NUMERICAL MODEL OF OTRC WAVE BASIN

BASED ON LINEAR HYDRODYNAMICS

A Thesis

by

FANG WANG

Submitted to the Office of Graduate and Professional Studies of
Texas A&M University
in partial fulfillment of the requirements for the degree of

MASTER OF SCIENCE

Chair of Committee,	Richard Mercier
Committee Members,	Hamn-Ching Chen
	Steven D. Taliaferro
Head of Department,	Sharath Girimaji

August 2017

Major Subject: Ocean Engineering

ABSTRACT

This thesis presents a numerical model of the Offshore Technology Research Center (OTRC) wave basin based on linear hydrodynamics. WAMIT program is used for hydrodynamic analysis. Two methods are explored in simulating the wave basin: (a) build the wave basin model in WAMIT program with tank walls and the pit as a fixed body; (b) simulate the reflection from tank walls using the method of images. In both methods, the wave maker motion is modeled using generalized modes and the higher order panel method is applied. On each panel, the momentum flux is calculated based on third-order Gauss quadratures. The numerical wave basin contains 48 wave maker flaps, side walls, a floor and the wave absorber is modeled as an open boundary.

Regular wave response, including the spatial uniformity of the wave field, has been studied. Evanescent modes from the wavemaker, the effect of reflection from a test model and the side walls, and oblique wave generation have also been investigated. It was found that reasonable results cannot be achieved using method (a) of direct side wall modeling despite numerous modifications to the tank geometry and its discretization; most noticeably, spatial uniformity cannot be achieved in long-crested wave generation. On the other hand, method (b) does yield spatial uniformity in long-crested wave generation, to numerical accuracy. Therefore method (b) is adopted for investigation of wave basin responses.

DEDICATION

This thesis is dedicated to my parents. Their persistent encouragement and support have always been with me.

CONTRIBUTORS AND FUNDING SOURCES

This work was supervised by a thesis committee consisting of Professor Richard Mercier and Professor Hamn-Ching Chen of the Department of Civil Engineering and Professor Steven Taliaferro of the Department of Mathematics.

All work conducted for the thesis was completed by the student independently.

There are no outside funding contributions to acknowledge related to the research and compilation of this document.

NOMENCLATURE

TGF	Tank Green Function
2D	Two Dimensional
3D	Three Dimensional
OTRC	Offshore Technology Research Center
POT	WAMIT Potential Control File
GDF	WAMIT Geometric Data File
FRC	WAMIT Force Control File
CFG	WAMIT Configuration File

TABLE OF CONTENTS

Page

LIST OF FIGURES

Page

LIST OF TABLES

Page

CHAPTER I

INTRODUCTION AND LITERATURE REVIEW

The numerical wave tank method has been widely investigated since Longuet-Higgins and Cokelet (1976) developed the direct numerical simulation of unsteady 2D potential free surface flows with the Mixed Eulerian-Lagrangian method. Raymond Cointe (1990) simulated transient free surface flows in the vicinity of a free surface-piercing structure. S. Y. Boo et al. (1994) developed a nonlinear numerical wave tank using a 3D higher order boundary element method. For the corners and edges of the wave tank, discontinuous boundary elements were employed. Tanizawa (2000) presented time domain simulation methods of nonlinear free surface and floating body motion involved with a numerical wave tank. Additionally, Tanizawa (2001) developed a 3D numerical wave tank for simulation of running ship motions in waves.

In recent years, the capability of numerical wave tank has increased significantly. M.H. Kim et al. (2001) studied the characteristics of nonlinear multidirectional waves and the effects of side-wall reflections using a finite-difference scheme and a modified marker-and-cell method. Large tank width or an effective side-wall absorbing mechanism is necessary for simulation of open-sea conditions. Westhuis (2001) developed a numerical algorithm for a fully nonlinear simulation of free surface waves based on a combination of Runge-Kutta, Finite Element and Finite Difference methods. Grilli et al. (2002) modified the 3D fully nonlinear potential flow numerical wave tank to simulate tsunami generation by underwater landslides and studied the effect of landslide

width. Weoncheol Koo (2004) built a 2D fully nonlinear numerical wave tank based on potential theory, mixed Eulerian-Lagrangian time marching scheme and boundary element method. X. T. Zhang et al (2006) studied wave propagation in a fully nonlinear numerical wave tank using the desingularized boundary integral equation method coupled with mixed Eulerian-Lagrangian formulations. He added a damping layer near the end-wall of the wave tank to absorb the outgoing waves.

In particular, J. N. Newman (2010) analyzed wave generation and absorption in a closed basin within the framework of linear potential theory. He used wavemakers for both generating and absorbing the waves in square and circular basins and derived the relations governing control of the absorbers.

In terms of wavemaker theory, the first step is the underlying wave theory. Stokes (1847) gave results for regular waves using the wave steepness. Stokes found that for regular waves, only the sum frequencies appear since the difference frequencies vanish. After that, first-order wavemaker theory corresponding to linearized Stokes theory has long been well established (Havelock, 1929; Biesel, 1951; Ursell et al., 1960; and others; cf. the review by Svendsen, 1985). Havelock (1929) calculated the two-dimensional motion of the water surface forced by the specified small amplitude horizontal oscillatory motion of an infinite vertical plate or vertical oscillatory motion of an infinitely long, partially immersed, horizontal cylinder. Lamb (1932) introduced the first-order theory of surface waves in deep water. Cooper & Longuet-Higgins (1951) investigated the reflection from a partially immersed vertical barrier by measuring the unsteady state before the secondary incident wave had travelled back from the

wavemaker. This unsteady state could be treated as a steady state with little loss of accuracy because it persisted for so many periods. The measured reflection coefficient was of an order of 10% lower than the theoretical and the discrepancy decreased as the depth of immersion of the lower edge of the barrier increased. The pressure variations in a purely progressive wave were found to obey the exponential law of decrease down to a depth of at least half a wave length, and below this depth were very small. Ursell et al. (1960) validated forced small-amplitude water waves with experiments and small-amplitude wave theory based on the assumptions that the fluid was inviscid, of uniform density, that motion started from rest and that non-linear terms were neglected. The results of frequencies, velocities, wave heights and forces agreed with theoretical predictions.

The motions of segmented wavemaker boards are generally calculated based on the snake principle. However, there are limitations to this technique. For example, the snake principle cannot account for the reflection effects from the sidewalls and the diffraction due to the finite length of the wavemaker paddle. The size of the optimal test area in the model basin can be small, especially if the maximum angle of the oblique wave is large. For model studies of offshore or coastal structures, it is important to ensure a large area with a homogeneous sea state for testing purposes. It should also be far from the wavemaker to ensure freedom from the evanescent modes. Funke and Miles (1987) developed an extension of the snake principle known as the corner reflection method. This technique makes use of partial sidewalls and is able to obtain a larger test area. Dalrymple (1989) developed a technique based on a splitting procedure used on the

mild-slope equation to develop a propagation equation for the wave potential in the wave basin, with reflecting sidewalls and a bottom. The wave field is determined as a function of the distance from the wavemaker paddle given its motion. Short-crested waves occur near the upwave sidewall and diffraction occurs at the other side of the tank due to the presence of sidewalls and the finite width of the wavemaker. The advantage of the Dalrymple theory over the snake principle is that the area of the basin where the desired multidirectional wave field can be reproduced is much larger. The analytic solution though is only applicable to the case of a wave basin with full-length reflecting sidewalls. As the waves propagate further down the basin, they gradually become contaminated by diffraction and reflection from the sidewalls. The reflection effects can be avoided by using partial-length sidewalls where there are side absorbers at a certain distance from the wavemaker. This will also account for the sidewall reflection of the diffracted wave field produced by the structure in the test area. Numerical validation of this theory was made by Mansard (1993).

In order to determine the exciting forces on a ship in waves, not only the hydrodynamic pressure in the incident wave but also the effects due to the presence of the ship have to be known. But in linear theory the diffraction or disturbance of this incident wave system due to the presence of the ship is difficult to evaluate. Haskind (1962) derived an expression for the exciting forces and moments on a fixed body without the need for diffraction effects. The result is calculated based on the velocity potential for forced oscillations of the body in calm water and it is known as Haskind relations.

Unlike in an unbounded domain, wave-body interactions in tanks of finite length are worth investigating due to the tank wall effect. Reflections from the tank walls can be significant if the width of the tank is of the same order as the body length or wavelength. An infinite array of image Green functions can be used for the boundary condition on the walls and the calculation of Green function is the key to the tank wall effect. There are several ways to formulate the Green function: through the method of images, method of eigen-functions or in the form of closed integrals. Kashiwagi (1990) replaced the infinite series of Green functions with a closed-form analytical expression. Chen (1994) developed the tank Green function (TGF) by integral representations. Linton (1999) derived a more efficient expression with rapid convergence. Xia (2002) presented a direct summation approach for the tank Green function based on the image representation. This is extended by Shen and Qin (2011) with partial reflection from side walls. Newman (2001) studied the wave effects on multiple bodies and showed that results with practical levels of convergence can be achieved by a finite number of image bodies, without extending the Green function. Linton (1998) described an analytical technique to transform the Green's function from the slowly convergent representation as sums of a series of images into an accelerated series of image Green functions.

Only recently, Newman (2016) investigated the channel wall effects with three approaches: (1) using a finite array of image bodies, (2) including reflecting walls of finite length, and (3) accelerating the convergence of the infinite series of image Green functions. A modified version of WAMIT is used to generate the result using the third approach. Added mass and damping coefficients are compared as well as heave and

pitch motions. The effect of walls is substantial and near-resonances occur when the distance between the body and the side walls is an integer number of wavelengths.

For irregular waves, sum and difference frequencies appear in the interaction terms at second order. Longuet-Higgins and Stewart (1964) delved in regression stress and derived results for the subharmonics when the frequencies were only slightly different. Ottesen-Hansen (1978) studied group-induced long waves and applied a transfer function in the expression of the second-order contribution of interacting first-order wave components, where the transfer function was defined by the ratio between generated wave amplitude and paddle amplitude.

This thesis aims to develop a three-dimensional numerical model of the OTRC wave basin based on linear hydrodynamics. The parameters of the numerical wave tank are identical to those of the OTRC wave basin. The model simulates 48 wave maker flaps, 2 side walls, and a floor with a pit. Wave absorbers are not used in this model. Rather, the wave absorber at the end of the tank is modeled as an open boundary. Regular wave response is studied. That includes the study of the wavemaker's evanescent modes, the generation of long-crested waves, the generation of oblique waves, the effect of reflection from the tank walls, and the exciting force on a bottom-founded caisson model in the test area in waves. A bottom-founded cylinder (caisson) is used as a representative object and it is placed in the tank to investigate the effect of reflections from the model and side walls.

The objective of the research is to develop a better understanding of how the side walls and floor of the basin, in relation to the location of the test area and the

wavemaker, affect the waves in the test area and the forces and responses on fixed platform models in the test area. Reflections from the wave absorber are not modeled or investigated.

CHAPTER II

THEORY

2.1 Linear Hydrodynamic Theory

The linear waves are small amplitude waves under the potential wave theory, where the water depth is assumed to be constant and the fluid is inviscid, incompressible and irrotational. We only consider monochromatic regular waves in this thesis. The water motion is then represented by a velocity potential which is denoted by ϕ. The fluid velocity is then described through

$$\vec{V} = \vec{\nabla}\phi = \vec{\imath}\frac{\partial \phi}{\partial x} + \vec{\jmath}\frac{\partial \phi}{\partial y} + \vec{k}\frac{\partial \phi}{\partial z}$$

Since the flow is irrotational, it has no vorticity and $\zeta = \vec{\nabla} \times \vec{V} = 0$. Thus,

$$\vec{\nabla} \times \left(\vec{\nabla}\phi\right) = \vec{0}$$

From the conservation of mass equation, we have the Laplace equation.

$$\vec{\nabla} \cdot \vec{V} = \vec{\nabla} \cdot \vec{\nabla}\phi = \nabla^2\phi = 0$$

From the conservation of momentum equation, we have the Bernoulli equation.

$$p = -\rho\frac{\partial \phi}{\partial t} - \frac{\rho}{2}\left(\vec{\nabla}\phi\right)^2 - \rho g z + C(t)$$

where ρ is the fluid density, p is fluid pressure, g is the gravity acceleration and $C(t)$ is a constant of integration.

The bottom boundary condition is

$$\frac{\partial \phi}{\partial z} = 0 \; on \; seabed$$

The kinematic free surface boundary condition is

$$\frac{\partial \eta}{\partial t} + \frac{\partial \phi}{\partial x}\frac{\partial \eta}{\partial x} - \frac{\partial \phi}{\partial z} = 0 \; on \; free \; surface \; z = \eta$$

The dynamic free surface condition is

$$\frac{\partial \phi}{\partial t} + \frac{1}{2}\left(\vec{\nabla}\phi\right)^2 + g\eta = 0 \; on \; free \; surface \; z = \eta$$

The linear approximations of these governing equations are used to obtain the first-order solutions for waves propagating in constant depth water without the presence of obstructions.

$$\nabla^2 \phi^{(1)} = 0 \; in \; fluid$$

$$\frac{\partial \phi^{(1)}}{\partial z} = 0 \; on \; seabed$$

$$\frac{\partial \eta^{(1)}}{\partial t} - \frac{\partial \phi^{(1)}}{\partial z} = 0 \; on \; undisturbed \; free \; surface \; z = 0$$

$$\frac{\partial \phi^{(1)}}{\partial t} + g\eta^{(1)} = 0 \; on \; undisturbed \; free \; surface \; z = 0$$

The velocity potential for a linear progressive wave is then

$$\phi^{(1)} = \frac{gH}{2\omega}\frac{\cosh\left(k(z+h)\right)}{\cosh(kh)}\sin(kx - \omega t)$$

where H is wave height, ω is wave frequency, h is water depth and k is wave number. Additionally the wave elevation η is then

$$\eta^{(1)} = \frac{H}{2}\cos(kx - \omega t)$$

The first-order pressure is obtained from the Bernoulli equation

$$p^{(1)}(x, z, t) = -\rho\frac{\partial \phi^{(1)}}{\partial t} = \rho g\frac{H}{2}\frac{cosh\left(k(z+h)\right)}{cosh(kh)}cos(kx - \omega t)$$

which is in phase with the wave elevation η.

We can use the complex notation to take the phase into consideration in a better way. We assume all variables are proportional to $\exp(-i\omega t)$. Then the harmonic functions can be expressed through the real parts of the complex expression.

$$\Phi(x,t) = Re\{\phi(x,\omega)e^{-i\omega t}\}$$

In wavemaker theory, the flaps act as solid boundary surfaces with prescribed normal velocity distribution to radiate waves. In order to generate oblique waves, the phases of discrete wavemaker flaps have to be shifted. The wavemaker flaps move in a wave-like pattern with a periodic length of $\frac{2\pi}{k_0}$, as shown in Figure 1.

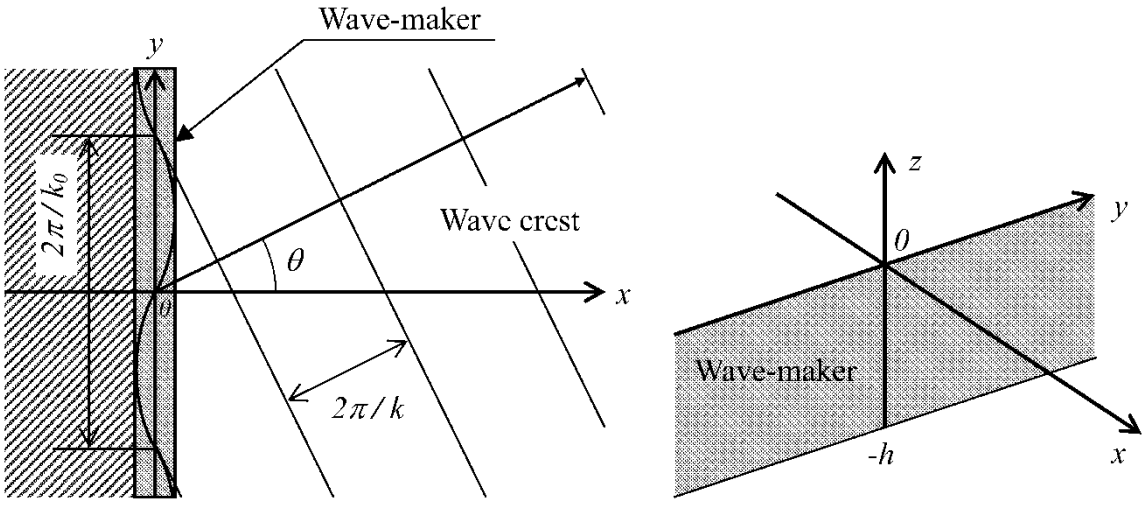

Figure 1 Wavemaker theory illustration reprinted from (Shigeru Naito, 2006)

The relation among wave number of progressive waves k, k_0 and propagation direction of waves θ is

$$k_0 = k \cdot \sin\theta$$

And the velocity potential of waves radiated by the wavemaker is (Shigeru Naito, 2006)

$$\phi(x,z,t) = A_p\, cosh\left(k_p(z+h)\right)\sin\left(k_p x - \omega t\right) + \mathrm{C}e^{-k_s x}\cosh\left(k_s(z+h)\right)\cos\omega t$$

The subscripts on *k* indicate that that portion of ϕ is associated with a progressive or a local standing wave. The values of wave number are real and imaginary roots of the dispersion relation. Here the values of k_p and k_s are determined from

$$\omega^2 = g k_p \tanh k_p h$$

and

$$\omega^2 = -g k_s \tan k_s h$$

There are an infinite number of imaginary roots of the dispersion relation and thus an infinite number of evanescent modes. These represent non-propagating, standing waves that decay exponentially with distance *x* from the wavemaker. Thus, the final form of the velocity potential is

$$\phi(x,z,t) = A_p\, cosh\left(k_p(z+h)\right)\sin\left(k_p x - \omega t\right) + \sum_{n=1}^{\infty} C_n\, e^{-k_s(n)x}\cosh\left(k_s(n)(z+h)\right)\cos\omega t$$

When linear waves interact with a reflective, large displacement, elastically restrained body, the velocity potential can be represented as the sum of incident, scattered, and radiated potential components. The incident wave potential corresponds to the potential without the body obstructing the flow and is related to the undisturbed pressure of the incident-wave system, denoted as ϕ_I. The scattered wave potential ϕ_S

represents the disturbance of the incident waves due to the presence of the body; in other words, it corresponds to the wave field that is scattered off the body assuming the body is fixed in space. The radiated wave potential ϕ_R represents the wave field generated by the motion of the body. The effects of the incident and scattered waves are combined and denoted as wave diffraction. The diffraction potential is denoted as ϕ_D.

In the case of the hydrodynamic force on the body, the problem is coupled in that the body oscillates in the incident wave and the motion of the body in return has an influence on the wave field. The coupled problem can be considered in two independent problems: the diffraction problem of regular incident waves moving past the fixed body and the radiation problem of forced sinusoidal oscillations of the body in otherwise calm water. The solution of each of these problems yields pressure distributions that can be integrated over the surface of the body to obtain the associated forces and moments.

The velocity potentials can be determined by solving the Laplace equation with appropriate boundary conditions. Note that the presence of the body will cause scattered and radiated wave disturbances to propagate away from the body. In the open ocean case where the fluid is unbounded horizontally, the scattered and radiated potentials need to satisfy the radiation condition

$$\phi_S, \phi_R \sim \frac{e^{-ikr}}{\sqrt{r}} \; as \; radial \; distance \; r \rightarrow \infty$$

MacCamy and Fuchs (1954) gave an analytical solution for linear diffraction by a bottom-mounted, surface piercing vertical circular cylinder in the form of Bessel functions. The problem is formulated in a cylindrical coordinate system (r, θ, z) with the

origin at the mean water level on the vertical axis of the cylinder. The vertical z axis is positive upwards, and the polar angle θ is measured from the wave-propagating direction using the right hand rule. The governing equations are

$$\nabla^2\phi_D^{(1)} = \frac{\partial^2\phi_D^{(1)}}{\partial r^2} + \frac{1}{r}\frac{\partial\phi_D^{(1)}}{\partial r} + \frac{1}{r^2}\frac{\partial^2\phi_D^{(1)}}{\partial\theta^2} + \frac{\partial^2\phi_D^{(1)}}{\partial z^2} = 0 \; in \; the \; fluid$$

$$\frac{\partial\phi_D^{(1)}}{\partial z} = 0 \; on \; z = -h$$

$$\frac{\partial\eta^{(1)}}{\partial t} - \frac{\partial\phi_D^{(1)}}{\partial z} = 0 \; on \; undisturbed \; free \; surface \; z = 0$$

$$\frac{\partial\phi_D^{(1)}}{\partial t} + g\eta^{(1)} = 0 \; on \; undisturbed \; free \; surface \; z = 0$$

$$\frac{\partial\phi_D^{(1)}}{\partial r} = \frac{\partial\phi_I^{(1)}}{\partial r} + \frac{\partial\phi_S^{(1)}}{\partial r} = 0 \; on \; body \; surface \; r = a$$

$$\lim_{r\to\infty}\sqrt{r}\left[\frac{\partial\phi_S^{(1)}}{\partial r} - ik\phi_S^{(1)}\right] = 0$$

where a is the radius of the cylinder and h is the water depth. The total surge force is

$$F = Re\int_{-h}^{0}\int_{0}^{2\pi} p(a,\theta,z)a\cos\theta d\theta dz$$

$$F = \frac{2\rho gHah}{ka\sqrt{J'^2_1(ka) + Y'^2_1(ka)}}\frac{tanh(kh)}{kh}\cos(\omega t - \alpha)$$

where $J_m(x)$ is the Bessel function of the first kind of order m. $J'_m(x)$ is the derivative of first kind Bessel function with respect to argument x. $Y_m(x)$ is the Bessel function of the second kind of order m. $Y'_m(x)$ is the derivative of second kind Bessel function with respect to argument x. $\alpha = \tan^{-1}\left\{\frac{Y'_1(ka)}{J'_1(ka)}\right\}$ is the phase shift.

2.2 WAMIT Theory and Setting

In the boundary-value problem addressed by WAMIT, a 3D body interacts with plane progressive waves in water of finite depth. The objective of WAMIT is to evaluate the unsteady hydrodynamic pressure, loads and motions of the body, as well as the pressure and velocity in the fluid domain. The potential fluid assumption is applied and the flow is assumed to be free of separation or lifting effects. A harmonic time dependence and linear wave theory are adopted.

The Cartesian coordinate system is used to define hydrodynamic quantities evaluated by WAMIT and is fixed relative to the undisturbed positions of the free surface and body. The z-axis is positive upwards. If planes of symmetry are defined for the body, the origin must be on the planes of symmetry. Through the harmonic time dependence, the product of all complex quantities with the factor $e^{i\omega t}$ applies. The complex velocity potential φ is related to velocity potential Φ by

$$\Phi = \mathrm{Re}(\varphi e^{i\omega t})$$

The output of WAMIT are in nondimensional forms, in terms of water density ρ, the gravity acceleration g, the incident-wave amplitude A, wave frequency ω, and the user-selected length scale L. For example, the free surface elevation is in nondimensional form

$$\bar{\eta} = \frac{\eta}{A} = \left(\bar{\varphi}_D + KL \sum_{j=1}^{6} \bar{\xi}_j \bar{\varphi}_j \right)$$

Here KL is the nondimensional infinite depth wavenumber. ξ_j is the nondimensional motion amplitude, and j is the mode index.

The nondimensional hydrodynamic pressure and wave elevation are equal to the nondimensional velocity potential. The wave exciting force on a body may be determined either by direct integration of the pressure associated with the diffraction velocity potential or from Haskind relations.

In the case of Haskind relations, assuming small disturbances of an ideal fluid, the velocity potential Φ satisfies Laplace's equation and the free-surface condition

$$\frac{\partial^2 \Phi}{\partial t^2} + \mathrm{g}\frac{\partial \Phi}{\partial z} = 0 \ \ on\ z = 0$$

Here $z = 0$ is the plane of the undisturbed free surface in the Cartesian-coordinate system. For incident waves of frequency ω, we have

$$\Phi(x, y, z, t) = \varphi(x, t, z)e^{i\omega t}$$

where the real part is to be taken in complex quantities involving $e^{i\omega t}$. Thus the potential φ satisfies the free surface condition

$$\frac{\partial \varphi}{\partial z} - K\varphi = 0\ on\ z = 0$$

where $\mathrm{K} = \frac{\omega^2}{g}$.

The problem is considered in two independent diffraction and radiation problems as discussed before. In the diffraction problem, the incident potential φ_0 and the scattered potential φ_7 must satisfy the boundary condition of zero normal velocity on the body, or

$$\frac{\partial}{\partial n}(\varphi_0 + \varphi_7) = 0\ on\ S$$

where **n** is the unit normal vector into the fluid and *S* is the submerged surface of the body. For the radiation problem, the velocity potential is of the form

$$\varphi = \sum_{j=1}^{6} v_j \varphi_j(x, y, z)$$

where *j*=1 to 6 corresponds to oscillations in the jth mode. And on the body, the potential φ_j must have the same normal velocity as the corresponding mode of the body, or

$$\frac{\partial \varphi_j}{\partial n} = f_j(x, y, z) \; on \; S \; (j = 1,2, \dots 6)$$

Both the radiation potential φ_j and the scattering potential φ_7 must satisfy the radiation condition. In view of these boundary conditions and the free-surface condition, it follows from Green's theorem that

$$\iint_S \left(\varphi_j \frac{\partial \varphi_7}{\partial n} - \varphi_7 \frac{\partial \varphi_j}{\partial n} \right) dS = 0 \; (j = 1,2, \dots 6)$$

The six exciting forces and moments denoted by F_j can be calculated by

$$F_j = \iint_S p f_j \, dS$$

where *p* is the hydrodynamic pressure and for the diffraction problem is given by the Bernoulli equation

$$p = -i\omega\rho(\varphi_0 + \varphi_7)$$

By substituting and applying Green's theorem with the reflective boundary condition on the body, we achieve the exciting force in a form depending only on the incident wave potential φ_0 and the radiated wave potential φ_j, or

$$F_j = -i\omega\rho \iint_{S_b} \left(\varphi_0 \frac{\partial \varphi_j}{\partial n} - \varphi_j \frac{\partial \varphi_0}{\partial n} \right) dS$$

This last result is the Haskind relations, which allows the exciting (diffraction) force in mode j to be calculated from the radiation potential φ_j for the j^{th} mode.

In the case of incident waves generated by wavemakers instead of being specified as incident from minus infinity, the exciting force acting on the body is determined by the motion of wavemakers and it is called the 'surrogate' exciting force. The wavemaker flaps are special radiating surfaces. The wavemaker flaps are hinged with pitching motions about a horizontal axis. The surrogate exciting forces and moments on the body due to the motions of an individual wavemaker flap are calculated from solution of coupled radiation problems only, which lead to cross-coupling added mass and damping coefficients, where one mode is for the body and the other mode is for the wavemaker flap. In this case of a wavemaker, the exciting force transfer function in each mode must be calculated outside of WAMIT as the force calculated on the body by WAMIT divided by the wave elevation at the reference position of the body calculated by WAMIT in a separate run without the presence of the body.

The incident wave system is defined relative to the global coordinate system. The phases of the quantities like exciting forces, motions, pressure and fluid velocity are defined relative to incident wave elevation at the origin. The outputs are in complex general form

$$\text{Re}\left((U + iV) e^{i\omega t} \right) = W \cos(\omega t + \delta)$$

where $\text{W} = |U + iV|$ is the modulus and $\delta = \tan^{-1}(V/U)$ is the phase.

There are several input files to configure for application of the WAMIT program. The two principal subprograms of WAMIT are POTEN, which solves for the velocity potential, and FORCE, which solves the force, the motion coefficients and field data including fluid pressure, velocity and free surface elevation. The typical input files for POTEN include the Potential Control File (POT), which specifies parameters including the fluid depth, wave periods, and wave heading angles, and the Geometric Data File (GDF), which contains the geometry information of the structure (body) to be evaluated. The principal input files for FORCE are the Force Control File (FRC), which includes the body dynamics information (mass, external damping and external stiffness matrices) and the Poten to Force (P2F) file, generated by POTEN for transferring data to FORCE.

The Configuration File (CFG) contains several parameters and options that are set to control the program execution. If a parameter is not specified, the default value will be used. We used the higher-order method of analysis, which is specified by parameter ILOWHI=1. In this method, the velocity potential on the body is represented by continuous B-splines and the fluid velocity on the body is evaluated by analytical differentiation. The body surface is subdivided into patches and patches are subdivided into panels. The number of patches NPATCH is specified in the GDF file. We can specify the number of panels, the order of the B-splines and the order of the Gauss quadratures to integrate over panels manually, or we can specify the size of panels with the parameter PANEL_SIZE and the program will do the subdivision of patches automatically.

To solve the linear systems of equations, we can use the iterative solver in WAMIT, specified by ISOLVE in the CFG file. A parameter MAXITT is used to control the maximum number of iterations. In the case of radiated waves from wavemakers in tank walls, we must use the parameter setting ISOLVE = -1, indicating that the wavemakers are in planes of symmetry, and it is not required to solve the integral equations of Green's theorem for the velocity potential on the wavemakers. In this case, the wavemakers are located in the walls, and the opposite walls of the wave tank have to be open domains extending to infinity or absorbing wavemakers.

In the presence of walls, it is assumed that all walls are planes of symmetry and the fluid motion is symmetrical about the planes. If the higher-order panel method is adopted, only one patch is required on each wavemaker flap.

WAMIT includes the capability to analyze generalized modes of body motion, extending beyond the normal six degrees of motion, for example motions of hinged bodies. The wavemaker consisting of a number of individual flaps is considered as a single body, with built-in generalized modes used to control the motion of individual flaps. The parameter IGENMDS=21 is specified in the CFG file for the wavemakers hinged with pitching motions about a horizontal axis. The depth of this axis is specified in the *wmkrhinge.dat* file and is the same for all wavemaker flaps. If more than one wavemaker flaps are analyzed, the outputs such as velocity potential and exciting force are generated individually in the order of the wavemaker flaps specified in the input file.

Other parameters in the CFG file are specified to choose which subprogram to use, which form of the input and output to choose, the number of generalized modes, the

number of field point arrays, whether to display output to the monitor and parallel processing capabilities. In case of bodies in channels of finite width, a channel width parameter can be specified so that the fluid domain is a channel of finite width with two parallel side walls that are perfectly reflecting. The parameters IWALLX and/or IWALLY can be specified in the CFG file to set the plane X=0 and/or Y=0 as a reflecting wall, respectively.

The fluid depth is specified in the POT file, as well as wave periods, wave angles and the indices IRAD and IDIFF specifying whether radiation and diffraction problems are to be solved. The number of bodies and the origin of the body-fixed coordinate system of each body relative to the global coordinate system are defined in the POT file. An array of modes for each body is specified to determine which modes of the radiation problem to solve.

We can specify what hydrodynamic parameters are to be evaluated in the FRC file using IOPTN indices, for example, the exciting forces from Haskind relations and the pressure/free-surface elevation at field points. The number of points in the fluid domain has to be specified if we want to evaluate the hydrodynamic pressure or wave elevation on the free surface. Or a 3D array containing the coordinates of field points can be defined conveniently. If the field point is on the free surface, the nondimensional potential is equivalent to the nondimensional wave elevation.

CHAPTER III

METHOD (A): DIRECT SIDE WALL MODELING

This chapter presents the numerical OTRC wave basin model for use with the direct side wall modeling method (method (a)), including the settings used to achieve the output from WAMIT. The results obtained using this method are also presented.

3.1 Numerical Wave Basin Model

The numerical model of the OTRC wave basin is built for simulation in the frequency domain. Two methods are explored in simulating the wave basin using WAMIT: (a) the wave basin model is assembled with finite length side walls and floor including the pit as a separate fixed body; (b) the wave basin model is assembled with the side walls represented using the method of images, as if the walls and floor are extended to infinity. In both methods, generalized modes are used to model the hinge-type wavemaker flaps and the higher order boundary element method is applied. The pressure / free-surface elevation at field points and exciting forces on a body in the wave basin are calculated using WAMIT and the database of the results is post-processed to generate 3D visualizations of the wave field using Matlab and to analyze the resulting forces.

In the direct side wall modeling method (method (a)), there are 2 bodies in the input. The first body is the fixed perfectly reflective boundary made of side walls, tank floor and the pit. The other body is the 48-flap wavemaker. Each of the 48 flaps is individually radiating as a generalized mode represented by a single patch. The body

geometry is represented by B-spline approximations, including parameters of panel subdivision numbers on each patch, the orders of the B-spline used to represent the potential and the orders of Gauss quadrature used for the inner and outer integrations over each panel. The wavemaker flaps are configured using a special subroutine in WAMIT and specified as hinged with pitching motions about a horizontal axis. The higher-order panel method is used for representation of the body boundaries. The velocity potential on the body is represented by B-splines in a continuous manner, and the fluid velocity on the body is evaluated by analytical differentiation.

The wave basin including 48 wavemaker flaps, 4 side walls of the pit, bottom of the pit, bottom floor of the tank and 2 side walls of the tank is set up in the input files. A uniform grid of field points is distributed over the free surface. Each of the 48 paddles will generate a separate complex wave field. The WAMIT-generated database of free-surface elevations at field points generated by individual flap motions is read and parsed in Matlab and rearranged for summation to obtain the total wave elevation at each field point.

The origin of the Cartesian coordinate system is set in the middle of the wavemakers on the undisturbed free surface. The positive x direction is along the direction of wave propagation and the positive z direction is the opposite direction of gravity. The tank side walls are 200’ long, 100’ thick and 60’ deep. The bottom floor of the tank is 19.05’ below the waterline. The edge of the pit is 38.5’ away from the wavemaker and is 30’ long, 15’ wide and 35.95’ deep (relative to the main floor at 19.05’ depth). There are 48 wavemaker flaps evenly distributed across the width of the

basin; each flap is 2.0417’ wide and 7.9583’ deep. The wave basin is 100’ wide. A back cavity is added to the basin to add communication of the pressure field with the back of the wavemaker. The cavity is 100’ wide,7.25’ long and 7.9583’ deep. After the back cavity is added, the side wall is extended by 15’ backwards and an outer end wall in the back is added. The wave basin is shown as Figure 2. The field points within the wave basin are shown in Figure 3.

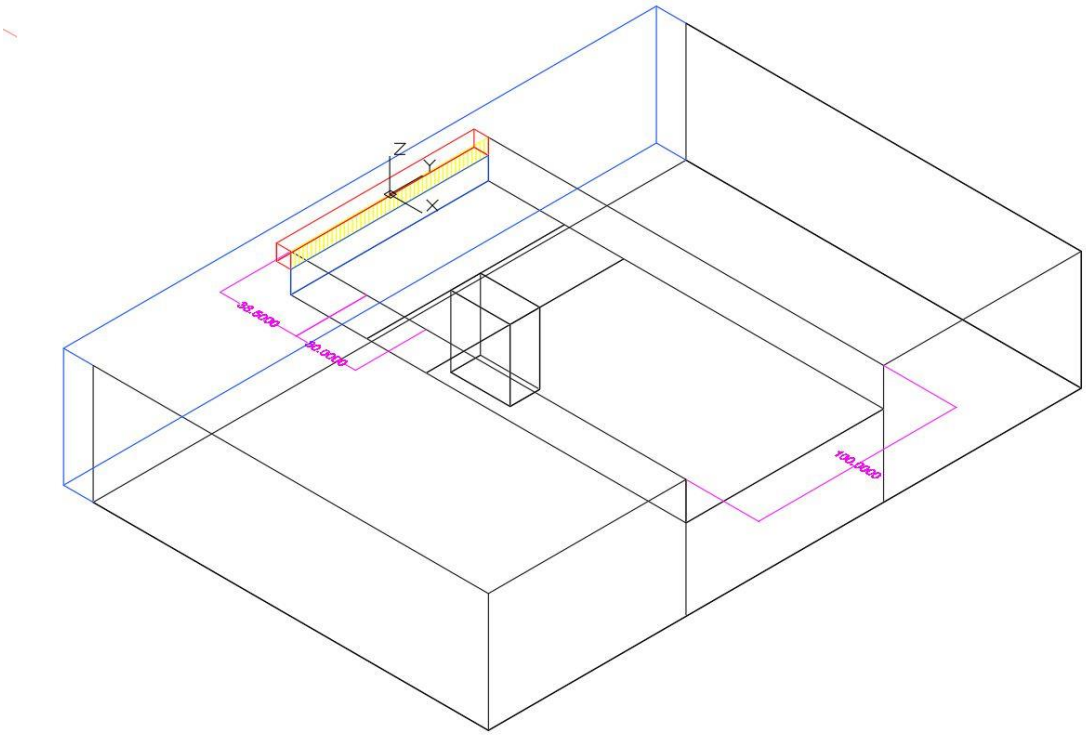

Figure 2 Wave basin model in CAD

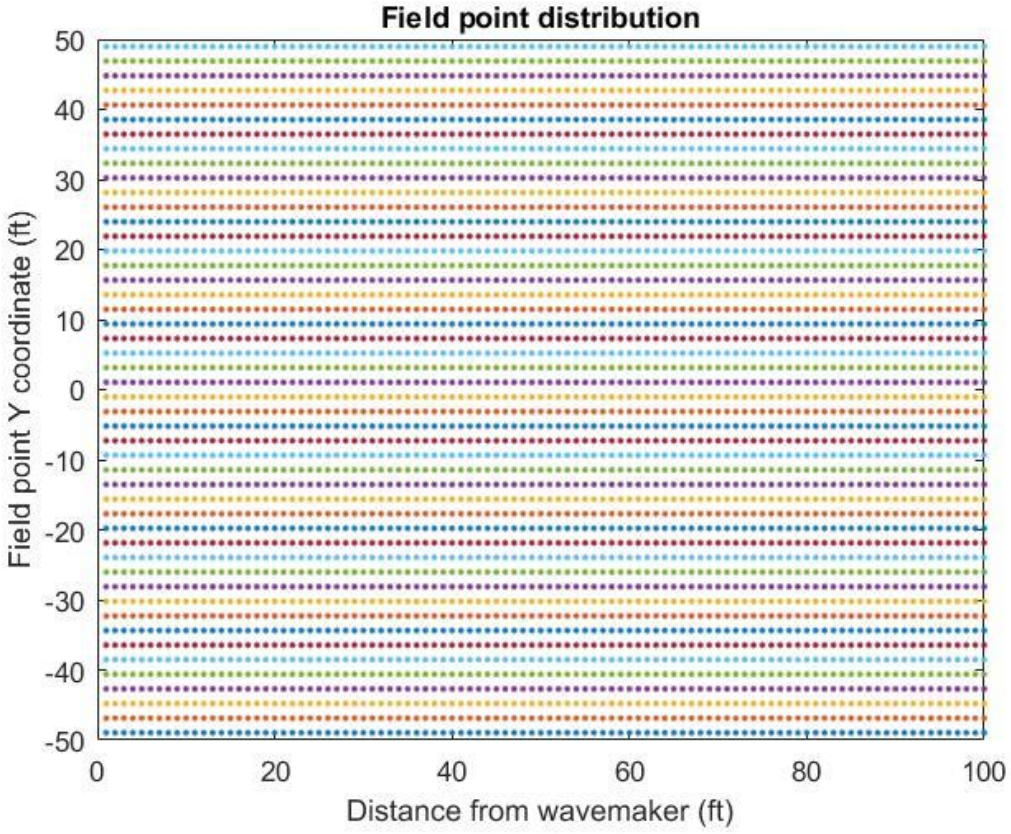

Figure 3 Field point distribution

3.2 Results and Discussion

Studies were made using the direct side wall modeling method, but inaccurate results with non-uniform wave fields were obtained in spite of numerous attempts to identify and eliminate the source of the problem. It has been years since the wavemaker feature was first introduced in WAMIT and there are published papers where the wavemaker capability in WAMIT was featured (J.N.Newman, 2008; John F. O'Dea and J. N. Newman 2007). We initially assumed that it was our lack of understanding in how to correctly prepare the WAMIT input that was causing the inaccurate results. That is

why a lot of exploration was made in order to try to make sense of the results we were obtaining. Because of our inability to obtain accurate results, we were forced to explore the alternative method of images (method (b)) to model the side walls. In April 2017 a new version of WAMIT was released with a specific new “channel width” feature for modeling waves propagating in a channel. This confirmed that there was indeed a problem in the previous version of WAMIT and WAMIT did not have the capability for accurately modeling wave propagation in a wave basin configured as in our method (a). Interestingly, the documentation provided for the “channel width” feature states that it is based on application of the method of images, which validated the method of images approach (method (b)) that we were already using at that time.

The results from method (a) are still presented herein to show the trials and exploration. All cases were run for periods from 0.5s to 4s, but not all results are represented in this thesis.

In this method of direct modeling, several settings and inputs were investigated. We started with 2 wavemaker flaps and increased to 48 flaps. And we also studied the cases with a single wavemaker flap spanning the entire width of the basin. For all cases, the results showed strong cross tank wave behaviors, which varied with the distance from the wavemaker. Figure 4 shows the real component of the free surface elevation in the case of a single wavemaker flap without a back cavity.

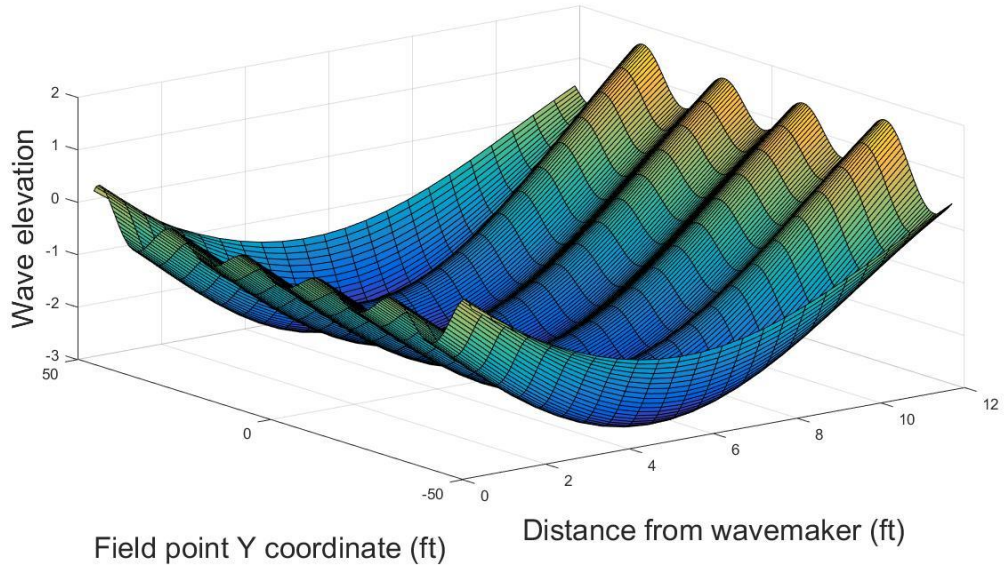

Figure 4 Real component of elevation generated by one 100’ wide flap without back cavity at period 2s

For any given cross-tank transect, the cross-tank wave behavior can be represented as a series of sinusoidal components. However, the reason why the sinusoidal components appear to vary with the distance from the wavemaker remains unexplained. We added a back cavity to the backside of the wavemaker, as is the case in the physical OTRC wave basin, to include consideration for pressure communication behind the wavemakers. However, the back cavity did not make any change in the results. The wave elevation for the entire wave field is shown in Figure 5.

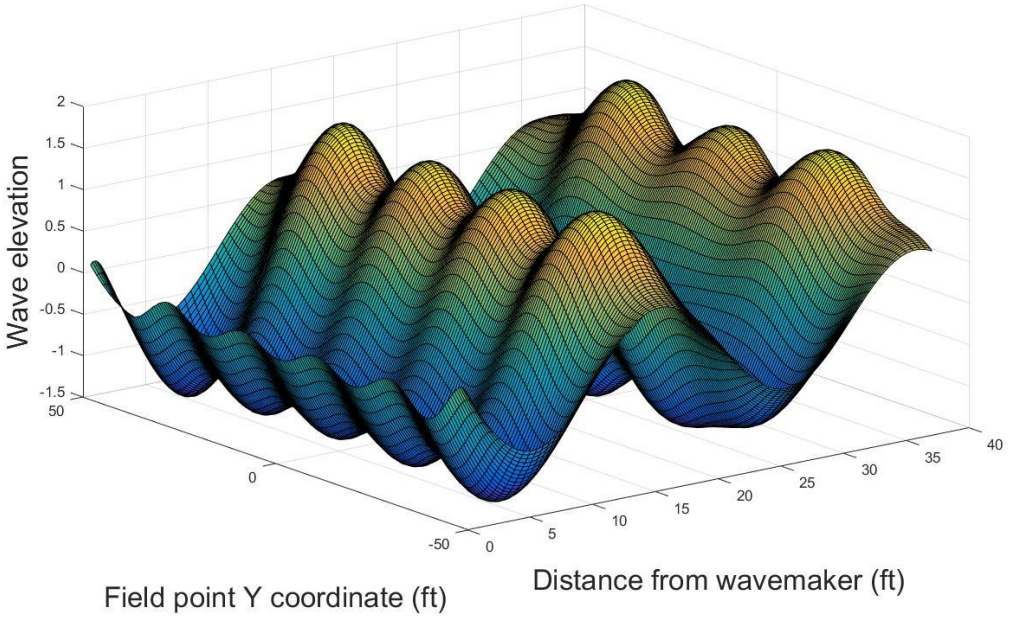

Figure 5 Real component of elevation generated by one 100’ wide flap with back cavity at period 2s

We replaced the 48 flaps with a single flap so that there are no gaps between the flaps. The result is pretty close to that of 48 flaps. We also removed the pit, and the results were not influenced. We extended the length of the side walls from 200’ to 400’ and 600’ and we closed the tank with an end wall instead of an open-boundary; the results remained unchanged.

To study the cross-tank wave behavior, we fit some cross-tank elevation transects with sums of sinusoidal functions, as shown in Figure 6, which is the cross-tank transect at the row of field points 24’ away from the wavemaker. The transect is from the single flap case at 2s period, fitted by a summation of 5 sinusoidal functions. Since the wave is propagating, the elevation in different transects is not only influenced by the cross-tank component, but also by the propagating component. To compare the cross-tank behavior

among different rows of field points (transects), we calculate the zero mean transect elevation by subtracting the mean value of the wave elevation across each transect, because the cross-tank mean values of the elevation represent the propagating wave component. The mean values of each transect can be calculated and fitted with one single sinusoidal function, as shown in Figure 7, which represents the expected propagating wave. The b coefficient in the fitting function $\mathrm{a} \times \sin(b \times x + c)$ can then be compared with the wave number for the corresponding wave period. As shown in Table 1, the difference between the fitted value and the theoretical value is relatively small, confirming the presence of the expected propagating wave component. So the observed cross-tank behavior remains a mystery.

Table 1 Fitted wave number and theoretical wave number of propagating wave

Period(s)	Theoretical wave number	Fitted wave number	Error
2	0.3067572	0.3046	0.70%
2.5	0.1963246	0.1959	0.22%
3	0.1363365	0.1417	3.93%
3.5	0.1001660	0.1055	5.33%
4	0.07669647	0.08562	11.63%

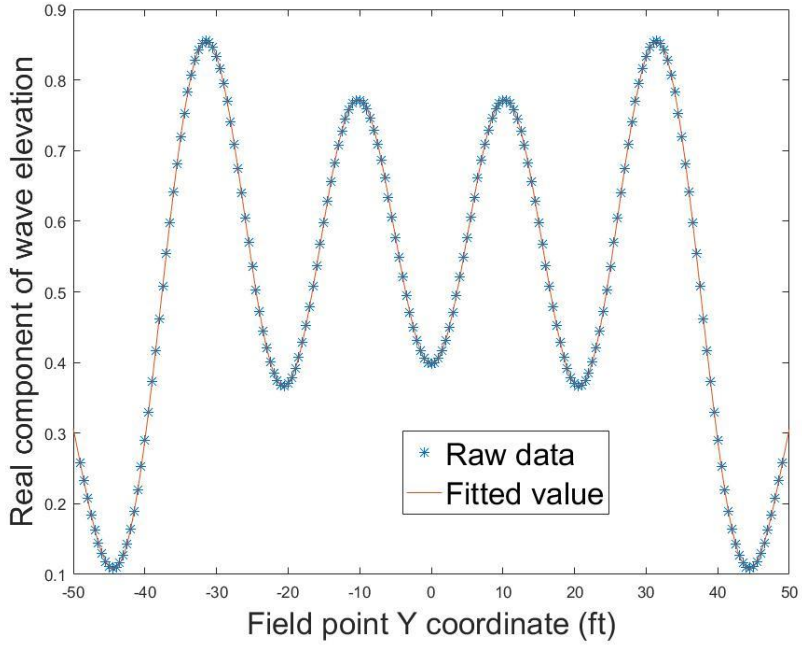

Figure 6 Cross-tank transect fit at 24' from wavemaker for single flap case at 2s period

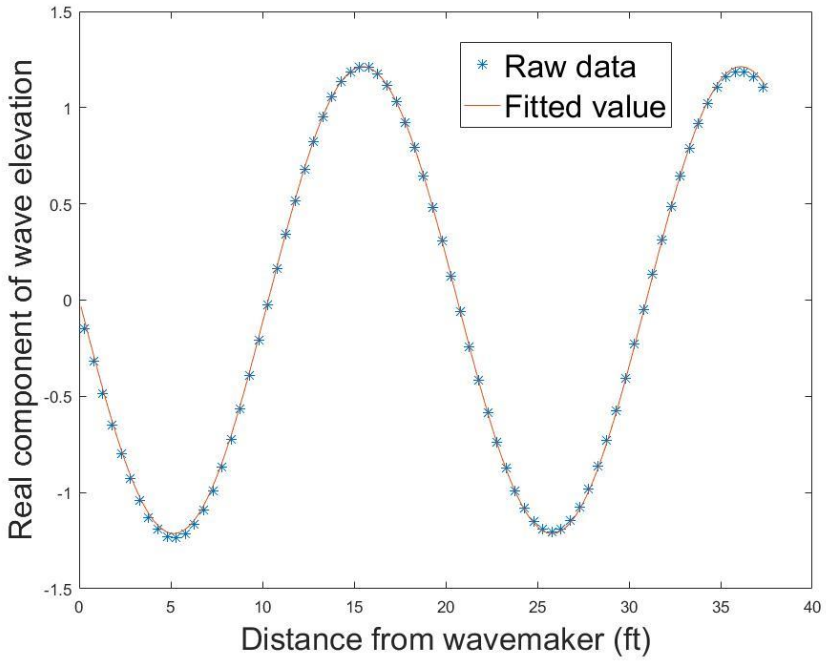

Figure 7 Mean elevation fit in the direction of wave propagation for 2s period, single flap case

The zero-mean transects can then be plotted and fitted by subtracting the mean elevation in the line. We can do this curve fitting to a series of lines and plot all transects from different distances to the wavemaker on top of each other. Unfortunately, they appear in different patterns as shown in Figure 8. In other words, this cross-tank behavior has spatial variation in the wave propagation direction. And this variation contributes to the nonuniformity in the wave field, as shown in Figure 9.

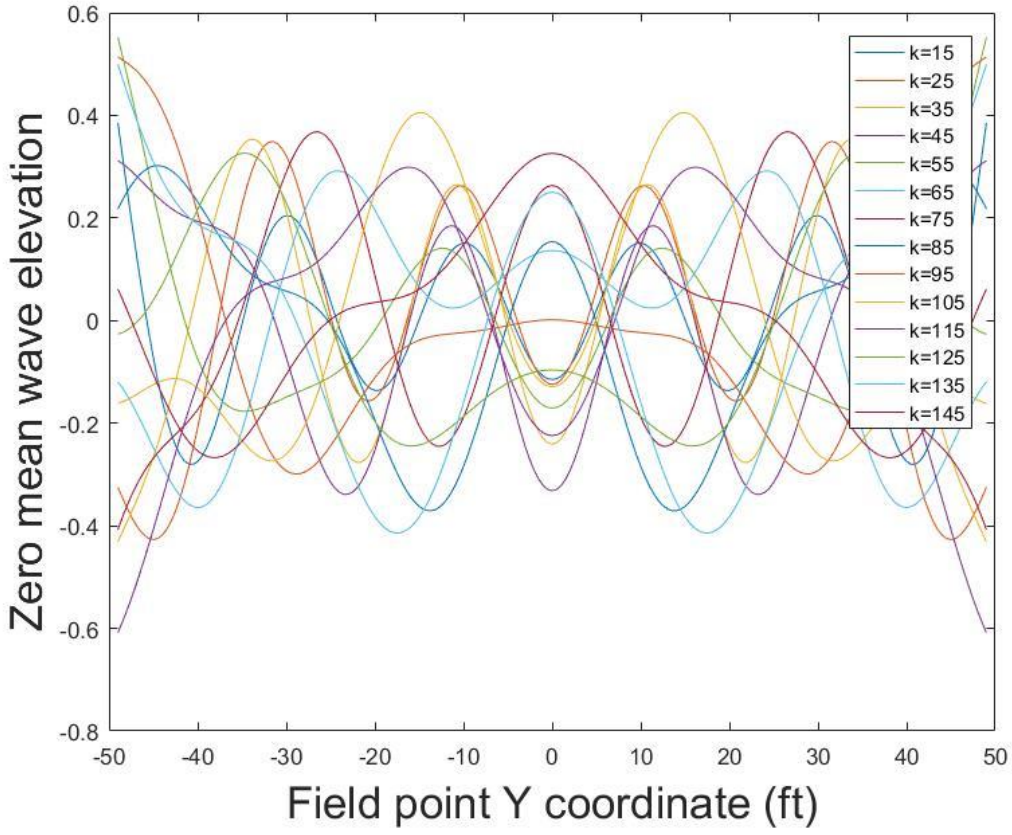

Figure 8 Zero mean cross-tank transect at Period 2s

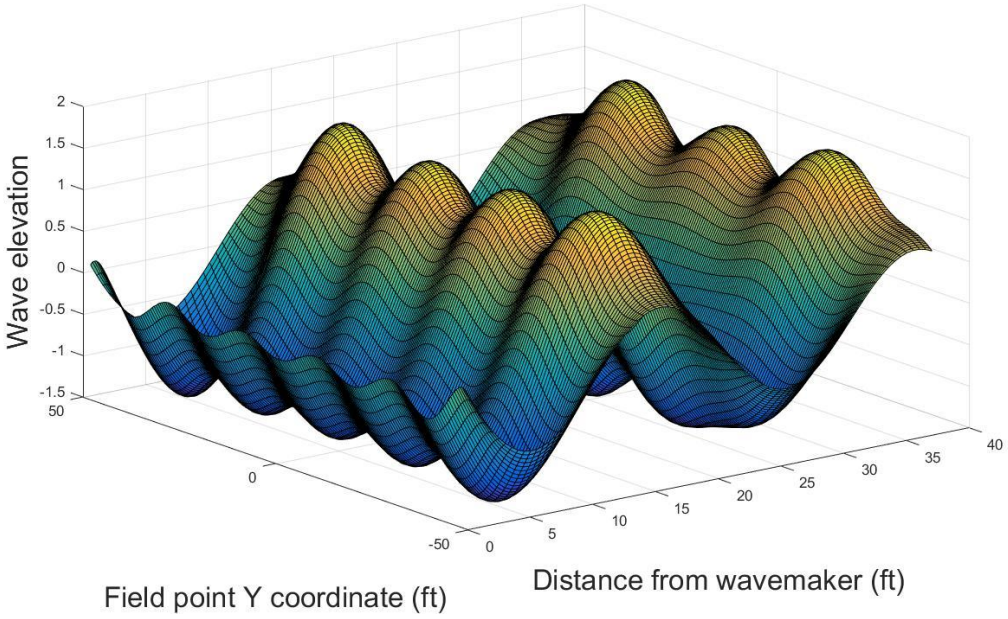

Figure 9 Real component of elevation from 2s period, single flap case

We set up cases where there were no tank walls and where there was one side wall, and the calculated wave fields illustrated the expected behavior without spurious cross-tank oscillations. As long as we introduced a second parallel tank wall, there would be unexplained spatial varying cross-tank behavior. Without the ability to understand or correct the source of the problem in WAMIT, it was necessary to introduce and adopt the method of images for further study.

CHAPTER IV

METHOD (B): SIDE WALL MODELING USING THE METHOD OF IMAGES

This chapter presents the numerical OTRC wave basin model based on the method of images, including the settings used to achieve the output from WAMIT and the algorithms of Matlab codes used for post-processing.

4.1 Numerical Wave Basin Model

Using the method of images to model the side walls, the WAMIT input does not contain a separate body to represent the tank boundaries. With this modeling approach we did not include the deep pit in the basin, although how to incorporate the pit could be the subject of a future study. For the study of wave elevation in the basin without the presence of a fixed or floating structure, the WAMIT input only contains one 2.0417' wide wave flap in a semi-infinite domain. For the study of exciting force on an axisymmetric body in the test area, the input contains twenty-four wave flaps. This would also be the case if the model being tested is symmetric about the centerline of the wave basin, otherwise 48 wave flaps would need to be included in the input if the model did not have the longitudinal plane of symmetry. The method of images is used to account for the reflection effect from the wave tank side walls.

In the case of free-surface elevation, since the tank walls are assumed to be perfectly reflective, the reflection from the side wall is taken as if there is a wavemaker image at a symmetric location on the other side of the imaginary wall, as illustrated in Figure 10. If the x-axis is a perfectly reflective tank wall, the wave elevation

contribution from the wavemaker flap at (x,y) on the field point at (x_0, y_0) can be treated in two parts: the direct influence as denoted by the dashed line in the figure; the reflection of the tank wall as denoted by the dotted line in the figure. The reflection influence component from the wavemaker flap at (x,y) is equivalent to the direct influence from the image flap at (x,-y).

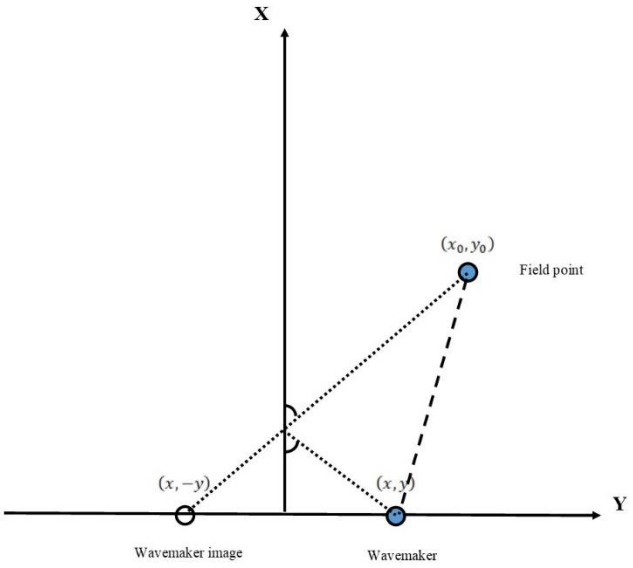

Figure 10 Illustration of reflection on side walls

In the case of two parallel side walls, the original wavemaker flap has reflection effect from both side walls. Thus, the reflection can be represented by two image flaps of the original wavemaker flap on both sides of the tank. Each of these 1st image flaps has

direct influence on the field point and is also reflected by the corresponding side wall, which creates two 2nd images. Since the side walls are perfectly reflective, the reflection continues and there are an infinite number of such reflections between the two side walls, as shown Figure 11. Thus, an infinite number of images is required to simulate two parallel side walls. As more images are included in the summation, the result will be more accurate. For a given wave period and a given field point, there exists a minimum number of images that can achieve a certain accuracy of convergence in terms of wave elevation simulation. So instead of an infinite number of images, a finite number of images are used for the computations. Convergence tests are performed to verify that the employed number of images is adequate.

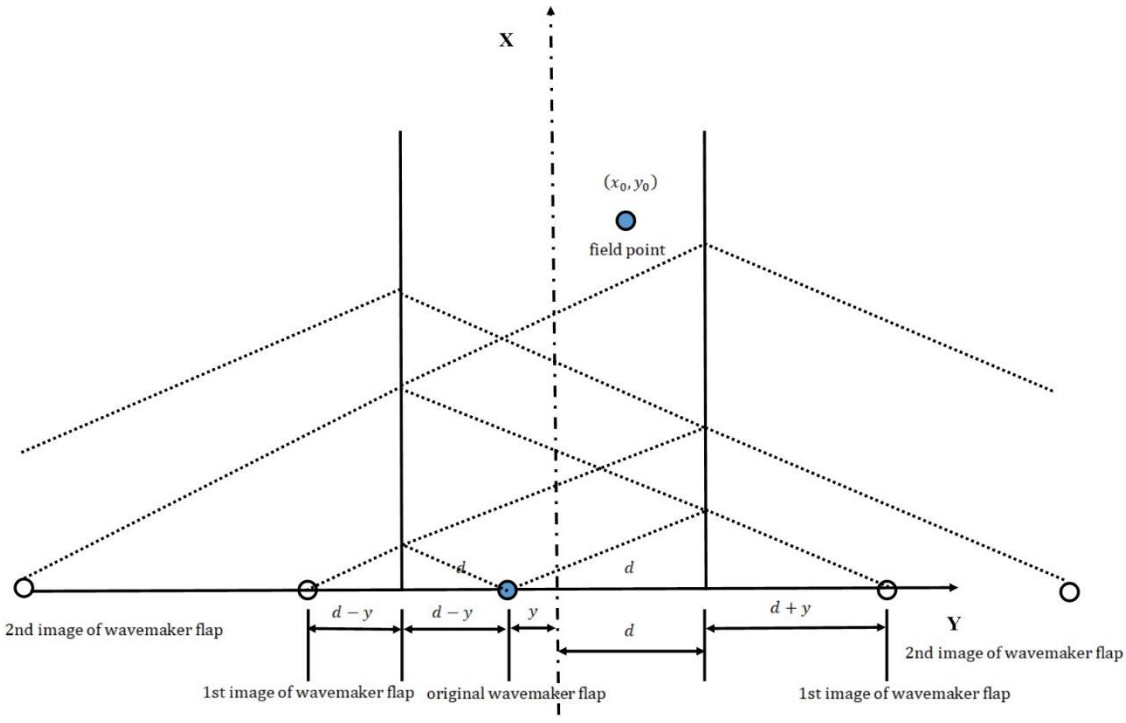

Figure 11 Method of images illustration

The geometry of each individual wavemaker flap is the same as previously described, which is 2.0417’ wide and 7.9583’ deep. There is a gap between adjacent wavemaker flaps. With 48 wavemaker flaps, there will be 49 gaps in total over the 100’ width of the basin, including the gap between the outer wavemaker flaps and the side walls. The summation of the gap widths is 2’.

For the case of wave generation in the basin without a body in the test area, one wavemaker flap is used in WAMIT to provide the field point information necessary to generate the entire wave field in the basin. This is done through judicious selection of

the array of field points. At a given field point within the basin, the influence from an image of a wavemaker flap can then be tracked to the influence from the original wavemaker flap on a corresponding field point that has the same relative position. The distance from an image of a wavemaker flap to a field point is relative to that from the wavemaker flap at the origin to a corresponding field point in the array of field points. As shown in Figure 12, the influence from an image of a wavemaker flap to the field point at (x_0, y_0) can be represented by the influence from the wavemaker flap at the origin to a corresponding field point with the same relative distance Δd.

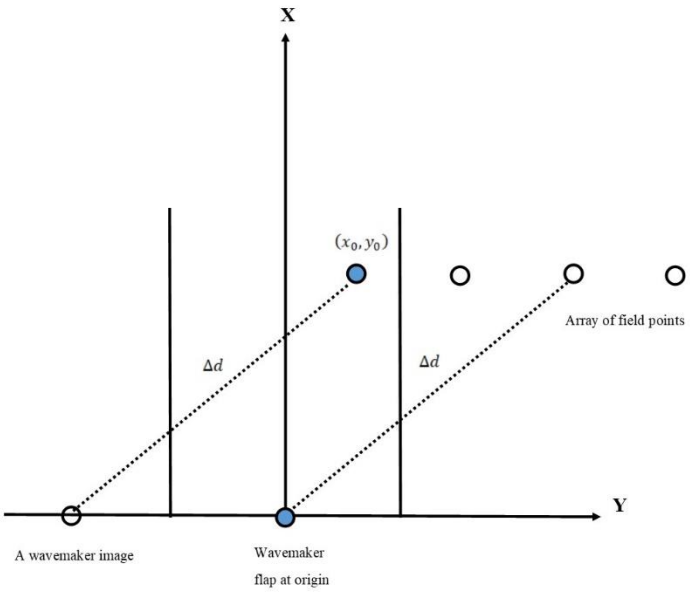

Figure 12 Illustration of relative distance

The selected array of field points is separated by 1’ in the x direction and 2.0833333’ in the y direction. Note that this distance in the y direction is just the width of 100’ divided by 48 wavemaker flaps. It is the distance between each consecutive wavemaker flap. A total of 80,001 by 100 field points are selected in this case, which represents a distance of up to $80{,}000 \times 2.0833333' = 166666'$ away from the wavemaker flap at the origin. The 3200^{th} image is 159,802’ away from the origin. Thus, this array of field points covers the distance of at least 3200 images of the wavemaker flap to a field point in the tank, giving the capability to simulate the wave tank with 3200 wavemaker images. The result can then be post-processed to generate non-oblique and oblique wave fields.

A bottom-founded vertical circular cylinder is used as a test case to illustrate the evaluation of the wave exciting forces on a body in the wave basin. Similar to the case of free-surface elevation, the method of images is applied to represent the reflection from the tank side walls. In this case, a finite number of images of the cylindrical body are evaluated in addition to the images of the wavemaker flaps to account for the reflections from the side walls. Twenty-four wavemaker flaps are used in this case because of symmetry about the centerline of the wave tank. The radius of the cylinder is 1.5’ and the draft is 19.05’, which is the same as the water depth. The center of the cylinder is 53.5’ away from the wavemakers in the positive x direction, as that is where the center of the pit (test area) lies. The images of the cylindrical body are separated by the width of the wave tank from each other.

Wave exciting forces from the Haskind relations are evaluated. An incident wave, open ocean case including both radiation and diffraction method is built for comparison.

4.2 Algorithm to Parse WAMIT Output

When the method of images is applied, several iterative loops are used to structure the WAMIT results prior to summing the individual contributions. As discussed above, in the free surface elevation case, the input contains only one wavemaker flap that is used to generate the wave field on a series of field points. The output from WAMIT is stored in the sequence of field points. The result is read in Matlab and is rearranged in the matrix form through iteration.

The purpose of adopting the matrix structure to store the data is that it provides a minimum level of O(1) access time to point to the data in a specific position. However, the drawback is that operations on matrices take more processing time especially when the dataset is big. The procedure that takes most of the time is parsing the output and rearranging it in the desired form, due to the number of iterations. Therefore, the raw output is parsed only once, and all useful information is stored in one or more matrices. The matrices can be loaded in an instant for post-processing. In that way, the most time consuming part is only executed once and it is cheap enough to do various post-processing steps.

In this case, we are to create a matrix containing free surface elevation information for N_f = 48 wavemaker flaps on the entire wave field. The file to parse in Matlab is the source WAMIT output file of one flap. We denote the index of wavemaker

flaps as q. The range of q is 1 to N_f = 48. We denote the row index of field point as r, corresponding to the x-coordinate of the field point. The range of r is 1 to N_r = 100 in the case of 100 rows of field points. Since the field point is separated by 1' in x-direction, the x-coordinate of a field point x_0 is equal to r'. We denote the column index of field point as c, corresponding to the y-coordinate of the field point. The range of c is 1 to N_c = 48 in the case of 48 columns of field points. Then a certain field point can be accessed by a pair of indices, (r,c), corresponding to coordinate (x_0, y_0) . The field point y-coordinate y_0 can be calculated through

$$y_0 = -D/2 + D/N_c/2 + (c-1) * D/N_c$$

where D is the width of the basin. In this case, D=100'.

Since there are N_f = 48 wavemaker flaps in the wave basin model, we denote an index q, which is the index of the wavemaker flap. The y-coordinate of the wavemaker flap y can be calculated through

$$y = -D/2 + D/N_f/2 + (q-1) * D/N_f$$

We denote the number of images we want to include as M, and an index of the image as j, corresponding to the j^{th} image. The range of j is 1 to M. For the j^{th} image of a wavemaker flap, the coordinate can be calculated and the absolute distance from the image to a field point at (x_0, y_0) can be determined. We denote the distance corresponding to flap images on the positive y-axis as d_{j+} and that corresponding to flap images on the negative y-axis as d_{j-}. Thus, we have

$$d_{j+} = \left|(j-1) * D + (-1)^{j-1} * y - y_0\right|$$

and

$$d_{j-} = \left|(j-1) * D + (-1)^j * y + y_0\right|$$

The absolute distance is used to compare with the source database (raw WAMIT output) where we have a single flap and a series of field points. In the input file of WAMIT, field points are created so that the distance to the wavemaker flap at the origin will match with the distance d_{j+} and d_{j-} in the 48 wavemaker flaps case. So the wave elevation of the WAMIT output is corresponding to that in the 48 wavemaker flaps case.

We have defined an intermediate matrix $\eta_{jq}(x_0, y_0)$ to store the complex wave elevation information. It is a matrix of *M* by N_f. The row index j is the number of images and the column index q is the wavemaker index. The element $\eta_{jq}(x_0, y_0)$ contains the incremental wave elevation at a certain field point (x_0, y_0) generated by the j^{th} image of the q^{th} wavemaker flap. The summation of each column, $\sum_{j=1}^{j=M} \eta_{jq}(x_0, y_0)$ can be used to calculate the cumulative elevation generated by a number of images for each wavemaker flap. This is the basic unit matrix that the parsing program works on.

We have defined a resulting matrix η_{rcq}. It is a three-dimensional matrix of field point row N_r by field point column N_c by wavemaker flap N_f. This is the main result of the parsing code. It contains the information needed for generating the wave field for either the non-oblique or oblique wave case. Since a wavemaker flap and its images are in phase, we can sum the complex elevation of all the images from the same wavemaker flap. The summed wave elevation at field point (x_0, y_0) with indices (r,c) from the wavemaker flap q and its images is stored in η_{rcq}, or

$$\eta_{rcq} = \sum_{j=1}^{j=M} \eta_{jq}(x_0, y_0)]$$

We have also defined a resulting matrix $\eta_{rcj'}$, storing a cumulative running total elevation for the first *j'* images from all 48 flaps. It is a three-dimensional matrix of field point row N_r by field point column N_c by number of images *j'*. The element $\eta_{rcj'}$ contains the cumulative elevation from *j'* images of all N_f wavemaker flaps for field point (*r*,*c*) and can be calculated by

$$\eta_{rcj'} = \sum_{j=1}^{j=j'} \sum_{q=1}^{q=N_f} \eta_{jq}(x_0, y_0)$$

This running total matrix can be used for convergence tests to show the trend of adding more images to the summation.

We have also defined an additional matrix $\eta_s(x_0, y_0)$, storing the summation of wave elevation from all wavemaker flaps and *M* of their images. It is a two-dimensional matrix of field point row N_r by field point column N_c. The element $\eta_s(x_0, y_0)$ contains the total elevation for field point (x_0, y_0), or

$$\eta_s(x_0, y_0) = \sum_{j=1}^{j=M} \sum_{q=1}^{q=N_f} \eta_{jq}(x_0, y_0)$$

In this matrix, the contribution from different wavemaker flaps is not separated so we can only use it for the non-oblique wave case.

The parsing process is built in nested for loops and is done iteratively. The basic operation is to find the matching distance of d_{j+} and d_{j-} in WAMIT output and store the

corresponding wave elevation information in the matrix η_{jq}. The first inner loop is to iterate through image index *j*. Given a wavemaker flap *q*, do the basic operation to all *M* images of *q*. The second inner loop is then to iterate through wavemaker index *q*. Through these two layers of iteration, the matrix η_{jq} is then complete, containing elevation information for a certain field point (x_0, y_0).

The row summation of the matrix, which is $\sum_{j=1}^{j=M} \eta_{jq}$, is then stored in a corresponding vector of the matrix η_{rcq}, connected through wavemaker index *q*. The summation of all elements in this matrix, which is $\sum_{j=1}^{j=M} \sum_{q=1}^{q=N_f} \eta_{jq}$, is then stored as an element in the matrix of $\eta_s(x_0, y_0)$. The cumulative running row summation of η_{jq} is then stored in a corresponding vector in the matrix $\eta_{rcj'}$, connected through image index *j'*.

After performing this iteration, the third inner loop iterates through field point column *c*. The above operation is processed for each line of field points in a row *r*, from the first point where *c*=1, to the last point where *c*= N_c. By the end of this loop, we will have the wave elevation for a line of field points at row *r*. Or, a row *r* of elevation is filled in the matrices $\eta_{rcq}, \eta_{rcj'}$ and η_s.

The last inner loop, or the outer loop, is to iterate through field point row *r*. The above operation is processed for each row of field points. Through the parsing process, the wave elevation for the entire wave field with points on (x_0, y_0) is found and stored.

The illustration of this iterative structure is shown in Figure 13.

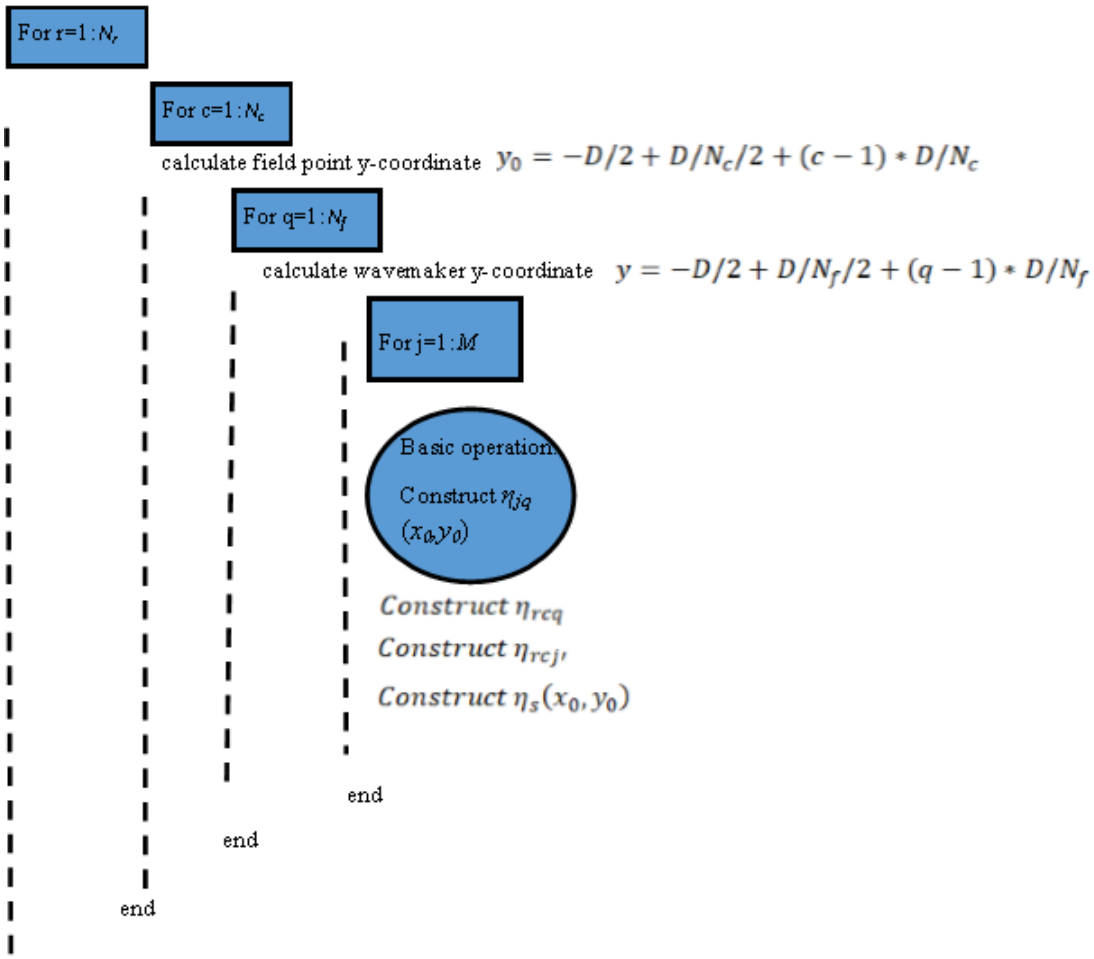

Figure 13 Illustration of iterative structure in parsing

The exciting force is output in the WAMIT '*.2' file following the order of individual wave period, individual wave flap or heading angle, body and modes. The real and imaginary components of surge and sway force are read into Matlab and then rearranged in matrix form with the number of periods as column. In our case, we have 8 periods, 24 wavemaker flaps and 21 images of the cylinder. For each period, there exists $24 \times 21 = 504$ components for surge force and the same amount for sway force. The resulting matrices are 504 by 8. The matrices are then partitioned into several groups.

Each group contains the components from 21 images of a wavemaker flap. A summation of such groups yields a resulting matrix of 24 by 8, giving the force from each wavemaker flap and its images. Here 24 corresponds to the number of wavemaker flaps and 8 corresponds to the number of periods. Again, since a wavemaker and its images are in phase, we can do this summation without losing phase information.

CHAPTER V

RESULTS AND DISCUSSION

5.1 Convergence Test for Method of Images

As discussed above, wavemaker images are used to account for the reflection of sidewalls. Theoretically, the more images we use, the more accurate we can get in simulating the reflection between two sides walls. However, handling a very large number of images is very time consuming in the stage of parsing and the accumulating error or the loss of precision may become a problem.

A convergence test is done to show that the number of images we use is adequate for a certain accuracy or a certain level of convergence. It is shown that the wave elevation or wave amplitude generation for a field point is converging with the number of wavemaker images used.

For a given wave period and field point, the wave elevation vs the number of images used in the positive y side forms a trending curve. An envelope can be generated and the difference between the upper and lower envelope decays as more images are used. The envelopes are determined by spline interpolation over local maxima separated by at least *np* samples, in our case, np=2. The difference curve is fitted with a two-term Gaussian model of the form

$$y = \sum_{i=1}^{2} a_i e^{\left[-\left(\frac{x-b_i}{c_i}\right)^2\right]}$$

The result is used to determine the number of images necessary for a certain accuracy of convergence. The wave elevation contributions from all images are accumulated in complex form to achieve the simulation of elevation from a wave flap with side walls.

As mentioned in the foregoing, we are able to fit an envelope on the plot and get the difference between the upper and lower envelope. An example is shown in Figure 14, which is the converging elevation for Period 2s at field point (25', 1.0417') in the case of 165 images. The envelopes are determined using spline interpolation over local maxima separated by at least np samples and the difference between the upper and lower envelope (i.e. the range of the computed elevation) is fitted in a two-term Gaussian fit model, as shown in Figure 15.

The Gaussian model can be used for evaluating the level of convergence given a number of images. Note that the converging plot varies with different field points but they all show a consistent converging trend. And for longer periods a larger number of images have to be summed to reach the same level of convergence as compared to shorter periods.

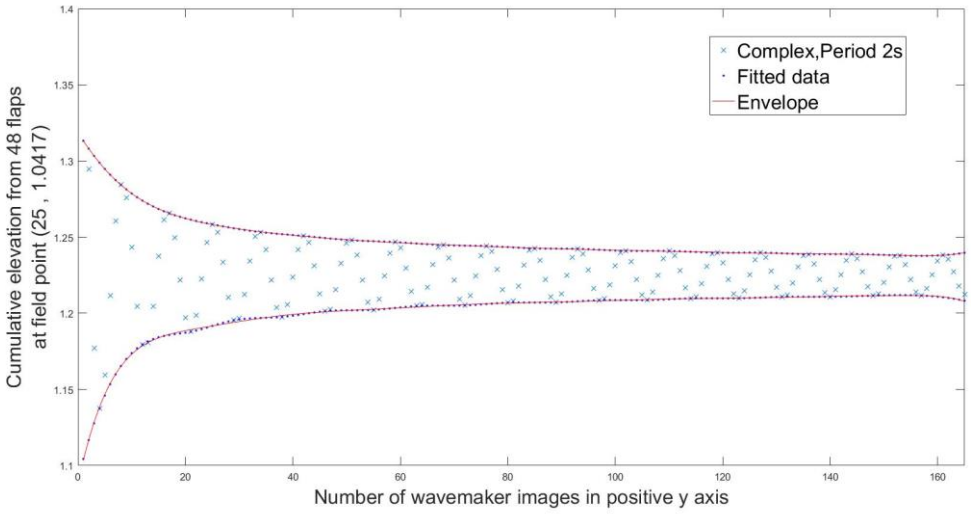

Figure 14 Cumulative amplitude from all flaps with envelope fitting for Period 2s at field point (25', 1.0417')

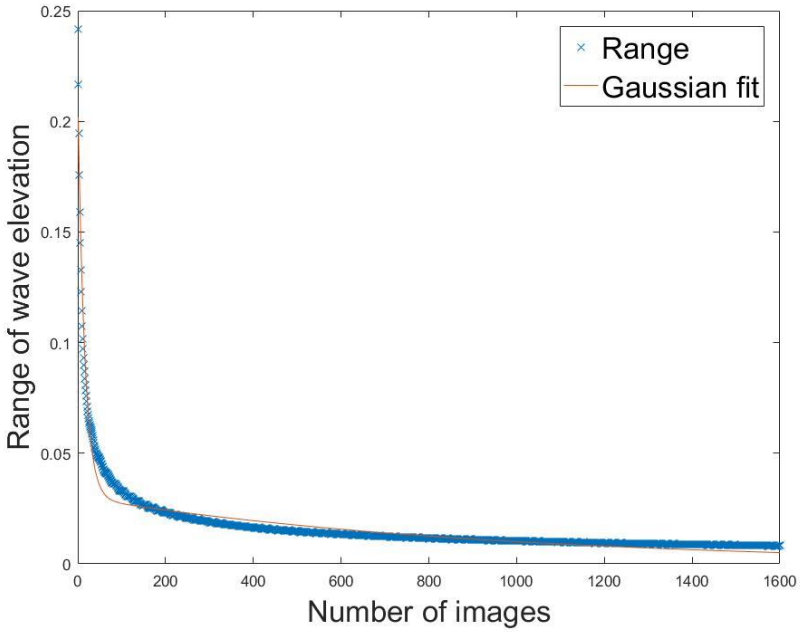

Figure 15 Gaussian fit of range of wave elevation for Period 2s at field point (50', 1.0417')

We first set up an initial case with 8001 points. The result provides information for a line of field points 25’ away from the wavemaker. Based on the relative distance from the image of a wavemaker flap to the field point, these 8001 points can cover the distance of up to 165 wavemaker images. In this thesis, the reported number of images represents the number of images in the positive y-axis, as there is always a corresponding image in the negative y-axis. With 165 images reported, we are actually using $165 \times 2 - 1$ images.

A Gaussian model is fit to the wave elevation results for each field point and the number of images needed to reach a certain level of convergence is calculated. Table 2 shows the number of images needed to reach certain levels of convergence for Period 2s. The numbers larger than 165 are determined based on extrapolation of the fitting function. Although the entire set of results for all field points in the row is not listed, the maximum number of images from each column in Table 2 is provided at the bottom of the table. Figure 16 shows the plot of number of images needed for 2% convergence level on all field points, which is the column of 2% in Table 2. We can see that the number of images needed is different for different field points.

Table 2 Number of images needed for convergence at 2s period based on model with 165 images

Field point y-coordinate (ft)	2% convergence	1% convergence	0.5% convergence	0.1% convergence
1	28	123	237	490
2	1	13	44	327
3	10	27	123	369
4	35	140	249	495
5	51	164	275	523
…	…	…	…	…
48	28	123	237	490
MaxNumber	51	168	289	561

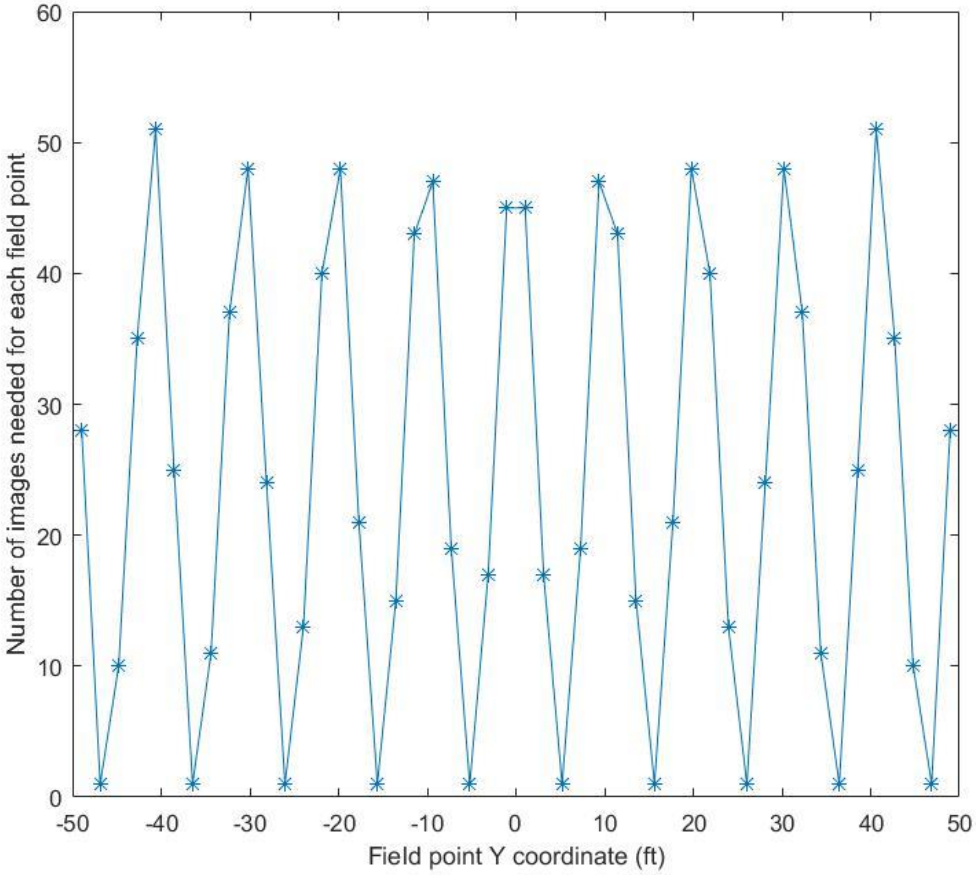

Figure 16 Number of images needed for 2% convergence level

It is shown that with 165 images, we can reach a decent accuracy at 1% level of convergence for all points at row 25' away from the wavemaker, for period 2s. We can then post-process the result of 165 images with confidence.

For a line of field points 25' away from the wavemaker, we can then plot the cross-tank wave amplitude by 165 images from all 48 wavemaker flaps. The amplitude is shown as Figure 17. The level of amplitude variation is about 2%, which is calculated by dividing the largest difference of the amplitude by the mean of the amplitude. This is

a much better uniformity compared to what we have with the direct side wall modeling method. We could barely see the cross-tank behavior if we consider the scale of the wave tank. Again, the number of 165 is the image number on the positive y-axis. As images come in pairs from positive and negative axis, the plot is actually a summation of $(165 \times 2 - 1 =)$ 329 images.

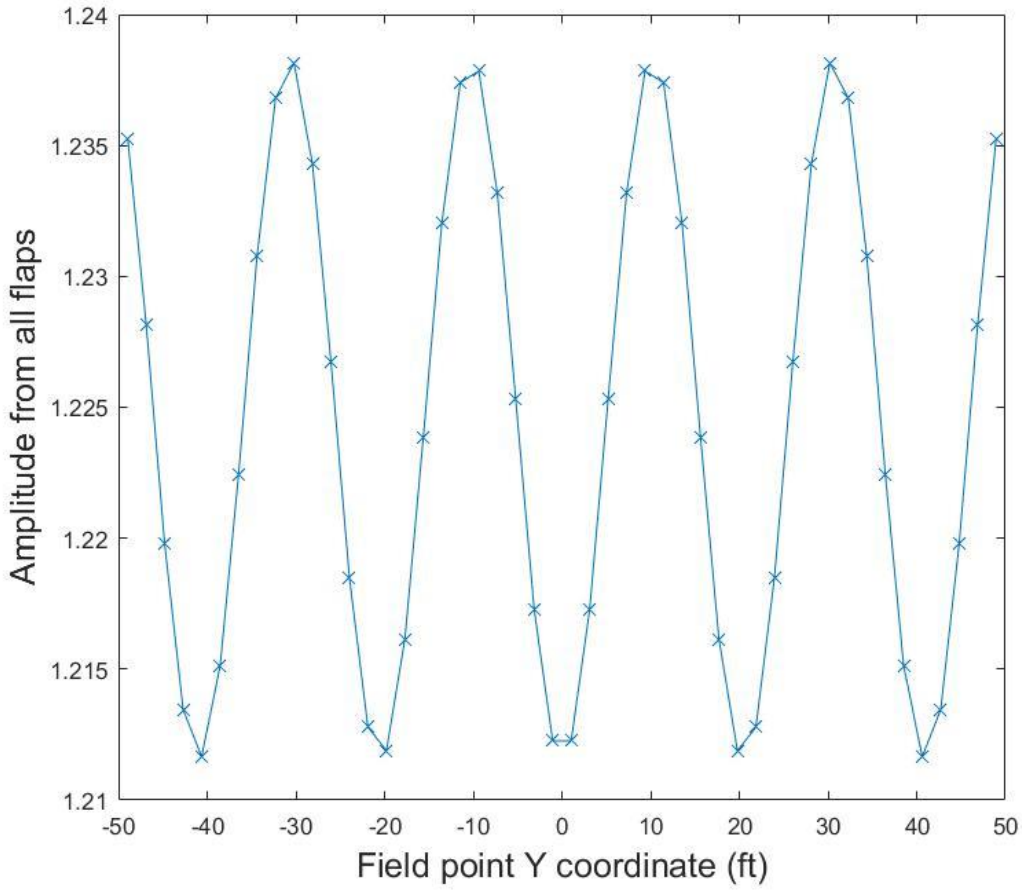

Figure 17 Amplitude by 165 images from all flaps at Period 2s

The level of amplitude variation for longer period is higher as compared to shorter period. But for period 4s, the level of amplitude variation is still within 4%, as shown in Figure 18.

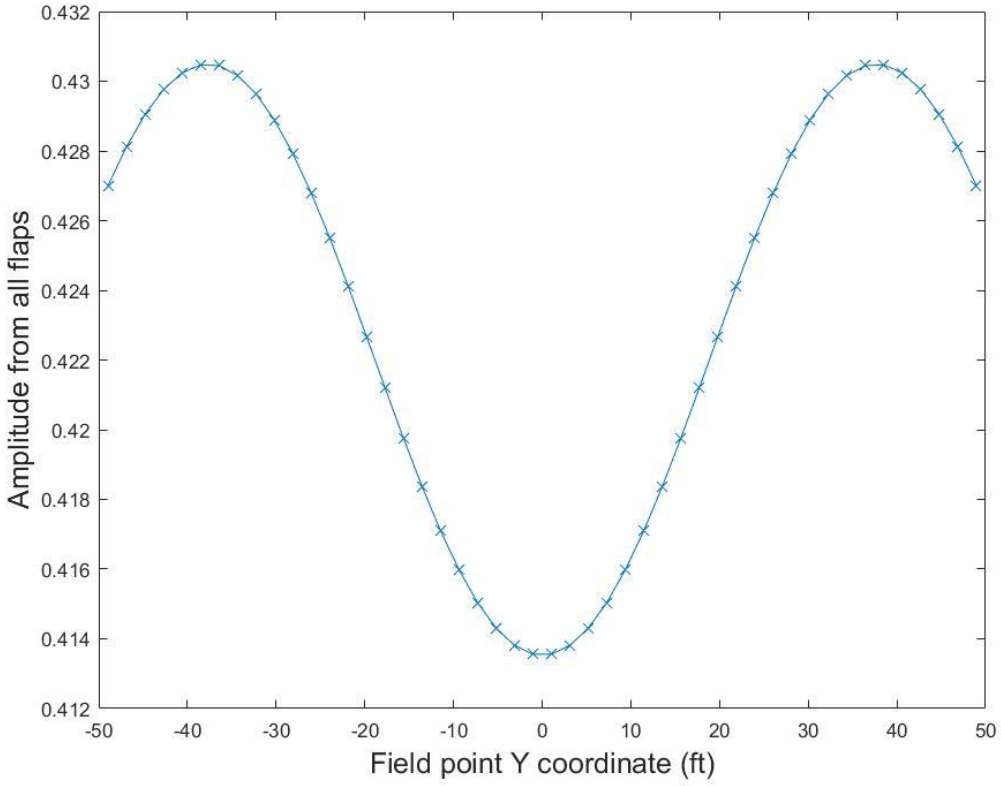

Figure 18 Amplitude by 165 images from all flaps at Period 4s

We can then increase the number of images by setting up a case with more field points. A case with $80{,}001 \times 50$ field points is run and parsed, which means in this case we have 50 rows of field points, and 80,001 points on each row. It gives the capability of including 1600 wavemaker images for calculation of wave elevation from 1’ to 50’ away

from the wavemaker. A convergence test is done similarly. Figure 19 shows the cumulative amplitude of 1600 wavemaker images at the row 25' away from the wavemaker. It can be seen that the elevation converges very fast in the first 200 images and converges slowly after that.

Even though it may not be readily apparent, the elevation is converging as we increase the number of images. This can be shown by the difference of upper and lower envelope being monotonically decreasing. Figure 20 shows the Gaussian fit of the difference elevation. It also represents this converging trend well. The difference decreases significantly for the first 200 images.

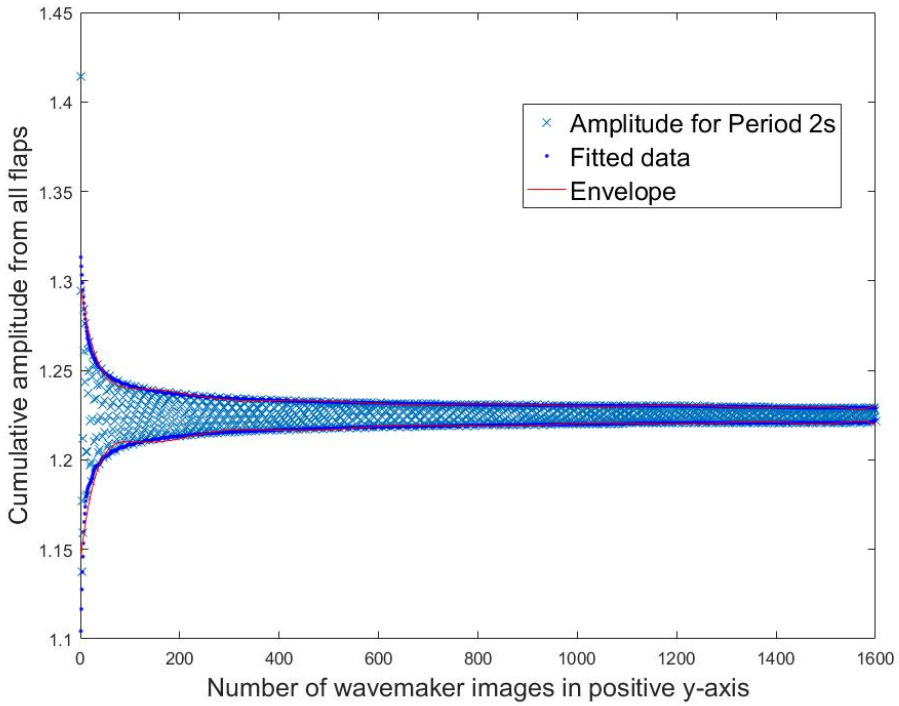

Figure 19 Cumulative amplitude from all flaps with envelope fitting for Period 2s for field point 25' away (up to 1600 images)

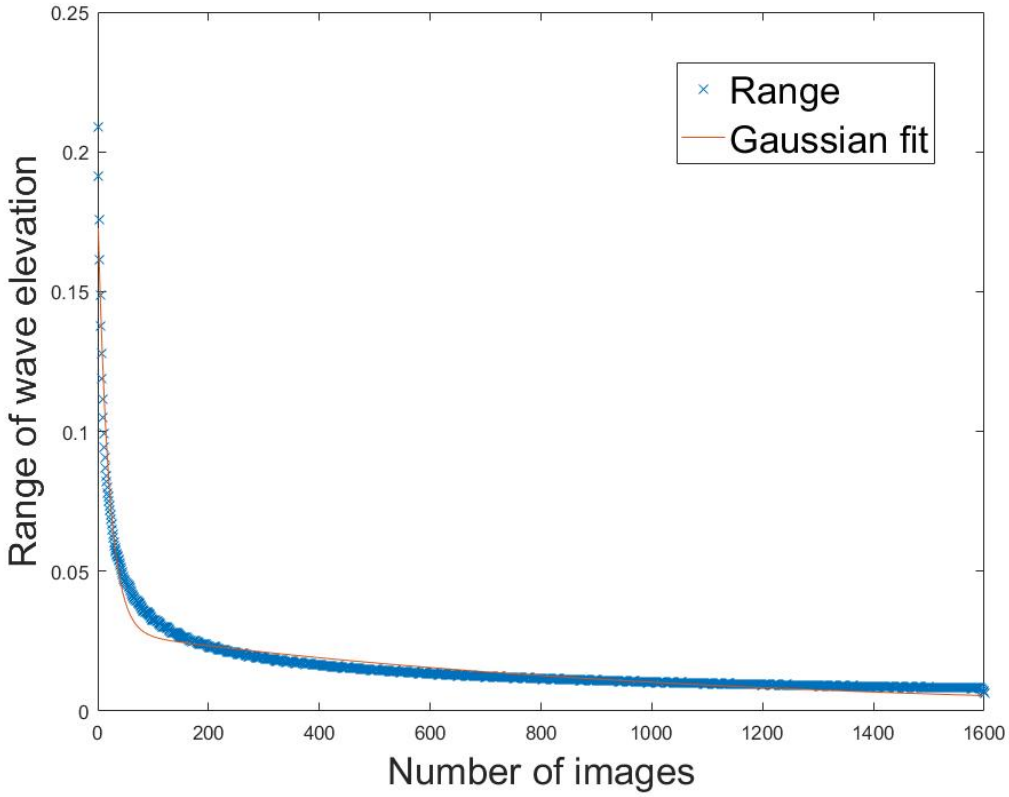

Figure 20 Gaussian fit of range of wave elevation (up to 1600 images) for Period 2s at field point (25', 1.0417')

Another field point at row 50' away from the wavemaker is selected. The cumulative elevation yields a similar result, as shown in Figure 21. And a similar table for 1600 images can be assembled showing the maximum number needed to reach the specified level of convergence for all points in a row, as shown in Table 3. The numbers larger than 1600 are determined based on extrapolation of the fitting function. The Gaussian fit of different field points across the transect is about the same as for the field points at row 25' away, as shown in Figure 15. So we can use the elevation result from

1600 images with confidence for at least 0.5% level of convergence, which is pretty good.

Moreover, 1600 images should be enough to simulate reflections from sidewalls. The cross-tank elevation amplitude transect is shown as Figure 22, which is the line of field points that are 50’ away from wavemaker. With 1600 images, the level of amplitude variation in the cross-tank transect is only about 0.5%.

Table 3 Number of images needed for convergence at 2s period based on model with 1600 images

Field point y-coordinate (ft)	2% convergence	1% convergence	0.5% convergence	0.1% convergence
1	31	76	627	2175
2	1	15	44	1051
3	11	31	72	1514
4	35	95	738	2275
5	42	193	880	2426
…	…	…	…	…
48	31	76	627	2175
MaxNumber	44	193	880	2466

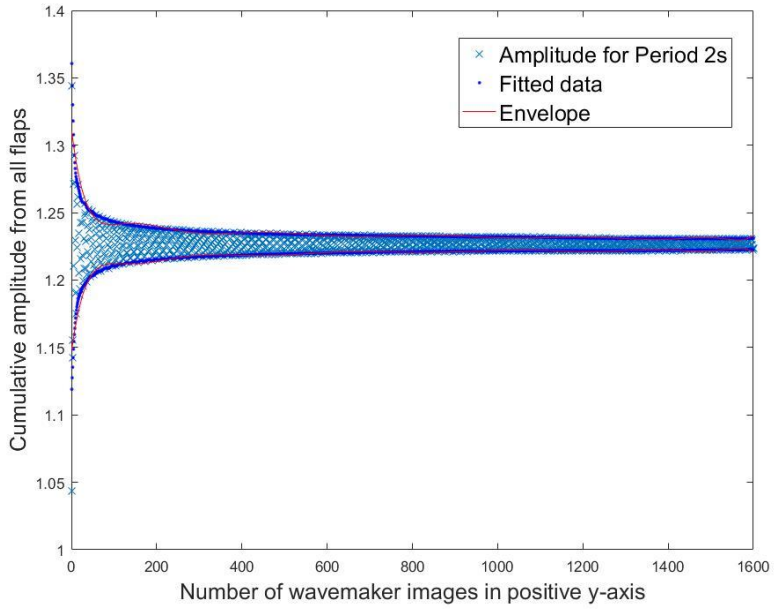

Figure 21 Cumulative amplitude from all flaps with envelope fitting for Period 2s for field point (50', 1.0417')

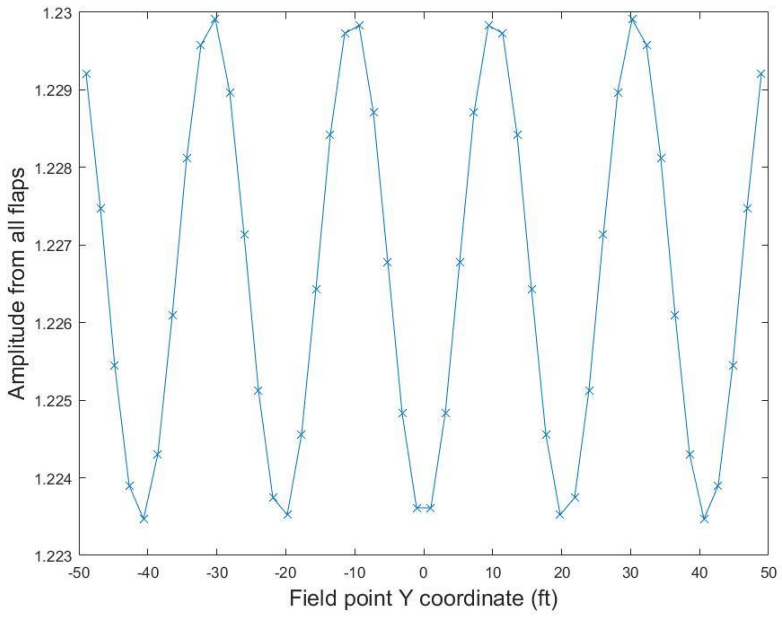

Figure 22 Amplitude by 1600 images from all flaps at Row 50' for Period 2s

5.2 Analysis of Evanescent Modes

In the wave propagation direction, the free surface elevation can be fitted with a sinusoidal model. This part corresponds to the propagating component. Since the wave frequency and wave number for each wave period are known, the amplitude of the sinusoidal model is the only variable in the curve fitting. Evanescent modes can be analyzed by subtracting the fitted sinusoidal model from the original free surface elevation. In principle the residual of the subtraction can then be fitted with a series of exponentially decaying evanescent modes. The theoretical wave numbers for evanescent modes are imaginary roots of the dispersion relation and thus are known for the curve fitting. The modal amplitude is the only variable. And the subtraction can be done recursively as each one of the evanescent modes is added into consideration.

We use the case with 400 images on a wave field 0' to 50' away from the wavemaker for the output. As mentioned above, 400 images should provide a relatively converged result of free surface elevation.

We first use sinusoidal functions to fit the real and imaginary components of the free surface elevation. To identify the propagating wave component, we examined the wave field in the domain 25' to 50' away from the wavemaker. The 25' distance from the wavemaker should be free of the elevation from evanescent modes. Both the real and imaginary components can fit perfectly in a sinusoidal function, shown as Figure 23 and Figure 24. Note that the sinusoidal fitting function is $a \times \sin(kx + \delta)$ where a is the amplitude to be determined, k is the wave number and δ is initial phase. For real component $\delta = 0$ and for imaginary component $= \frac{\pi}{2}$. So the amplitude a is the only

variable to be fitted. After fitting, we will have the sinusoidal function of the propagating component of the free surface elevation.

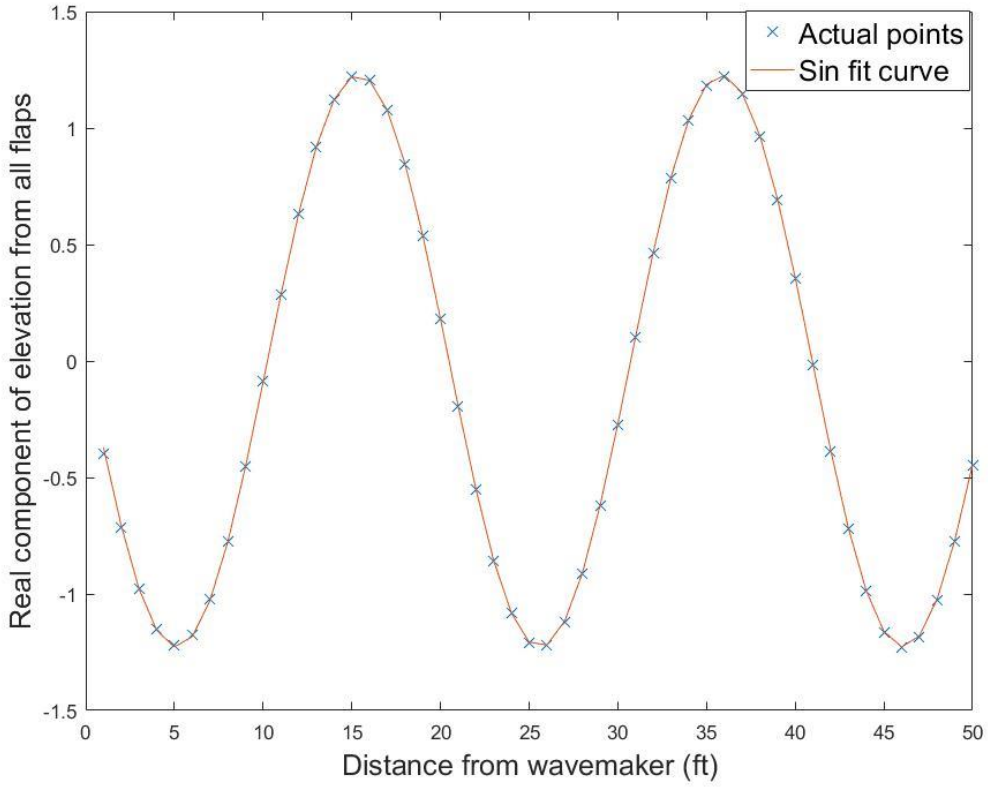

Figure 23 Real component of elevation by 400 images sin fit for Period 2s

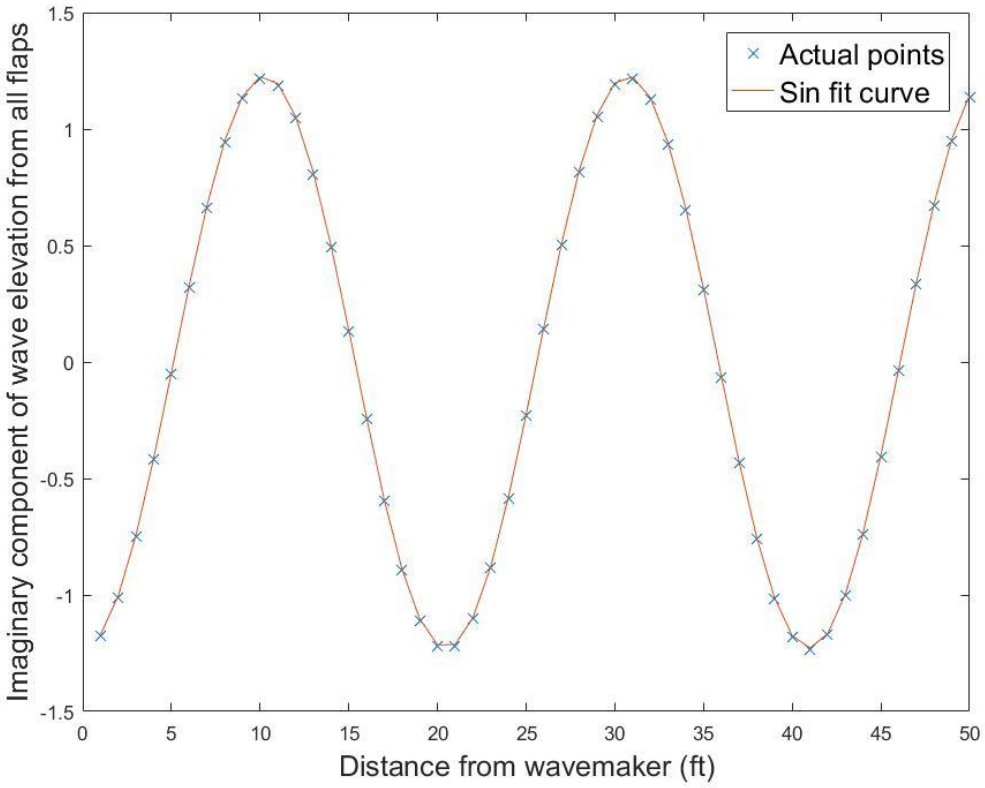

Figure 24 Imaginary component of elevation by 400 images sin fit for Period 2s

If we subtract the propagating component from the free surface elevation, the residual will be the standing wave component, corresponding to the summation of a series of evanescent modes. The evanescent modes are of the form

$$\sum a_i e^{-k_i x}$$

The theoretical wave numbers k_i for evanescent modes are the imaginary roots of the dispersion relationship and can be calculated. Only the amplitude a_i of the evanescent modes is to be determined.

We first fit the residual with the first evanescent mode, $a_1 e^{-k_1 x}$. After the amplitude a_1 for the first mode is identified, we can subtract the first evanescent mode from the residual, and fit the second residual with the second evanescent mode, $a_2 e^{-k_2 x}$. We 'peel off' the modes one by one and the residual decreases. This way we can demonstrate the dominating component of the evanescent modes.

Consider Period 4s as an example. Since the evanescent modes decay exponentially with the distance from the wavemaker flap, the evanescent modes should have less influence on the elevation at field points far away from the wavemaker compared to that at field points close to the wavemaker. Figure 25 and Figure 26 compare the sinusoidal wave elevation profile for the propagating wave, as identified from analysis of field points in the 25' to 50' range, with the total wave elevation results in the 0' to 50' range. As expected, the real component shows the exponentially decaying incremental wave elevation contribution associated with the evanescent modes in the 0' to 25' range.

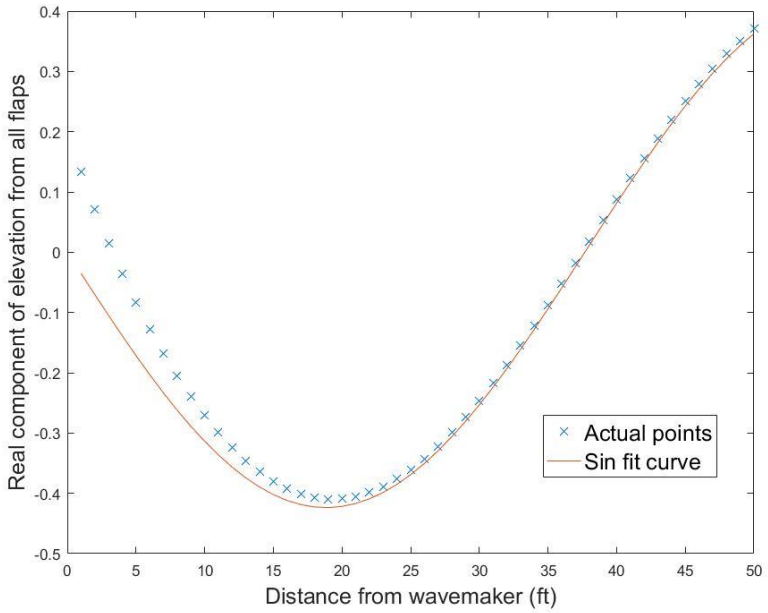

Figure 25 Real component of elevation by 400 images sin fit for Period 4s

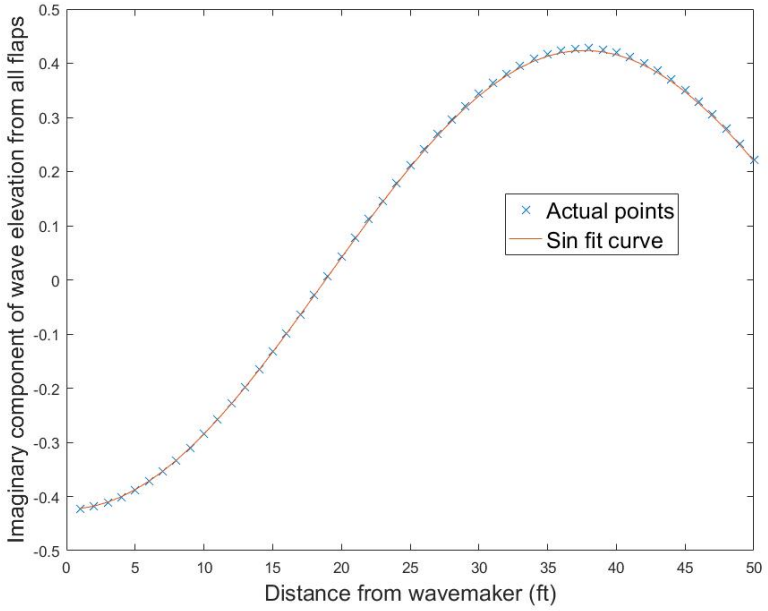

Figure 26 Imaginary component of elevation by 400 images sin fit for Period 4s

The sinusoidal fitting on the imaginary component of elevation is very good. From the residual of subtracting propagation elevation, we can see that the difference is at the level of 10^{-3}, which can be considered as noise. So only the real component of elevation is processed for evanescent mode analysis. The first residual and evanescent mode fit is shown as in Figure 27. From the first residual plot Figure 27, we can see that the evanescent mode function fits the residual curve well and it is exponentially decaying to a very small value in the distance from 0’ to 25’ away, which in some respect validates our method to fit a sinusoidal function for the propagating mode to field points from 25’ to 50’ away.

As determined from the numerical model, the minimum distance of 25’ from the wavemaker should be adequate for free surface elevations to be free from the influence of evanescent modes. The evanescent mode is shown to exist in the free surface elevation caused by wavemaker flaps and is only affecting the area close to the wavemaker. The exponentially decaying curve corresponds to the evanescent mode theory as well.

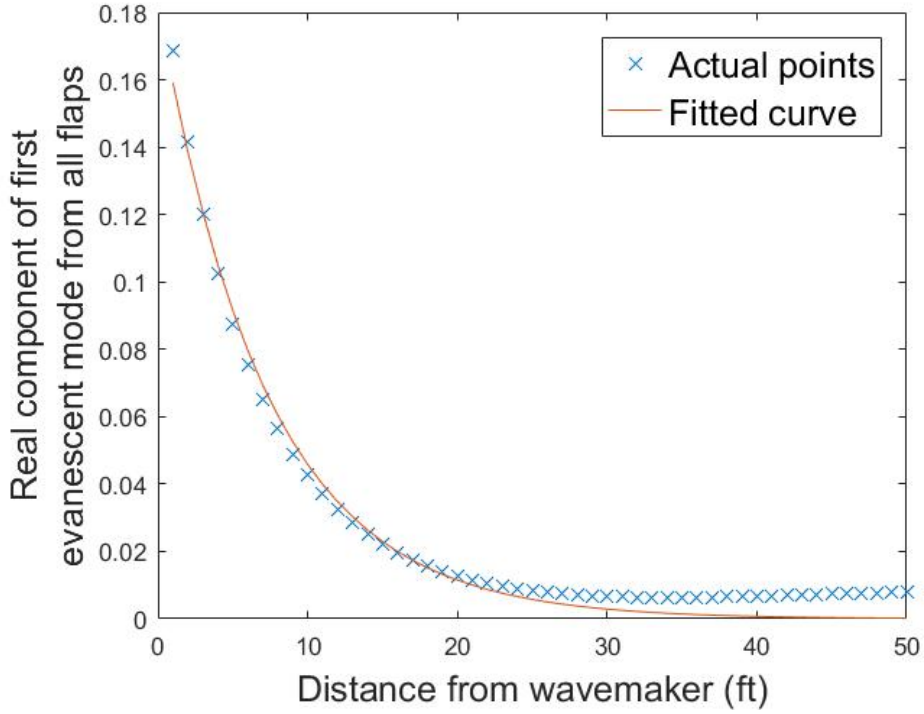

Figure 27 Real component of first evanescent mode fit by 400 images at Column 24 (*y*=-1.0417') for Period 4s

The second residual and evanescent mode fit is shown in Figure 28. From the second residual plot Figure 28, we can see that the first evanescent mode is dominating and the second residual is at a level of 10^{-3}, which can be considered as noise. If we look back at the first residual and evanescent mode fit in Figure 27, we can see that beyond 25' the residual is not decaying exponentially. Instead, it is almost a constant at a very small level (10^{-3}). This can be due to the accuracy limit in this method of images. There is loss of precision when the method of images is adopted because of the accumulating error over the larger number of image contributions that need to be summed. If we subtract that noise from the first exponentially decaying evanescent mode, we will not

get an exponentially decaying curve. Thus, we cannot fit the second residual with an evanescent mode model.

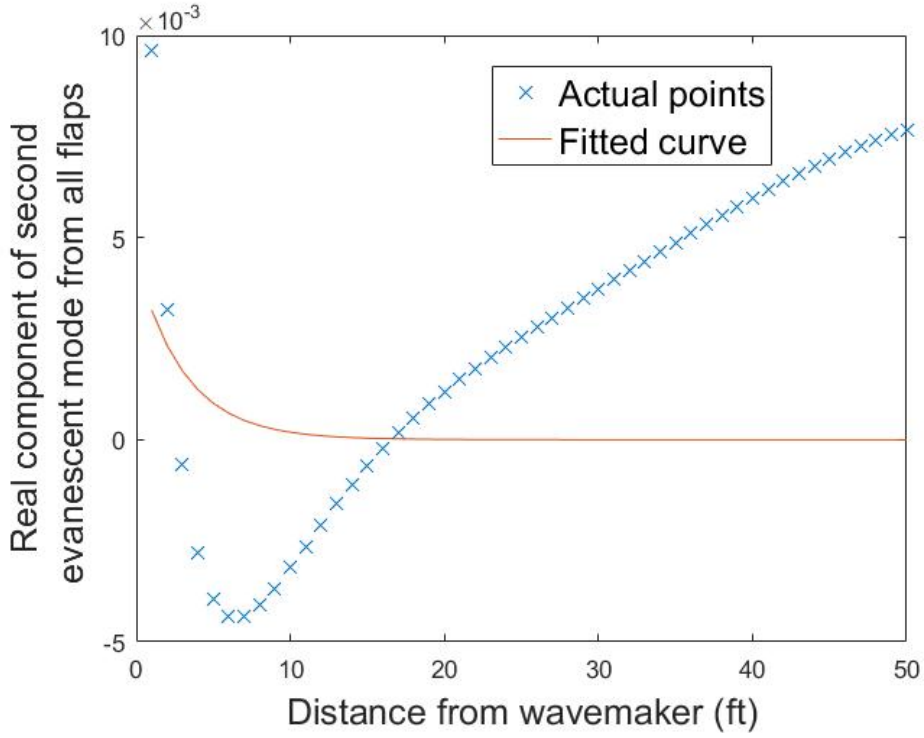

Figure 28 Real component of second evanescent mode fit by 400 images at Column 24 (*y*=-1.0417') for Period 4s

Alternatively, we can also fit the residual with a series of evanescent modes in one plot. We just need to fit the first residual with a series of exponentially decaying functions and the curve fitting function in Matlab will determine the amplitude $(a_1, a_2 \ldots)$ for each mode. But it will not be as accurate as the previous 'peel-off' method and it will not show a dominating component of the first evanescent mode as clearly.

The evanescent modes for all other periods were processed and similar results were obtained. For example, Figure 29 shows the first evanescent mode identified for 3s period.

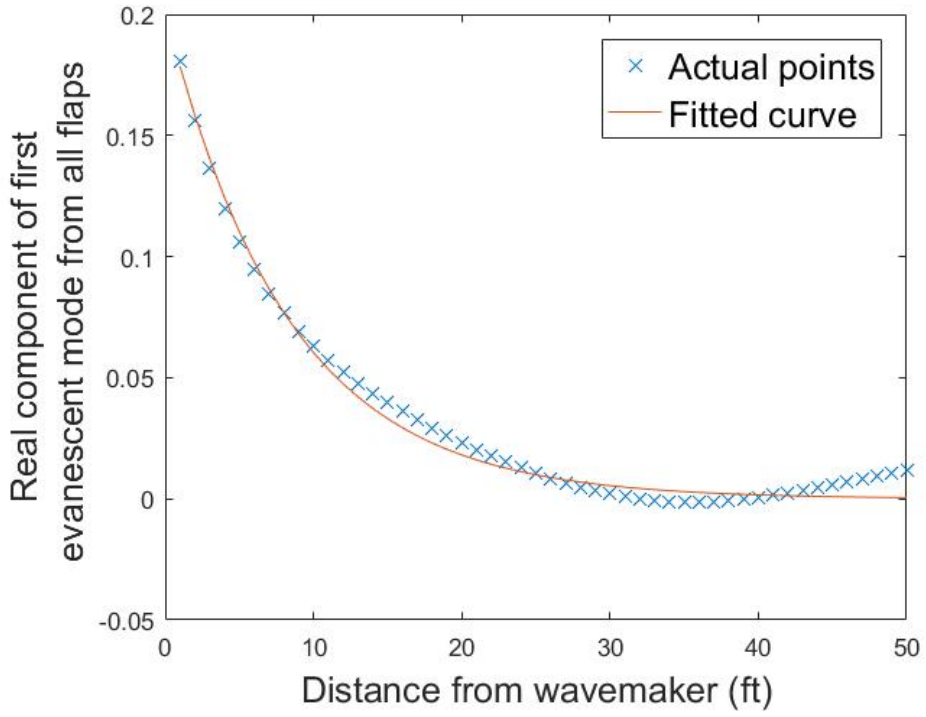

Figure 29 Real component of first evanescent mode fit by 400 images at Column 24 (*y*=1.0417') for Period 3s

5.3 Non-oblique Wave Generation

Since the wave elevation from all the wavemaker flaps for the entire wave field is stored in the matrix $\eta_s(x_0, y_0)$, we can use the 'surf' function to generate an instantaneous wave elevation surface in Matlab.

The real component of the elevation represents the surface elevation at the phase point ωt =0. Thus, the real component can be plotted to show a surface of wave elevation. Figure 30 shows the elevation surface for Period 2s. We can see that the wave is long crested and is almost uniform across the tank. An elevation surface of the extended wave field from 0' to 100' away is shown in Figure 31. The uniformity remains in the extended wave field.

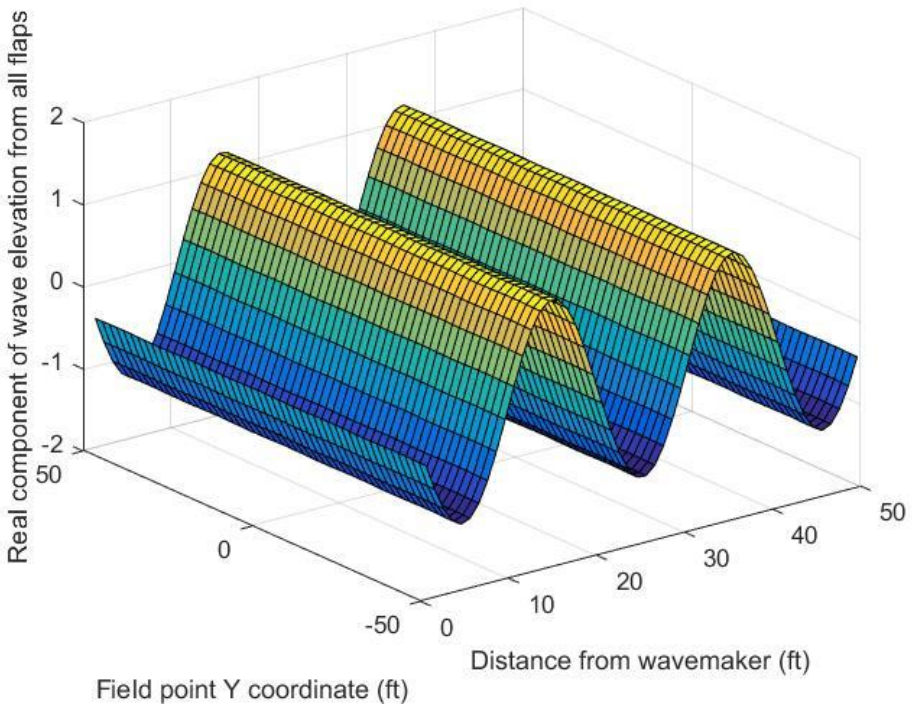

Figure 30 Surface of real component of wave elevation from 1600 images from all wave flaps for Period 2s

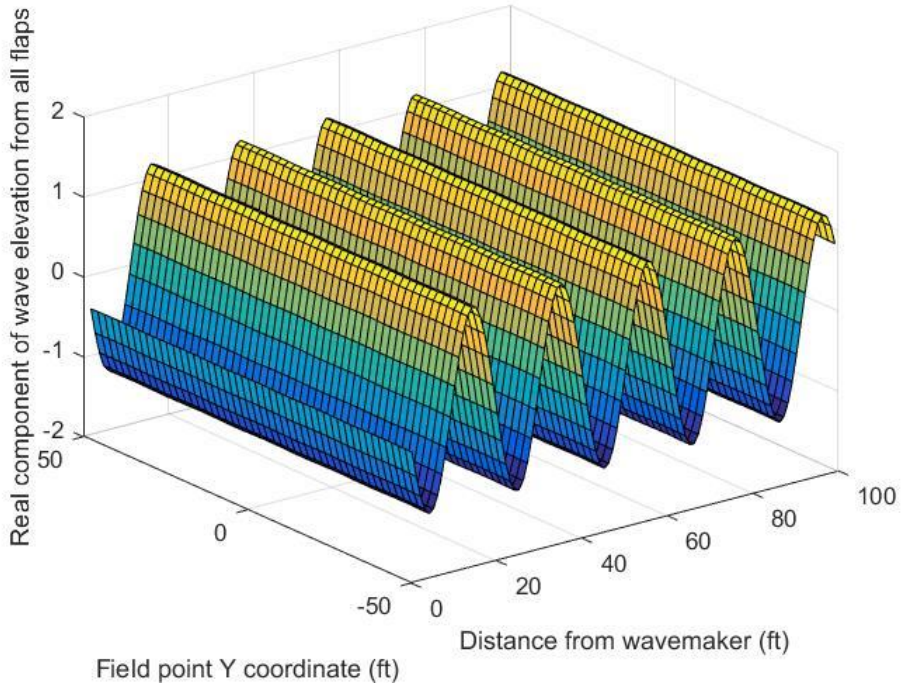

Figure 31 Surface of real component of wave elevation from 1600 images from all wave flaps for Period 2s - extended domain

The surface for the imaginary component is similar to that for the real component except for a phase shift. The movie of the propagating wave can be created by applying the phase information to the real and imaginary components as $Re\,cos(\omega t) - Im\,sin(\omega t)$. The movie is a series of instantaneous surface plots presented at a frame rate during a period.

5.4 Oblique Wave Generation

The oblique wave field is generated in a manner similar to the non-oblique wave field. The wave propagation angle θ is defined as the angle between the positive x-axis of the global coordinate system and the direction in which the wave propagates. Based on the relation $k_0 = k \cdot sin\,\theta$ from the snake principle, a phase shift is applied on each

wavemaker flap. Due to the finite width of wavemaker flaps, the phase of the wavemaker flap is represented by the phase at the center of the wavemaker flap in a continuous wavemaker array. A phase shift of $k_0 \cdot y$ is added or subtracted in the phase information while generating the free surface elevation, where *y* is the y-coordinate of the center of each wavemaker flap and the sign of the phase depends on the direction of the sinusoidal movement of the wavemaker flaps.

Since different wavemaker flaps have different coordinates y_i, the total wave elevation is then a summation of all wavemaker flaps. A video of a progressive oblique wave field can then be made with different phase on different wavemaker flaps. The surface elevation for the oblique wave is determined by

$$\sum_{i=1}^{N_f} Re_i \, cos(\omega t - k_0 y_i) - Im_i \, sin(\omega t - k_0 y_i)$$

where Re_i and Im_i correspond to the real and imaginary components of wave elevation from i^{th} wavemaker flap and its images.

We can generate an oblique wave field by using the elevation information stored in the matrix η_{rcq}. It contains the elevation contribution from each wavemaker flap on the entire wave field. Thus, we can apply different phases to different wavemaker flaps according to the oblique wavemaker theory. The wave angle θ is chosen in consideration of the distribution of field points. We try to have as many field points as possible fall precisely on the line of the wave front, which is perpendicular to the wave direction. The field points are separated by 1' in x direction and $\frac{25}{12}$' in y direction. So a series of wave angles θ can be selected based on the value of $\tan\theta$.

Table 4 shows the wave angles being studied in this research and how they are calculated. Note that wave angle with zero degree should produce the same result as in the non-oblique wave case, which is validated. The difference of the results from these two methods is at the 10^{-15} level.

Table 4 Selection of oblique wave angles

Calculation	Ratio of tan θ	θ in radians	θ in degrees
0	-	0	0
atan(0.96)	12/25/1*2	0.7650	43.8309°
atan(0.72)	12/25/2*3	0.6240	35.7539°
atan(0.48)	12/25/1	0.4475	25.641°
atan(0.32)	12/25/1.5	0.3097	17.7447°
atan(0.24)	12/25/2	0.2355	13.4957°
atan(0.16)	12/25/3	0.1587	9.0903°
atan(0.12)	12/25/4	0.1194	6.8428°
atan(0.096)	12/25/5	0.0957	5.4836°
atan(0.08)	12/25/6	0.0798	4.5739°
atan(0.048)	12/25/7	0.0480	2.7481°

Figure 32 shows an example of an oblique wave field with an angle of 25.641° for period 2s. The uniformity of the surface elevation across the wave front is related to the angle of wave propagation. This can be shown through a series of oblique wave

surface plots, provided as Figure 33 to Figure 36 below, with the wave angle decreasing as we get closer to the non-oblique wave case.

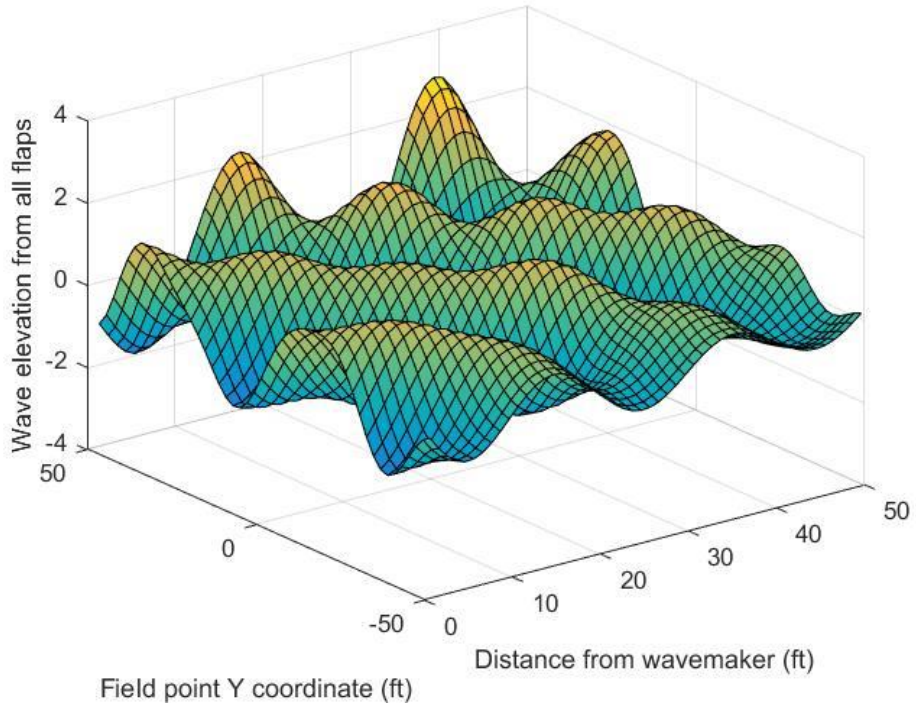

Figure 32 Oblique wave at θ = 25.641° from 1600 images for Period 2s

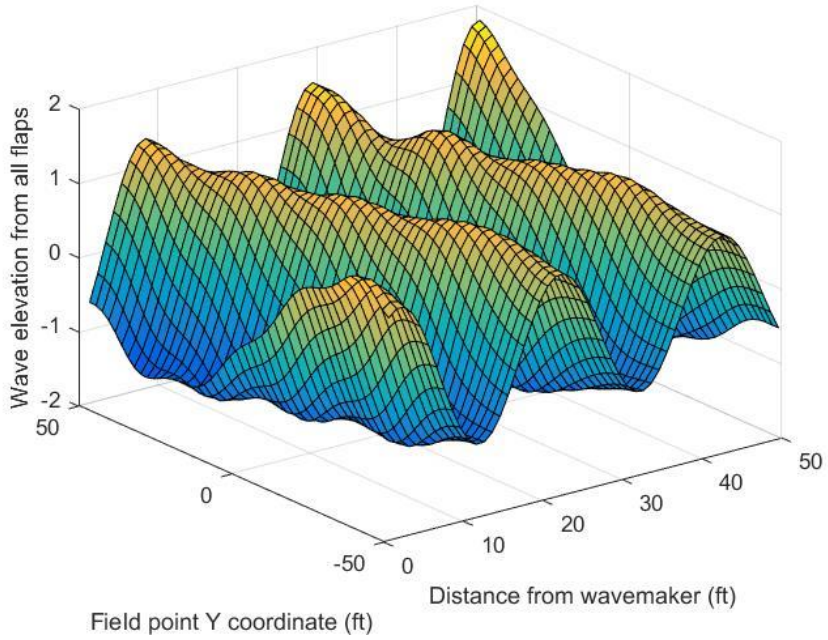

Figure 33 Oblique wave at θ = 9.0903° from 1600 images for Period 2s

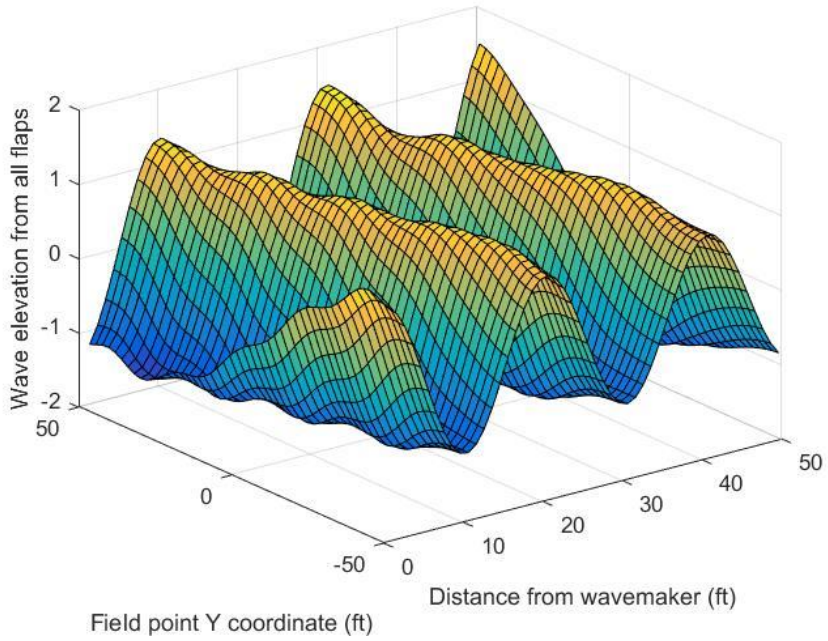

Figure 34 Oblique wave at θ = 6.8428° from 1600 images for Period 2s

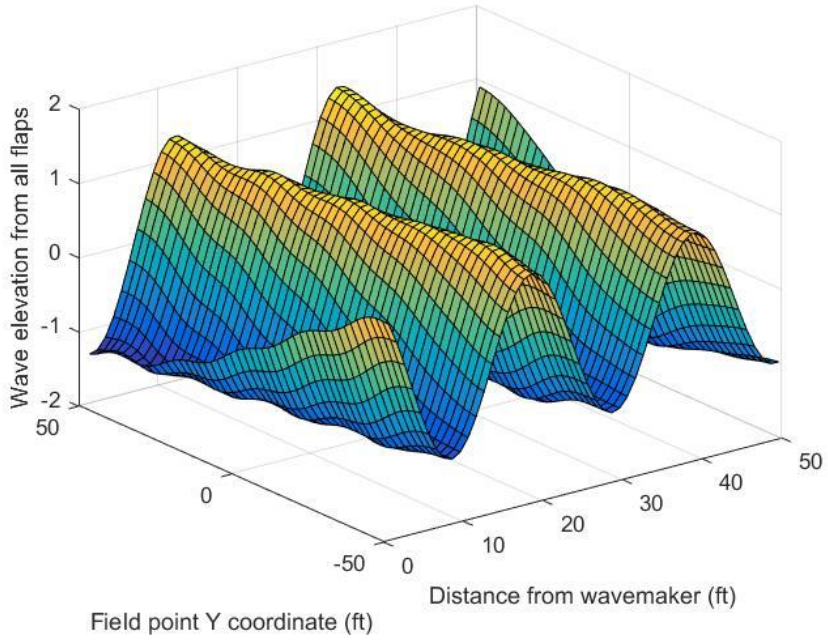

Figure 35 Oblique wave at θ = 4.5739° from 1600 images for Period 2s

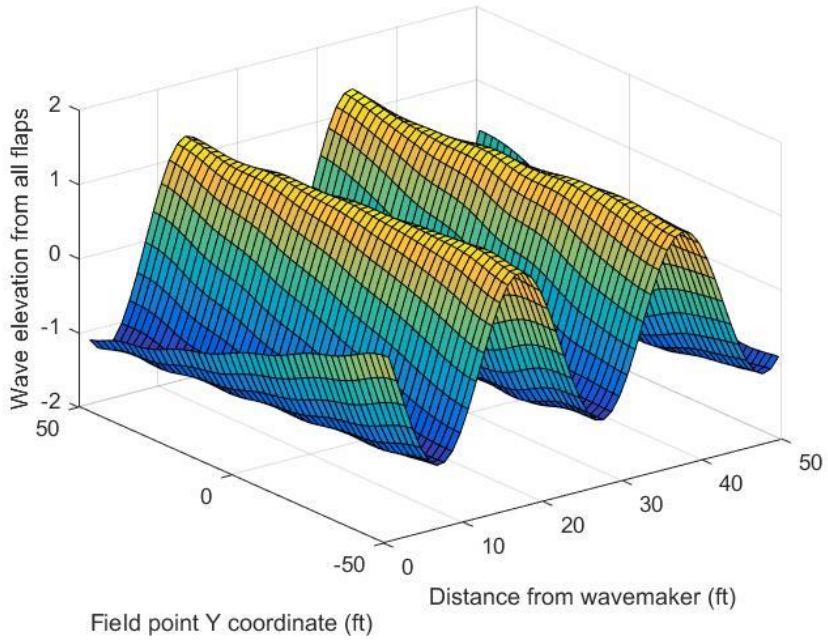

Figure 36 Oblique wave at θ = 2.7481° from 1600 images for Period 2s

To have a clearer view of the wave elevation across the wave front, we can check whether the oblique wave is propagating in the designated wave angle and how the elevation is distributed along the line of field points parallel to the wave front. For an instantaneous oblique wave surface, a transect of the propagating oblique wave can be plotted to show the cross-tank oscillation. The wave angle is selected so that we can find exact field points lying on a line that is perpendicular to the wave propagation direction. The elevations on these points will then show the difference across the wave field, as shown in Figure 37. This is especially important because we want to maintain a homogeneous sea state in the test area even in oblique waves.

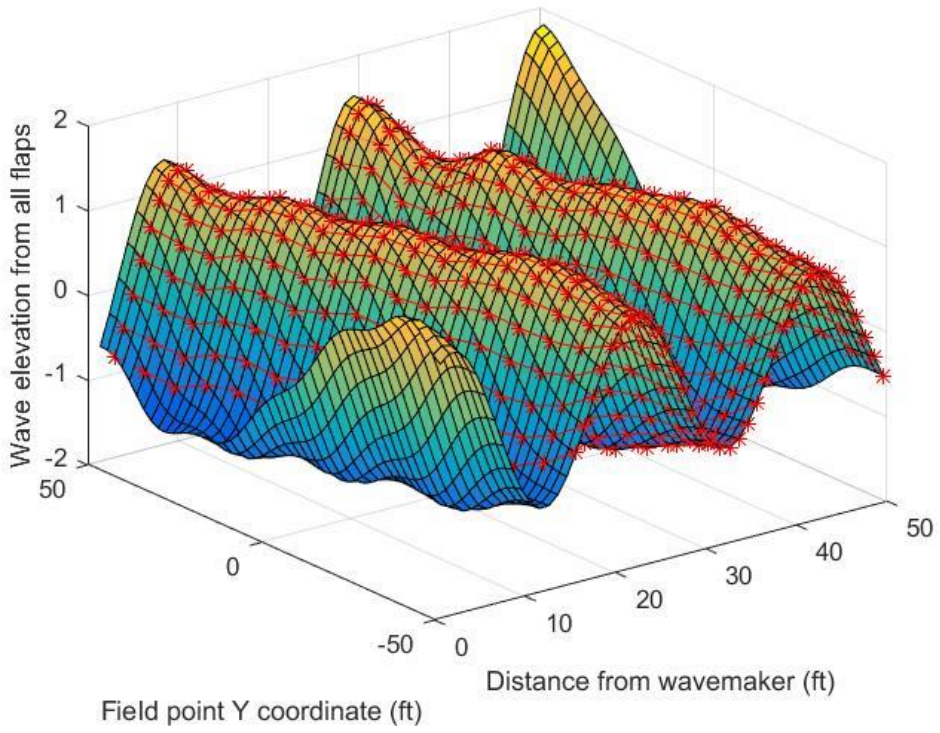

Figure 37 Oblique wave at θ = 9.0903° from 1600 images for Period 2s (showing with field points)

A contour plot of the wave field can also be examined. It can show the linearity of the oblique wave front and the uniformity of the wave field. We can check the wave propagation direction and see whether the crests are aligned parallel to the wave front. Both the instantaneous surface elevation and the amplitude of the surface elevation can be plotted in the contour plots. A series of contours of the oblique wave surface for Period 2s are plotted for the phase point $\omega t = 0$, presented from Figure 38 to Figure 41. The points on the plot form parallel lines that are perpendicular to the wave propagation direction.

If the wave is propagating in the designated direction and the wave elevation is uniform across the wave front, the contours should lie on the points in a line. We can see that this uniformity for the entire wave field is better for smaller wave angles. As we increase the wave angle, the wave field becomes less uniform and the drawback of the snake principle starts to appear. The discrete finite width wavemaker flap may not produce oblique wave accurately based on the snake principle. In addition, the reflection from the side walls has more influence on the contours. The wave field is more nonuniform in the area closer to the tank sidewall. As a comparison, the contour plot of the extended wave field is shown in Figure 42 for $\theta = 9.0903°$ and Figure 43 for $\theta = 0°$. We can see that in the case of non-oblique wave $\theta = 0°$, the contour consists of straight lines. The wave field is not disturbed at all since there is no reflection effect from the side walls. In the case of an infinite long wall of wavemakers without side wall reflection, the generated oblique wave will also be uniformly long crested.

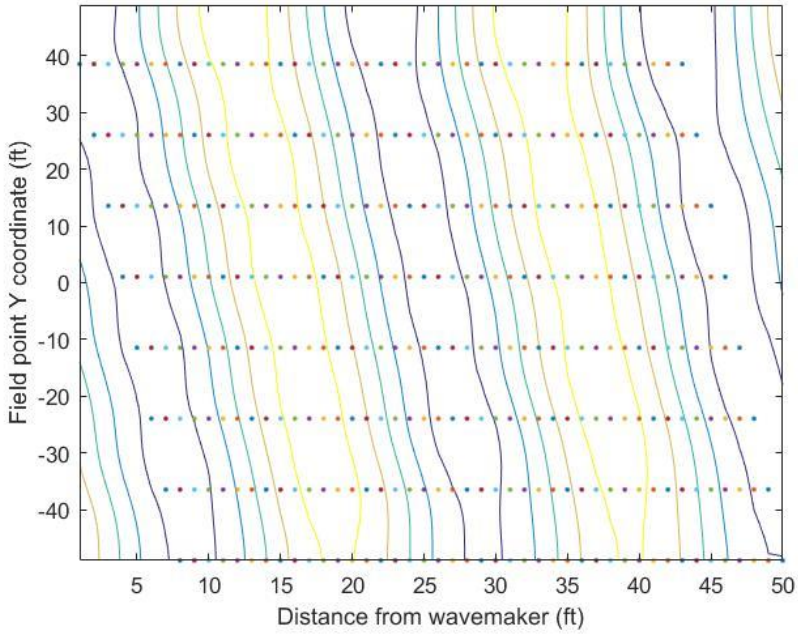

Figure 38 Contour plot at θ = 4.5739° for Period 2s

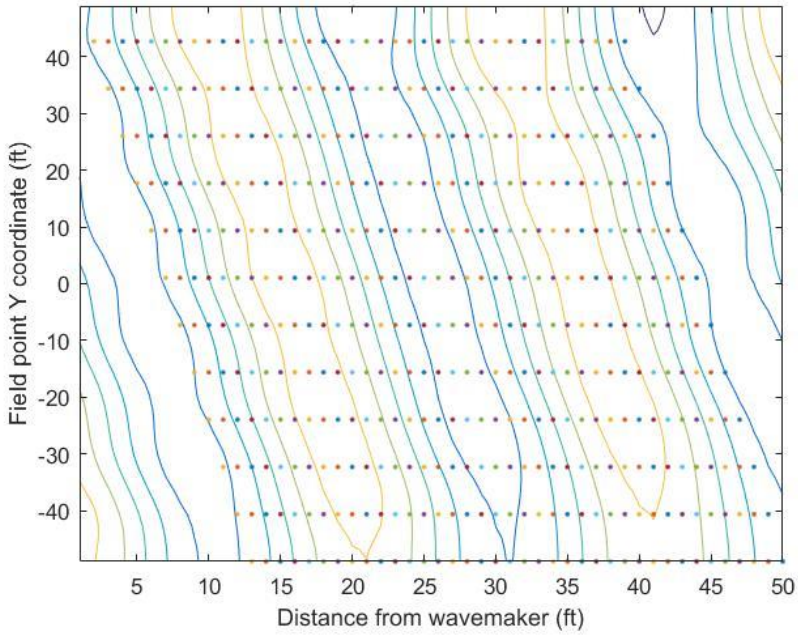

Figure 39 Contour plot at θ = 6.8428° for Period 2s

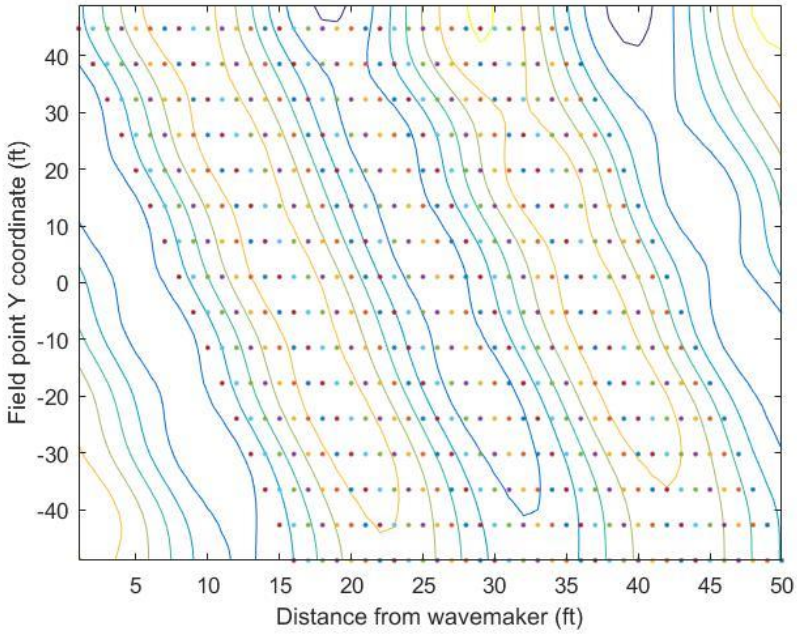

Figure 40 Contour plot at θ = 9.0903° for Period 2s

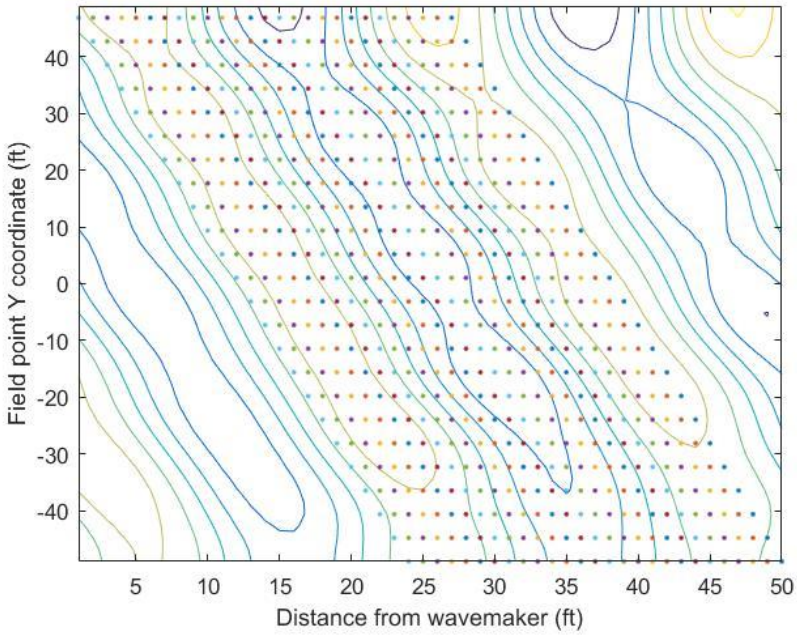

Figure 41 Contour plot at θ = 13.4957° for Period 2s

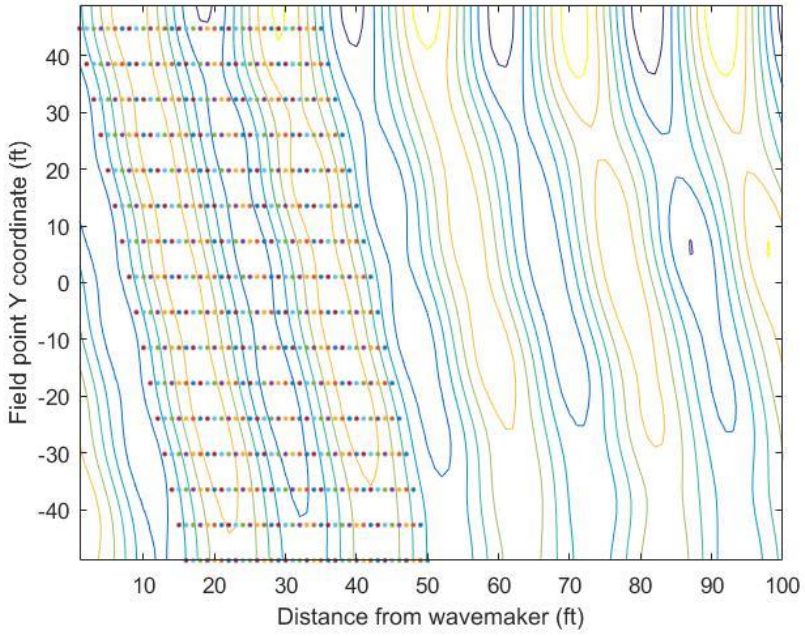

Figure 42 Contour plot at θ = 9.0903° for Period 2s - extended domain

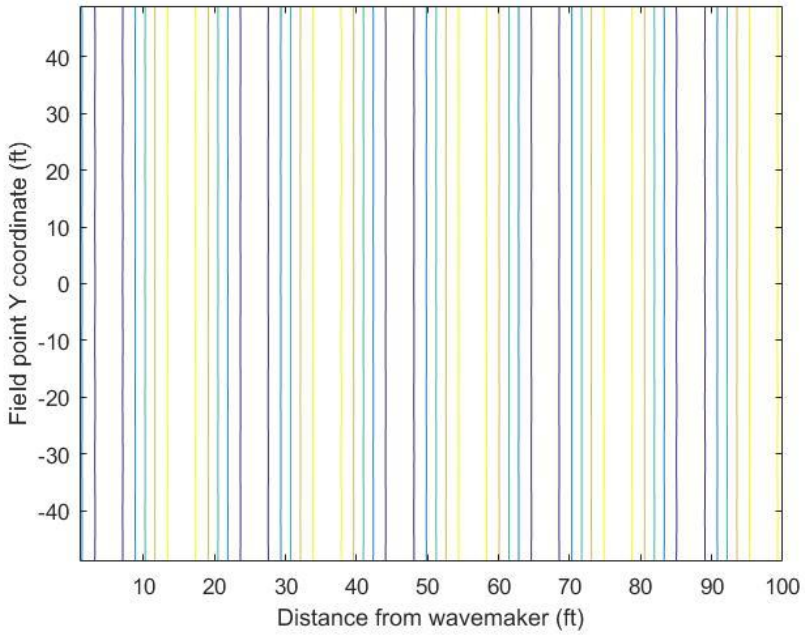

Figure 43 Contour plot at θ = 0° for Period 2s - extended domain

In the case of oblique wave generation, we are most concerned with the uniformity of wave elevation in the test area, where the pit is located. A line of points within the pit area can be selected and a plot of the free surface elevation amplitude along the line of points can be used to check the uniformity in the test area. The variation can be calculated.

The pit is centered at (53.5',0') in the wave field. A line of field points passing through the center of the pit is selected. The other two lines of field points are 7' further away from the wavemaker and 7' closer to the wavemaker, providing a square test area with edge length of 15'.

Because different wavemaker flaps have different phase, the amplitude is calculated from a summation of real and imaginary components of different wavemaker flaps.

$$\sum_{i=1}^{N_f} Re_i\, cos(\omega t - k_0 y_i) - Im_i\, sin(\omega t - k_0 y_i)$$

$$= \sum_{i=1}^{N_f} Re_i(cos(\omega t)\cos k_0 y_i + sin(\omega t)\sin k_0 y_i)$$

$$- Im_i\,(sin(\omega t)\cos k_0 y_i - cos(\omega t)\sin k_0 y_i)$$

$$= \sum_{i=1}^{N_f} (Re_i \cos k_0 y_i + Im_i \sin k_0 y_i)\cos \omega t$$

$$+ (Re_i \sin k_0 y_i - Im_i \cos k_0 y_i)\sin \omega t$$

The amplitude is then

$$\sqrt{\left(\sum_{i=1}^{N_f}(Re_i \cos k_0 y_i + Im_i \sin k_0 y_i)\right)^2 + \left(\sum_{i=1}^{N_f}(Re_i \sin k_0 y_i - Im_i \cos k_0 y_i)\right)^2}$$

The surface elevation amplitudes along these transects are calculated and plotted in the same figure. As documented above, better uniformity is achieved for longer periods. But to be consistent with the previous analysis, the results for Period 2s are presented in Figure 44 to Figure 48. And the amplitude for zero degree wave angle, which is the non-oblique wave, is shown in Figure 49 for Period 2s and in Figure 50 for Period 3s for comparison.

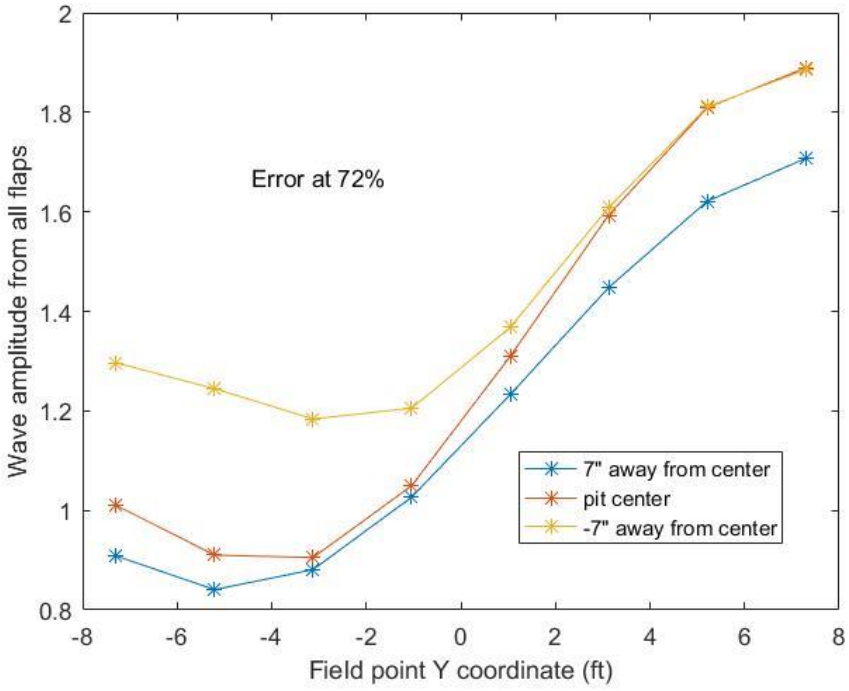

Figure 44 Amplitude in test area at θ = 25.641° for Period 2s

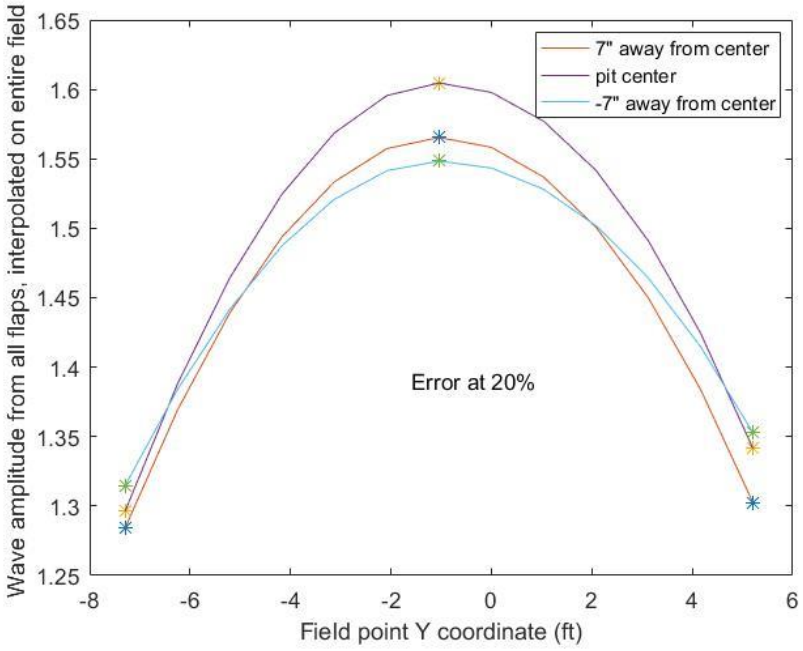

Figure 45 Amplitude in test area at θ = 17.7447° for Period 2s

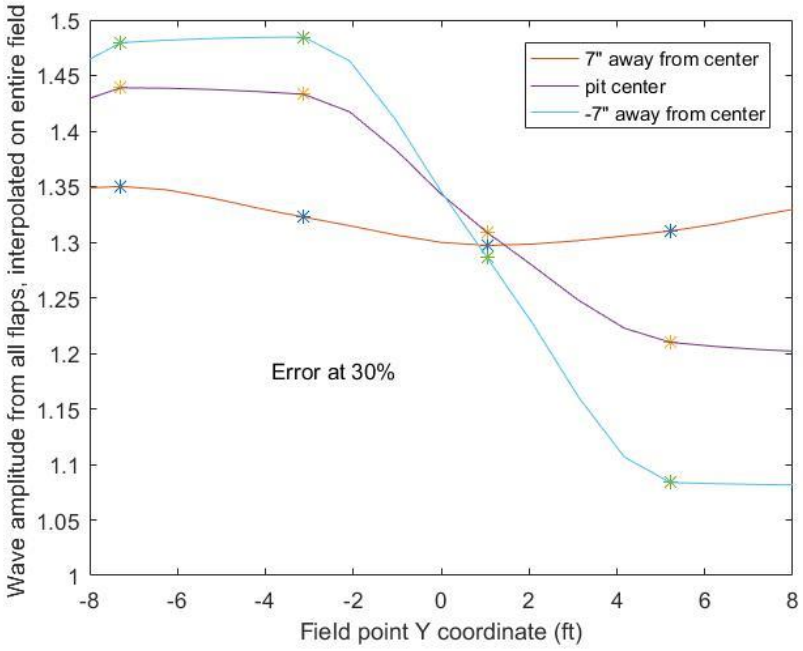

Figure 46 Amplitude in test area at θ = 13.4957° for Period 2s

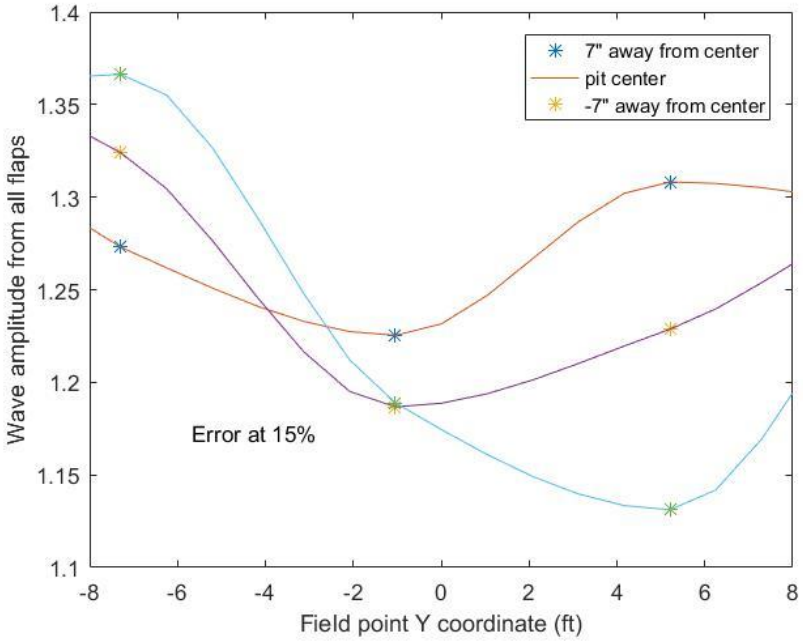

Figure 47 Amplitude in test area at θ = 9.0903° for Period 2s

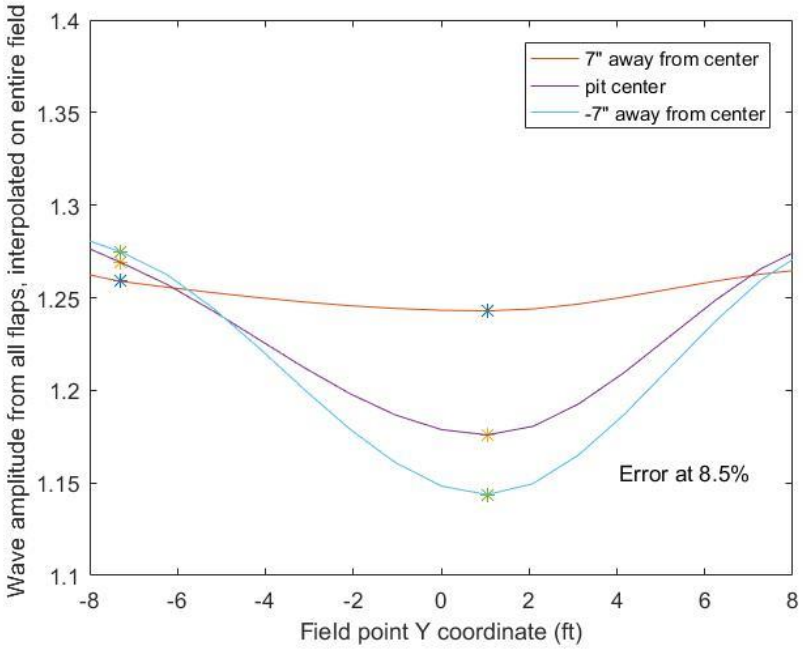

Figure 48 Amplitude in test area at θ = 6.8428° for Period 2s

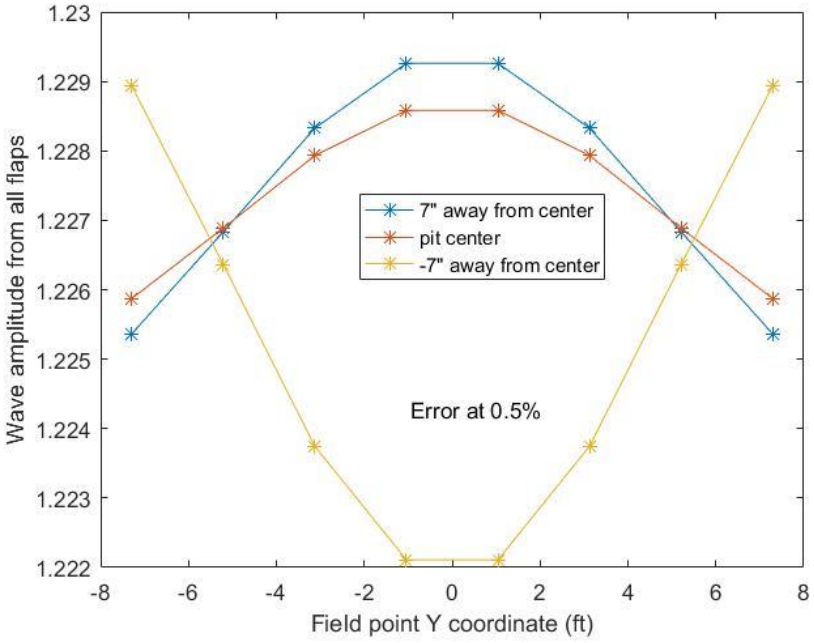

Figure 49 Amplitude in test area at $\theta = 0°$ for Period 2s

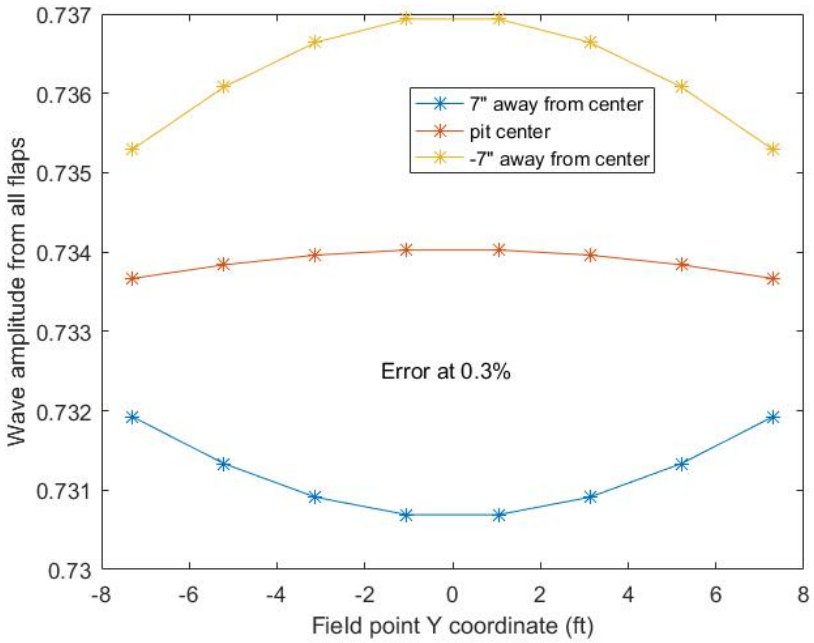

Figure 50 Amplitude in test area at $\theta = 0°$ for Period 3s

As we increase the wave angle, the variation in amplitude across the test area becomes larger and larger. If we have a wave angle larger than 10°, we may have a variation level higher than 10%. The quality of the results processed in this wave condition will be degraded. Note that, as stated in the literature review in Chapter I, Funke and Miles (1987) developed an extension of the snake principle known as the corner reflection method which is able to obtain a larger test area, or equivalently, obtain better uniformity over a given test area. Although this corner reflection method is routinely used in oblique wave generation in the OTRC basin, it has not been investigated herein.

5.5 Exciting Force on a Bottom-founded Cylinder for 0° Wave Angle

For the purpose of illustrating how the exciting force on a body in the test area can be calculated, we study a bottom-founded, surface piercing circular cylinder with a radius of 1.5'. Both theoretical results of exciting force and results from WAMIT output are considered and plotted. In the case of theoretical exciting force analysis, the exciting force is due to incident waves of different periods and the phase of the force is referenced to the center of the cylinder. The theoretical result is based on MacCamy and Fuchs' theory.

One case of calculating the exciting force on the bottom-founded cylinder is run in WAMIT for an open ocean situation (without basin side walls or wavemaker). This result is compared with the theoretical force. Another case is run using wavemaker flaps with the method of images to generate waves and calculate the exciting force on the cylinder including the effect of basin side wall reflections. In this case, twenty-four flaps

are used for wavemakers because of symmetry about the centerline of the wave tank. In the WAMIT input, images of the circular cylinder are used to account for the side wall reflection of the waves scattered by the cylinder. Thus, an array of cylinders is used and the individual exciting force influence on each cylinder from each wavemaker flap is calculated. Due to the time limitations, a convergence test was not performed for the exciting force analysis using the method of images. However, the comparison of the WAMIT calculation with the theoretical result for the open ocean case serves to confirm that the selected number of cylinder images is reasonable.

In the case of non-oblique waves, all of the wavemaker flaps are in phase. The total exciting force is a linear superposition of all wavemaker flaps multiplied by a factor of two, because of symmetry about the x-axis. Since the summed exciting forces are stored in matrices with respect to wavemaker flaps and periods, we can then calculate the total exciting force on the circular cylinder by summing the matrices associated with individual wavemaker flaps.

A plot of non-dimensional exciting force vs periods can be drawn. The theoretical exciting force magnitude for the open ocean case is calculated as

$$F = \frac{2\rho g H a h}{ka\sqrt{J'^2_1(ka) + Y'^2_1(ka)}} \frac{tanh(kh)}{kh}$$

The open ocean case with incident waves propagating from minus infinity toward the cylinder is performed in WAMIT and the magnitude of the resulting exciting force is plotted and compared with the theoretical case as shown in Figure 51. For the theoretical force, eight points of exciting force from Period 0.5s to 4s are calculated based on

known wave numbers from WAMIT output and the points are joined through interpolation. The result of the open ocean case in WAMIT shows excellent agreement with the theoretical calculation. The difference is only at a level of 10^{-4}.

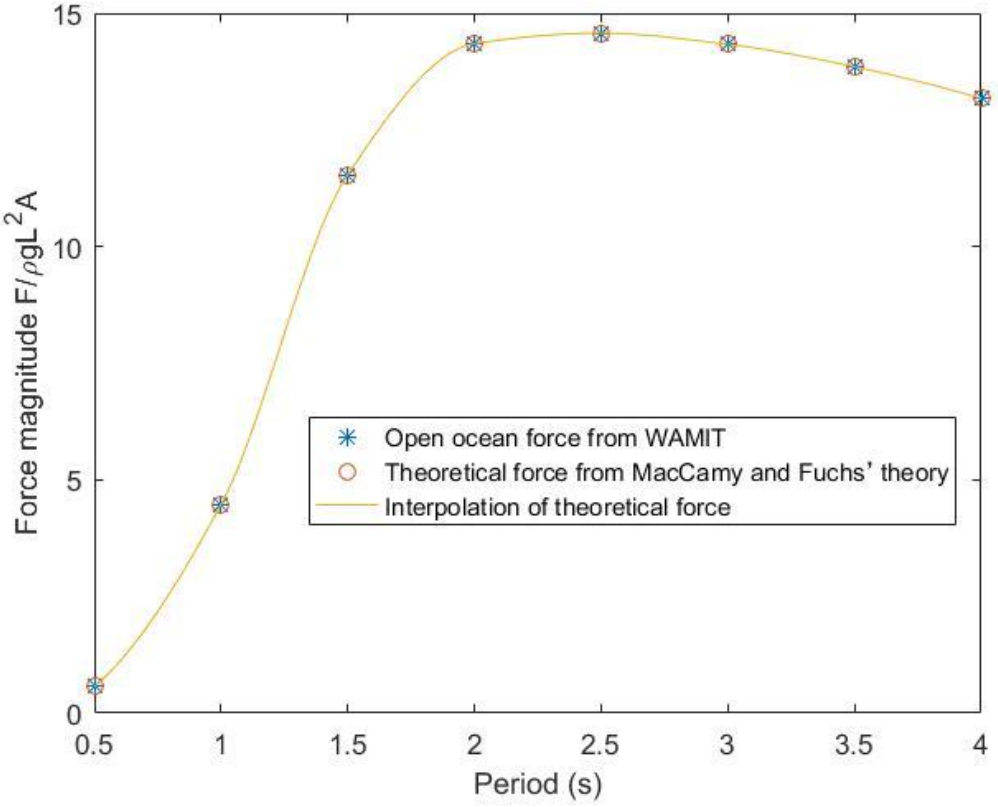

Figure 51 Comparison of magnitude of surge force transfer function for open ocean case

The exciting force calculated by the method of images is studied. Since the result is generated by twenty-four flaps, the factor of symmetry is considered. The exciting force is calibrated by the wave elevation at the center of the cylinder to achieve the force transfer function $|F|/(\rho g L^2|\eta|)$, where $|F|$ is the exciting force amplitude and

$|\eta|$ is the wave elevation amplitude without the presence of the cylinder body. The wave elevation amplitude $|\eta|$ is calculated from the previous wave elevation analysis using the method of images. Since there is no field point on the exact center of the cylinder, the wave elevation is represented by the average wave elevation of the four closest field points around the center.

Figure 52 shows the calibrated surge force transfer function and the theoretical result. There is a difference in the calibrated surge force transfer function for the cylinder in the wave basin, as calculated by the method of images, compared to the theoretical result for the open ocean. Considering the calibration is based on the average wave elevation, which may not represent the actual elevation precisely, considering the small loss of precision in applying the method of images using Matlab, and considering the real effect of the side wall reflections, the WAMIT result using the method of images is reasonable. Moreover, the error for periods larger than 1s is less than 5%, as shown in Table 5.

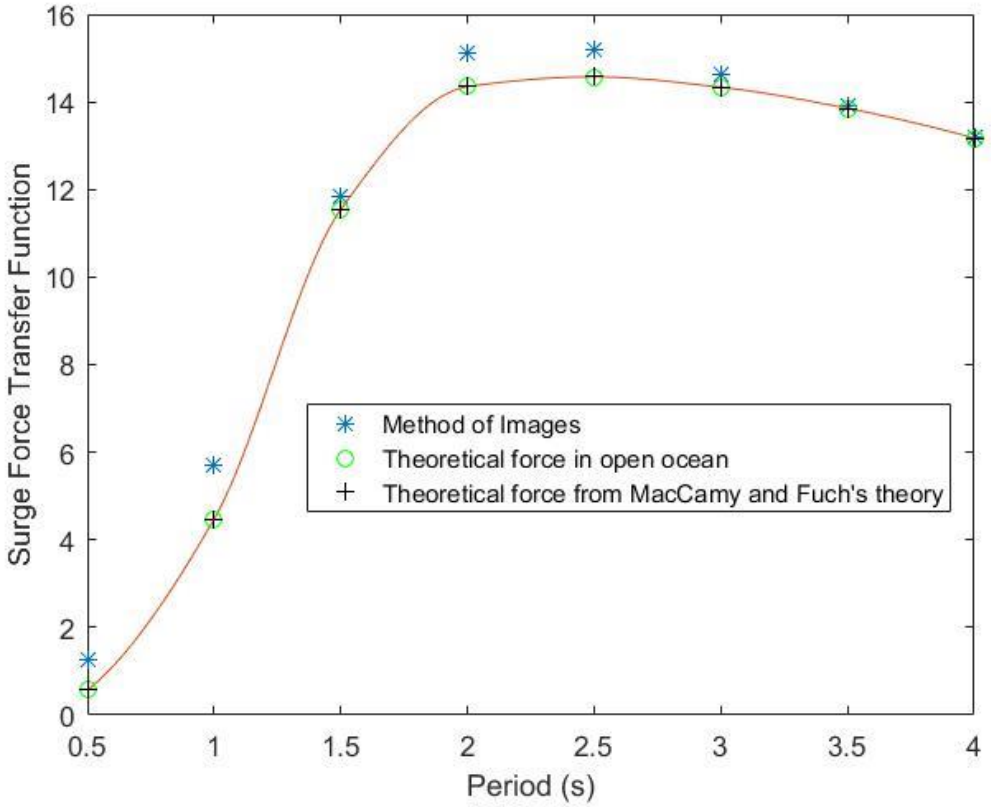

Figure 52 Comparison of magnitude of surge force transfer function: cylinder in wave basin (method of images) and theoretical result for cylinder in open ocean

Table 5 Difference of surge force transfer function between method of images for wave basin and theoretical calculation for open ocean case

Period/s	Theoretical calculation	Method of images	Magnitude of difference	Percent difference
0.5	0.5652	1.2606	0.6953	123%
1	4.4700	5.7056	1.2356	27.64%
1.5	11.5397	11.8226	0.2828	2.45%
2	14.3465	15.1227	0.7763	5.41%
2.5	14.5726	15.1879	0.6153	4.22%
3	14.3338	14.6257	0.2920	2.04%
3.5	13.8519	13.8978	0.0459	0.33%
4	13.1761	13.1931	0.017	0.13%

Figure 53 shows the phase shift of the surge force transfer function, where the theoretical phase shift is calculated by

$$\alpha = \tan^{-1}\left\{\frac{Y_1'(ka)}{J_1'(ka)}\right\}$$

where Y_1' is the derivative of the first order of second kind Bessel function and J_1' is the derivative of the first order of first kind Bessel function. k is the wave number and a is the radius of the cylinder, as introduced in Section 2.1.

Considering the phase of the WAMIT result is referenced to the center of the wavemakers, a phase shift of $k \Delta x$ is applied, where k is the wave number and Δx is the distance from the center of cylinder to the plane of the wavemakers. In this case, Δx =

53.5’. After applying this phase shift, the results calculated by the method of images and the theoretical results are very close. The difference may be due to the considerations noted above for the amplitude of the transfer function.

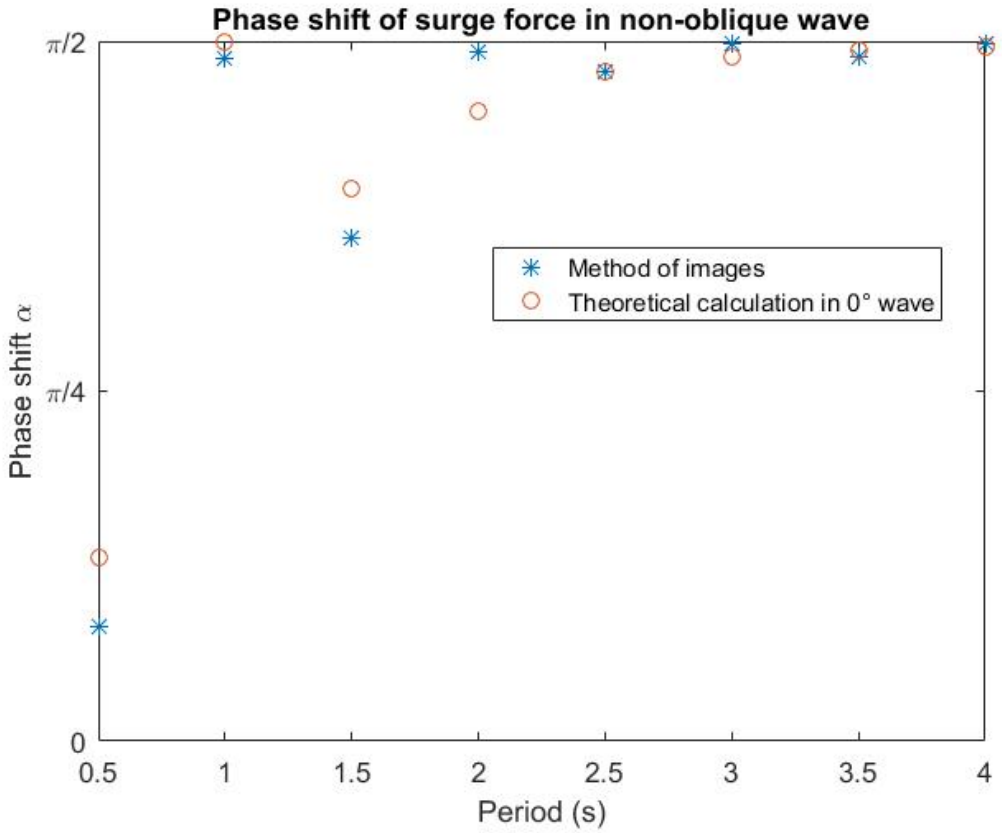

Figure 53 Phase shift of surge force

The sway force contribution from flaps in the positive y-axis is different in sign from that in the negative y-axis. Because of the symmetry about the centerline of the wave tank, the sway force is zero in the 0° wave. The contribution from wavemaker flaps on the positive y-axis cancels out that from flaps on the negative y-axis.

5.6 Exciting Force on a Bottom-founded Cylinder in Oblique Waves

The algorithm to post-process the exciting force due to oblique waves is similar to that for generating the oblique waves. To generate an oblique wave field, the motion of the wavemaker flaps is based on the snake principle. Similarly, there is a phase shift on each finite width wavemaker flap. The phase shift of the wavemaker flap is then passed on to the exciting force on the circular cylinder. Note that in this case, the plane of symmetry is applied. The database only contains the data for twenty-four wavemaker flaps and we are supposed to generate the influence for the entire wave basin containing 48 wavemaker flaps. We can realize this by referring to the twenty-four wavemaker flaps database through corresponding mirrored indices. Given a wavemaker flap, we will only need to calculate the y-coordinate for the flap (either the coordinate of the flap among the twenty-four flaps or the corresponding mirrored flap) and the phase shift will be simply $k_0 \cdot y$. We can then apply different phase shifts of $k_0 \cdot y$ to each exciting force component from a wavemaker flap of the 48 flaps.

We denote the wavemaker flap index as q, where the range of q is from $-N_f/2$ to $N_f/2$ excluding 0. Thus the set of q contains indices for $N_f = 48$ wavemaker flaps. The negative values of q correspond to the mirrored wavemaker flaps on the negative y-axis. The y-coordinate of the wavemaker flaps y including mirrored ones can be determined through

$$y = \frac{\frac{2}{N_f+1}}{2} * \frac{q}{|q|} + \frac{D-2}{N_f} * q + \frac{2}{N_f+1} * (|q|-1) * \frac{q}{|q|} - (D-2)/N_f/2 * \frac{q}{|q|}$$

where $\frac{q}{|q|}$ denotes the sign of q, and D is the width of the wave tank.

The amplitude of the exciting force can be calculated. In the case of oblique wave, the exciting force can be expressed in the form

$$W\,cos(\omega t + \delta - \ k_0 \cdot y)$$

Note that the real component of exciting force is $Re = W\cos(\delta)$ and the imaginary component is $Im = W\sin(\delta)$. The result can be expressed in the form

$$\begin{aligned} &W\cos(\omega t + \delta - \ k_0 \cdot \mathrm{y}) \\ &\quad = (W\cos(\delta)\cos k_0\mathrm{y} + W\sin(\delta)\sin k_0\mathrm{y})\cos\omega t \\ &\quad + (W\cos(\delta)\sin k_0\mathrm{y} - W\sin(\delta)\cos k_0\mathrm{y})\sin\omega t \\ &\quad = (Re\cos k_0\mathrm{y} + Im\sin k_0\mathrm{y})\cos\omega t + (Re\sin k_0\mathrm{y} - Im\cos k_0\mathrm{y})\sin\omega t \end{aligned}$$

The amplitude can then be calculated as

$$\sqrt{(Re\cos k_0\mathrm{y} + Im\sin k_0\mathrm{y})^2 + (Re\sin k_0\mathrm{y} - Im\cos k_0\mathrm{y})^2}$$

Note that the phase shift for each wavemaker flap is different. So the total amplitude is a summation of all real and imaginary components with phase shift applied.

$$\sqrt{\left(\sum_i^{N_f}(Re\cos k_0 y_i + Im\sin k_0 y_i)\right)^2 + \left(\sum_i^{N_f}(Re\sin k_0 y_i - Im\cos k_0 y_i)\right)^2}$$

where N_f is the number of wavemaker flaps.

The sway force contribution from flaps in the positive y-axis is different in sign from that in the negative y-axis, as previously discussed in Section 5.5. However, in the oblique wave case, the phase shifts on mirrored flaps are different, based on the snake principle. The contribution from wavemaker flaps on the positive y-axis can no longer

cancel out that from flaps on the negative y-axis. The sway force is not zero in magnitude.

The open ocean oblique wave cases are run in WAMIT and used for comparison. The surge and sway force transfer functions can be calculated by the components of the surge force transfer function in the non-oblique case. Denoting the magnitude of the surge force in non-oblique waves as F, for a given oblique wave with wave angle θ, the magnitude of the surge force for this wave angle is $F\cos\theta$. Similarly, the magnitude of the sway force for this wave angle is $F\sin\theta$. The phase shifts of the surge and sway forces are equal, which are the same with the theoretical calculation by MacCamy and Fuchs' theory, after applying the phase shift $k \Delta x \cos\theta$ from the origin of the global coordinate to the center of the cylinder, as shown in Figure 54. The force transfer functions in the open ocean cases are as shown in Figure 55 and Figure 56.

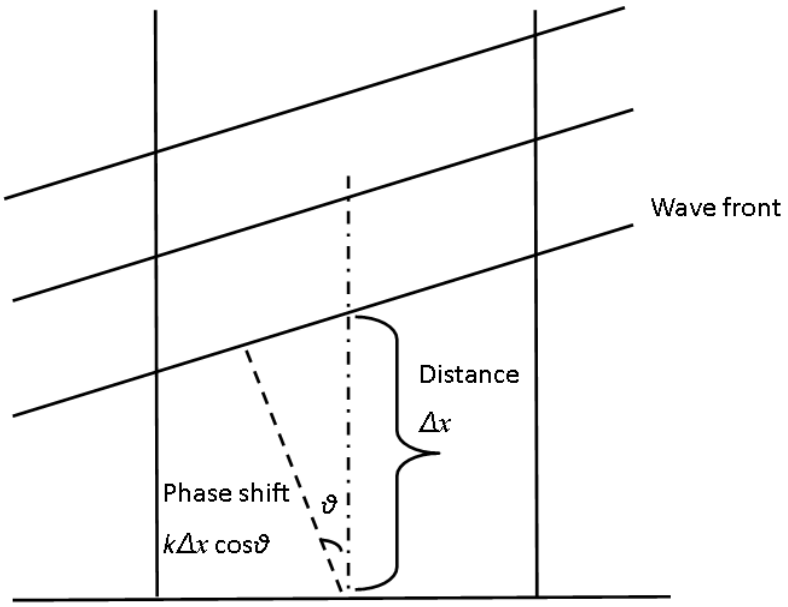

Figure 54 Illustration of phase shift in oblique wave

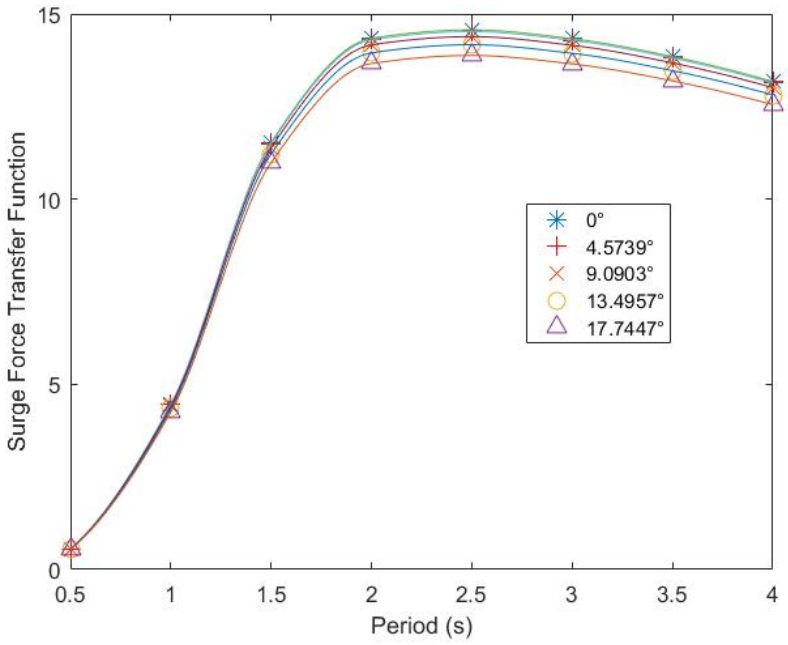

Figure 55 Magnitude of surge force transfer function in open ocean

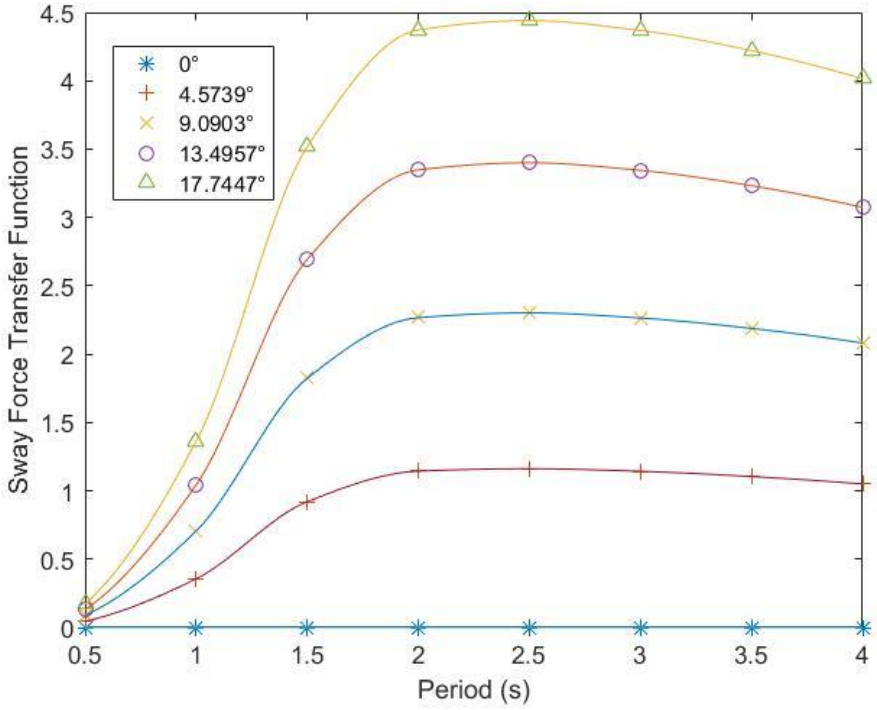

Figure 56 Magnitude of sway force transfer function in open ocean

We first analyze the 0° special case in oblique wave analysis. Figure 57 shows the surge force for 0° wave and Figure 58 shows the sway force for 0° wave. Notice that the sway force transfer function is at the level of 10^{-15}, which is consistent with the previous result in Section 5.5 where the sway force is zero.

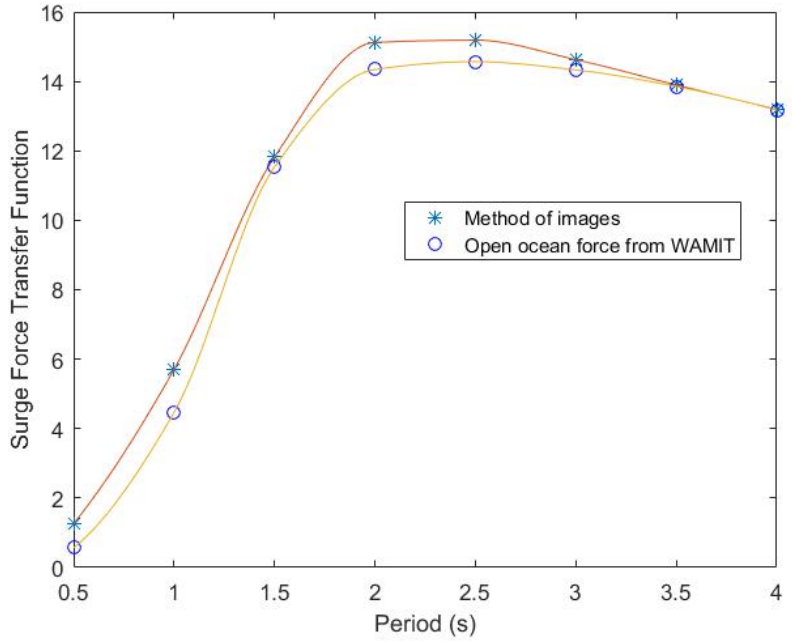

Figure 57 Magnitude of surge force transfer function for 0° wave

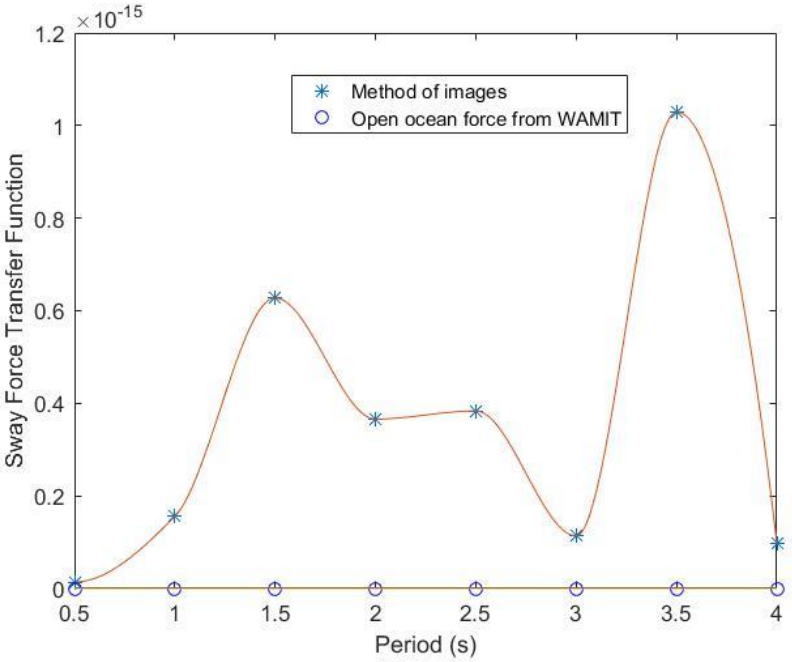

Figure 58 Magnitude of sway force transfer function for 0° wave

Since the wave amplitude is calculated by different methods in the oblique wave case and the non-oblique wave case, a comparison of the surge force transfer function obtained using the two methods is presented in Figure 59. With the non-oblique wave method, the wave amplitude is calculated from the $\eta_s(x_0, y_0)$ matrix, which is a summation of elevation from all wavemakers. While in the oblique wave method, 0° is just a special case of the oblique wave angle. The result shows that the different methods yield exactly the same result for the amplitude of the surge force transfer function, which to some extent validates the method of images in exciting force analysis.

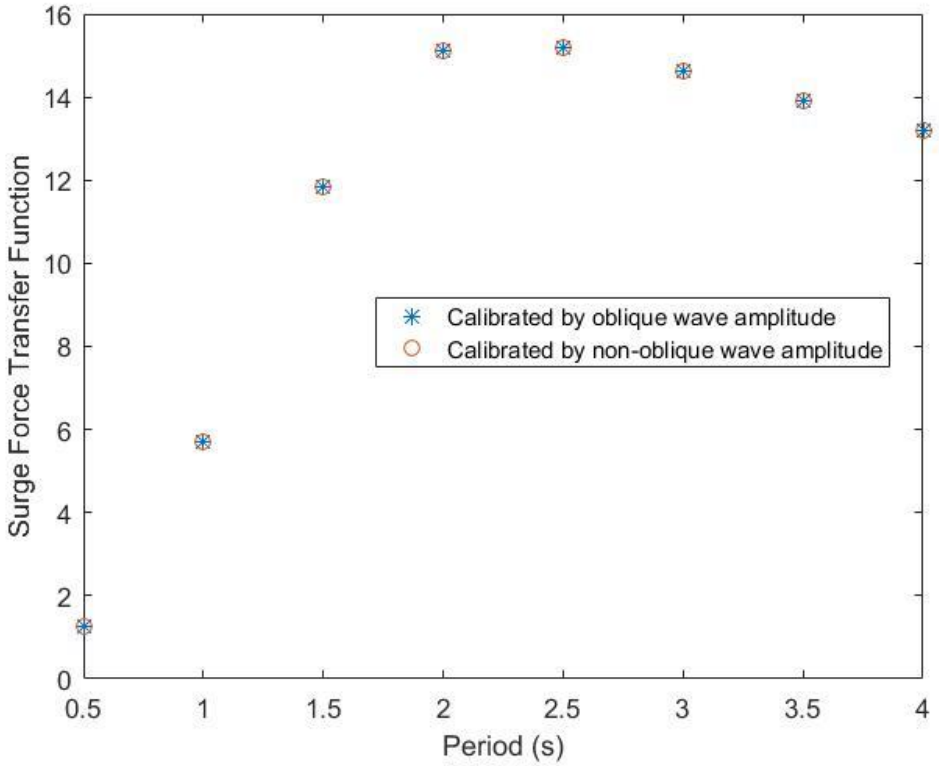

Figure 59 Magnitude of surge force transfer function based on different methods of wave calibration for 0° waves

As we increase the wave angle, the surge force changes slightly and the sway force becomes noticeable. The results are shown below in Figure 60 and Figure 61. Note that the change of the surge force amplitude is noticeable for different wave angles, but since the wave elevation amplitude is different for different wave angles, as shown in Figure 62, the resulting force transfer function after calibration does not change as much. The sway force transfer function changes greatly as related with $sin\theta$.

The phase shift of the surge and sway force transfer functions in oblique waves are shown in Figure 63 and Figure 64 respectively.

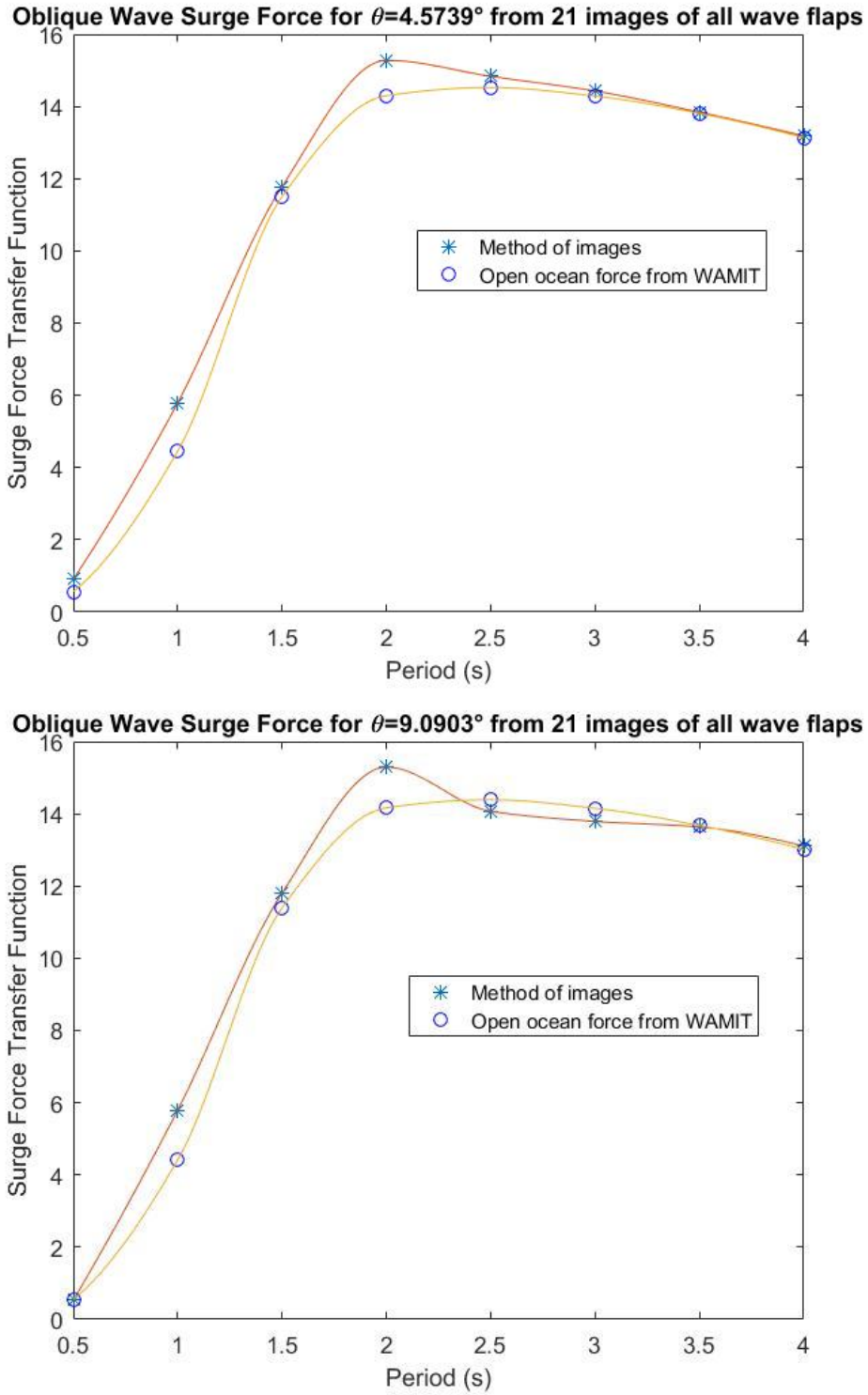

Figure 60 Magnitude of surge force transfer function for oblique waves

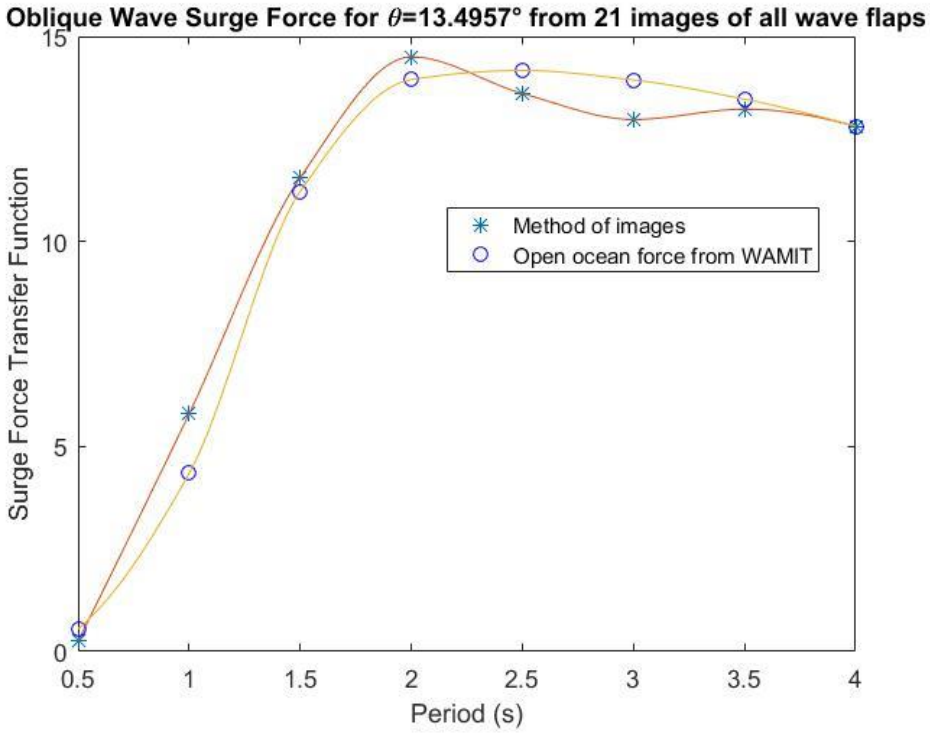

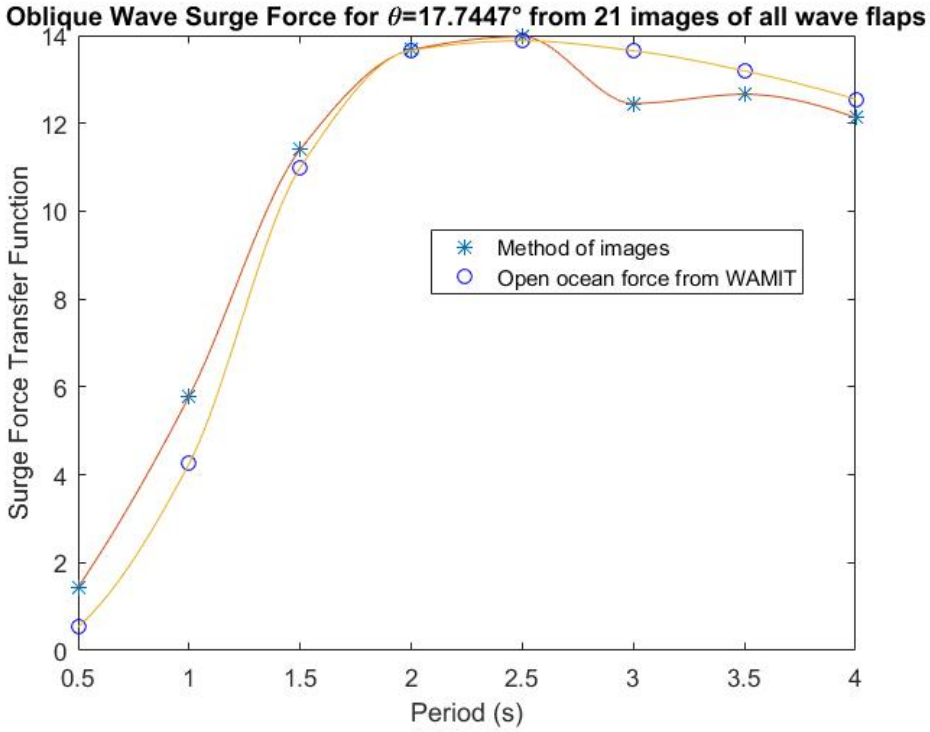

Figure 60 Continued

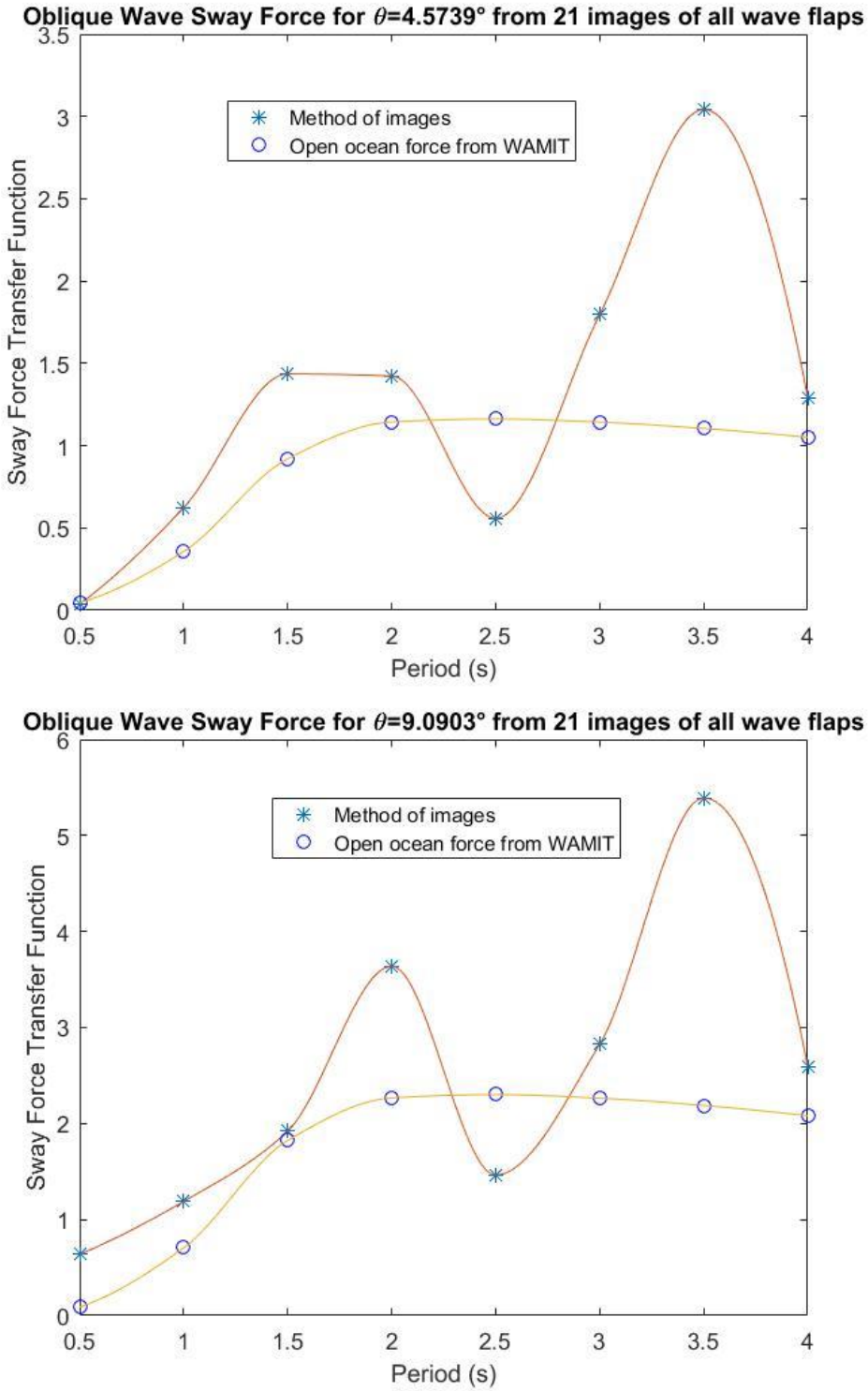

Figure 61 Magnitude of sway force transfer function for oblique waves

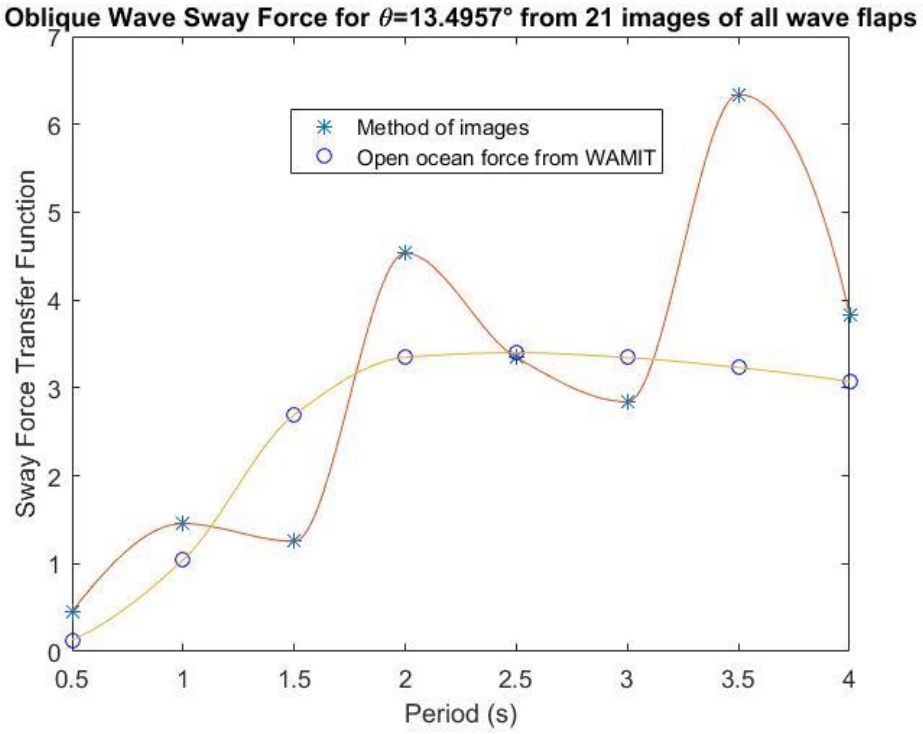

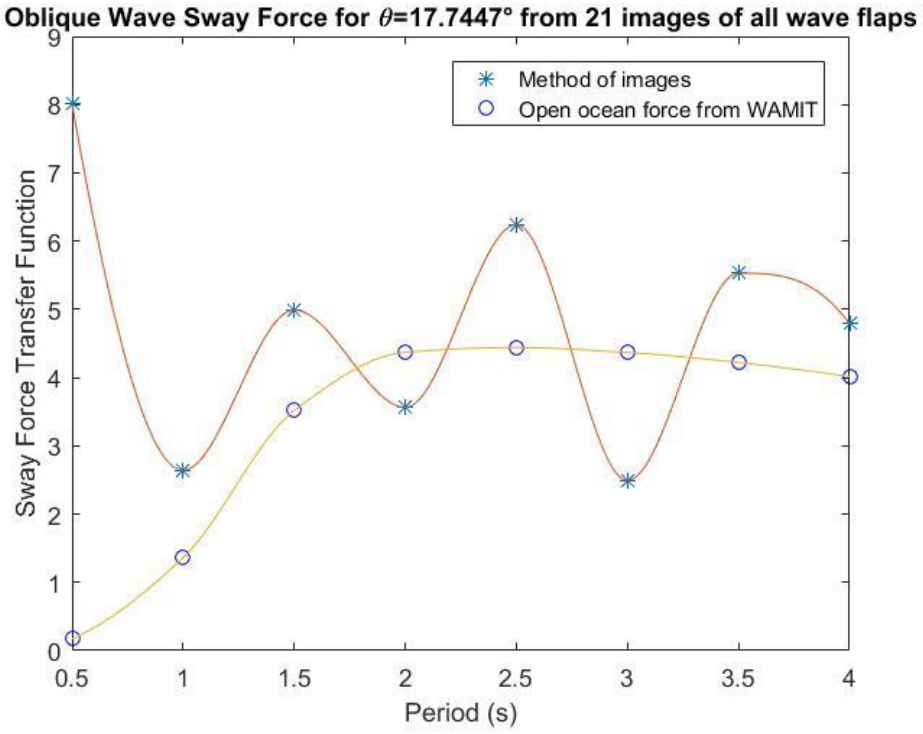

Figure 61 Continued

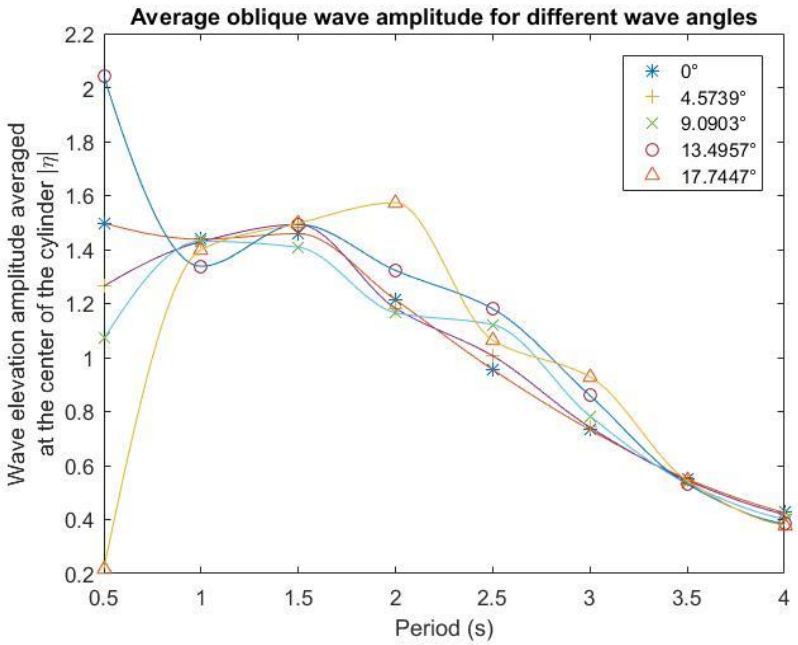

Figure 62 Average oblique wave amplitude for different wave angles

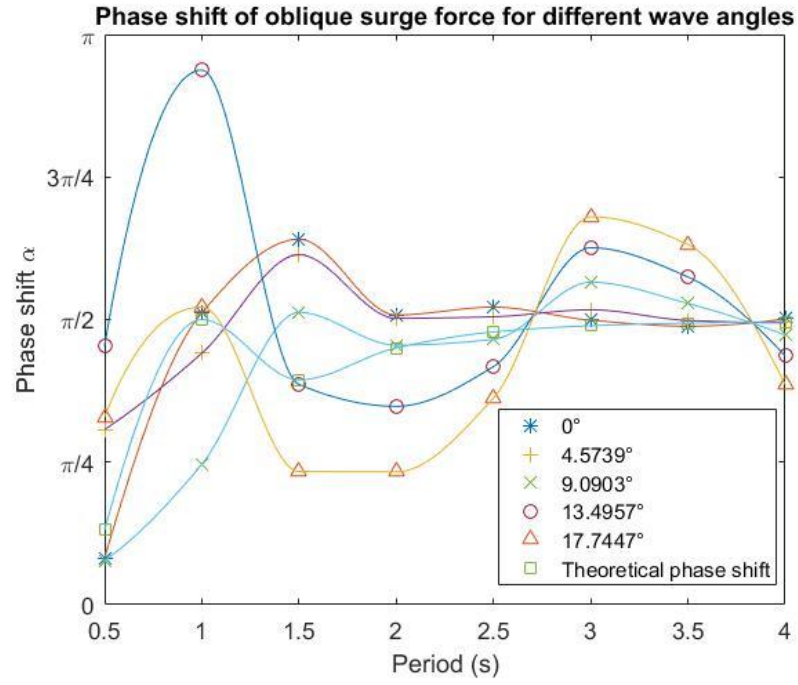

Figure 63 Phase shift of surge force transfer function for oblique waves

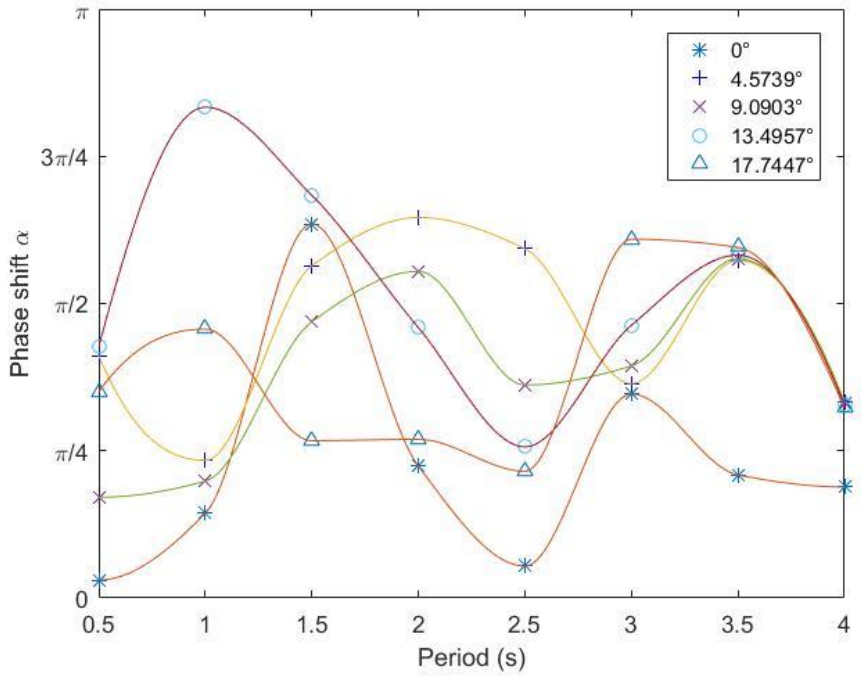

Figure 64 Phase shift of sway force transfer function for oblique waves

From the plots, it is shown that the surge force transfer function is in good agreement with the open ocean case. The sway force transfer function is more inconsistent with the open ocean case. However, it is still at a comparable level of magnitude with the open ocean result.

Ideally, the wave amplitude at the center of the cylinder should be the same in the oblique wave case compared to the non-oblique wave case. However, due to the side wall effects in the oblique wave case and the fact that the wave amplitude is calculated by the average wave elevation of the four closest points, there is a noticeable difference in the wave amplitude, especially for large wave angles. The variation of surge and sway force transfer functions in oblique waves may be due to this nonuniformity of wave

amplitude. As mentioned earlier, the uniformity of wave amplitude in the test area is degraded for large wave angles. The sway force may be more influenced by the nonuniformity and other source of loss of precision in that the magnitude of sway force transfer function is relatively small.

In addition, the convergence test was not performed for the exciting force analysis due to the limited time. Only one case of 20 cylinder images was run in WAMIT. Comparing to the number of images we used in wave elevation generation, this may not be enough to generate accurate results, particularly in the oblique wave case. The convergence test in wave field generation shows that about 40 images will provide a convergence level of 2%, which is actually 80 image flaps. With 20 cylinder images in this case, even though the scale of the cylinder is very small compared to the size of the tank, the loss of precision in the convergence will still have an accumulated effect on the analysis of forces.

A method of accelerated series of image Green functions for solving problems of bodies in a finite width channel is included in an updated version of WAMIT. The results of surge and sway force transfer functions generated from this 'channel-width' method are compared with our method of images. Figure 65 shows the comparison of surge force transfer function for non-oblique wave. Figure 66 to Figure 69 show the comparisons of surge and sway force transfer functions for oblique wave. The results from these two methods are in good agreement. Note that for the oblique wave case attempts to obtain converged WAMIT solutions using the 'channel-width' option at 0.5s and 1.0s periods were not successful, hence the omitted points on the plots.

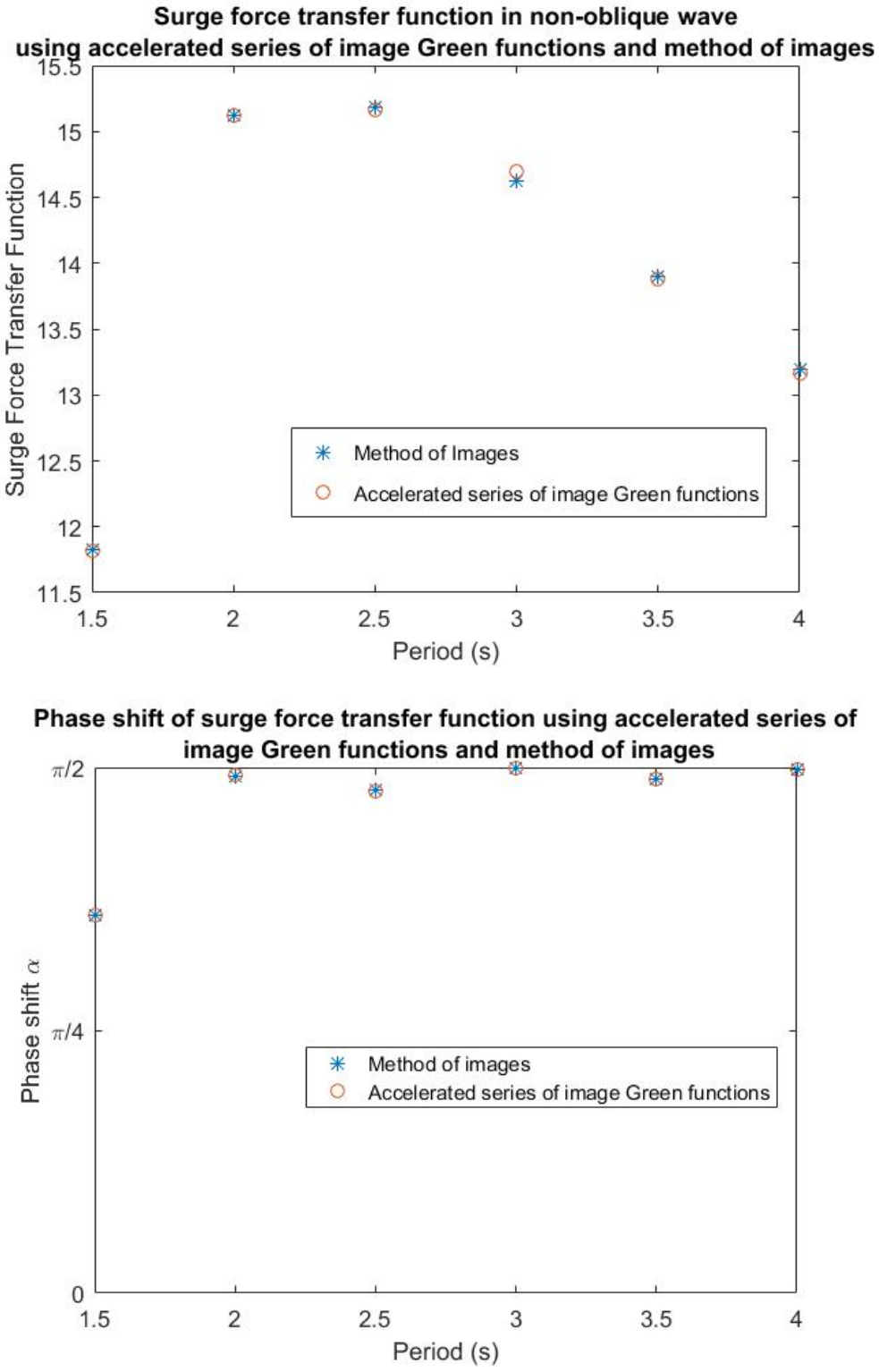

Figure 65 Comparison of surge force transfer function for non-oblique wave

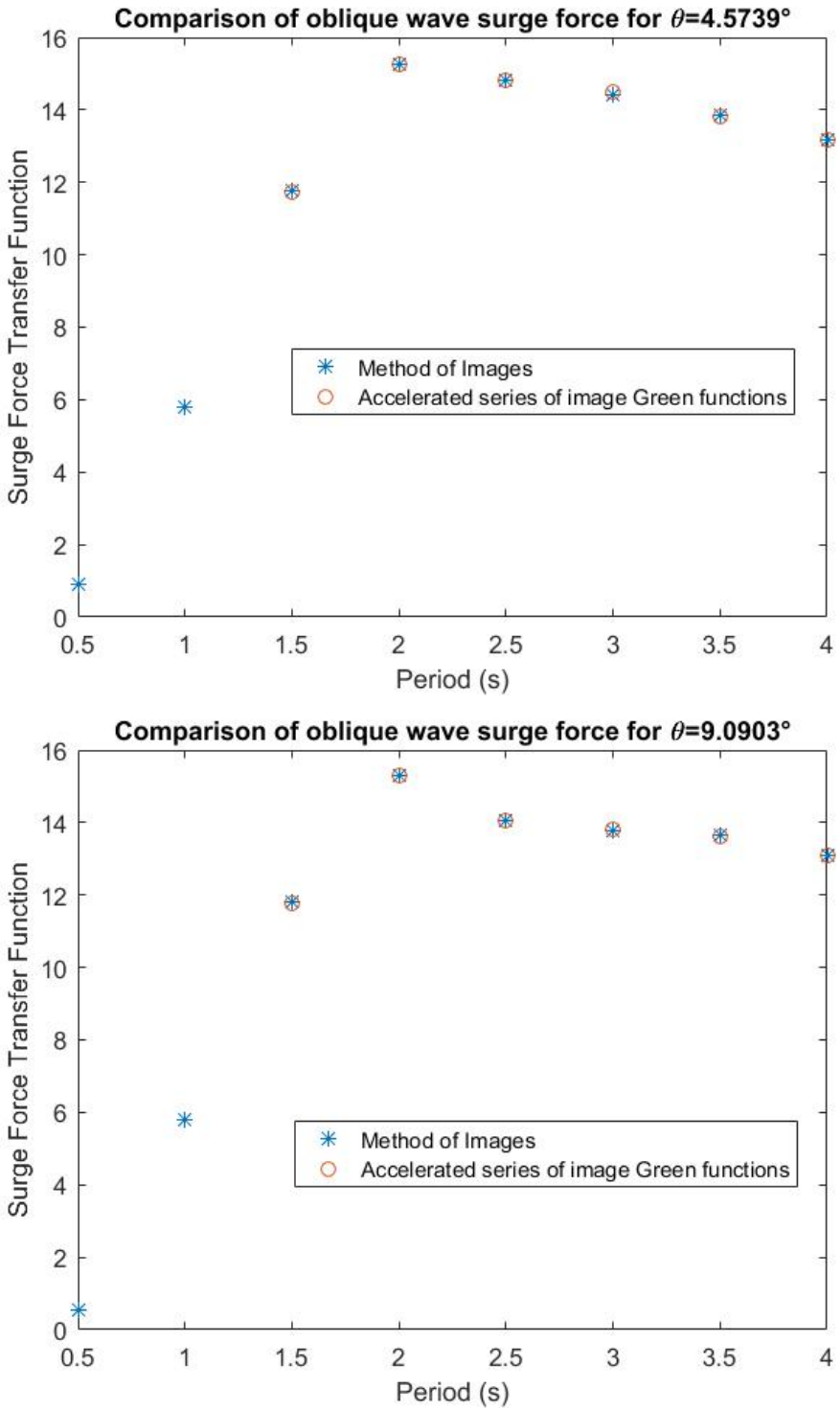

Figure 66 Comparison of surge force transfer function magnitude for oblique wave

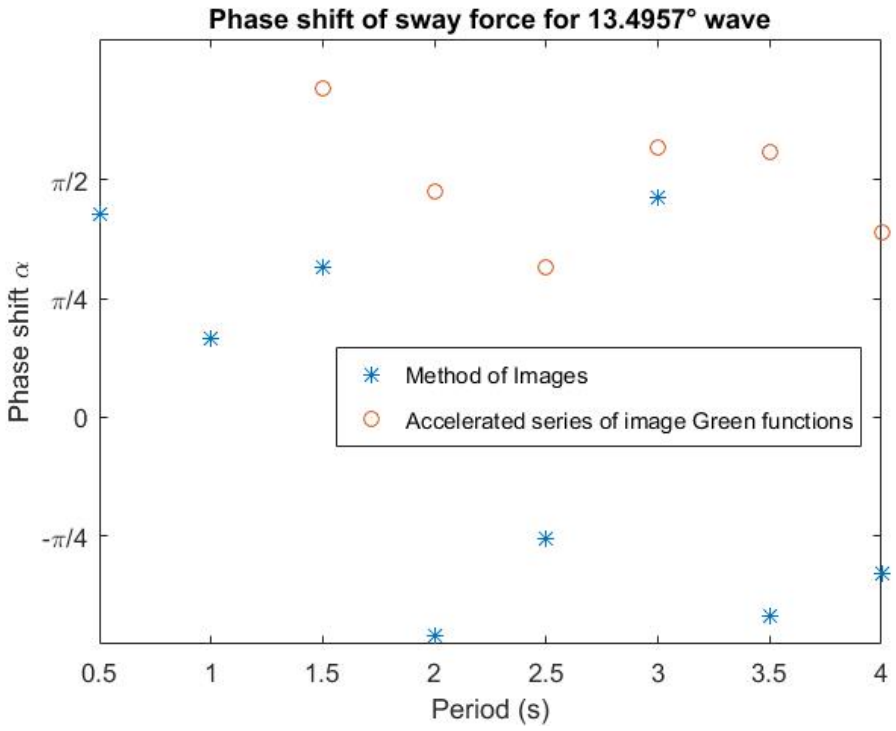

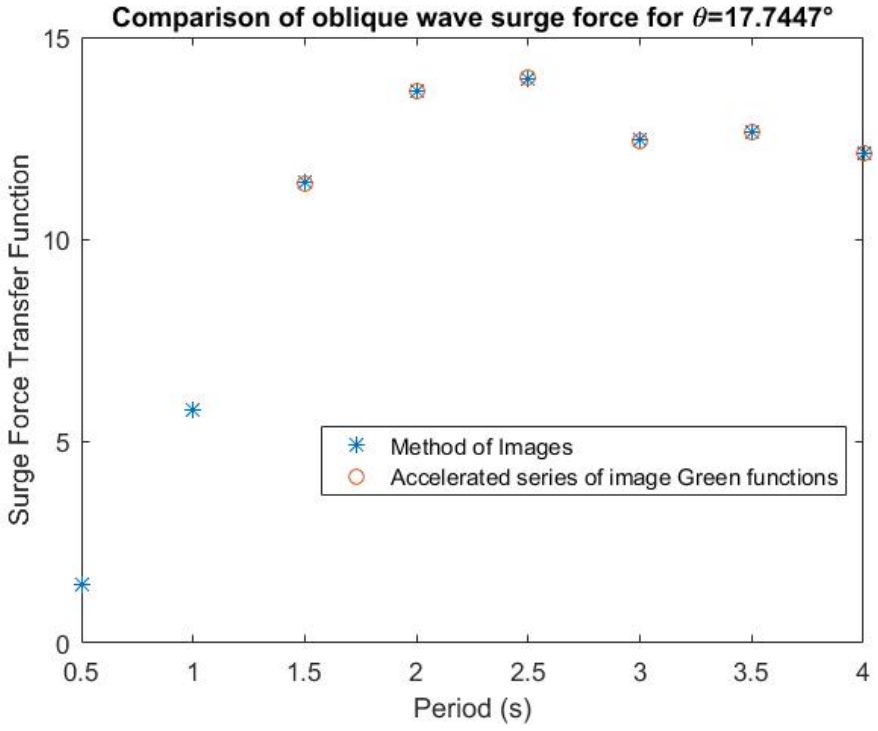

Figure 66 Continued

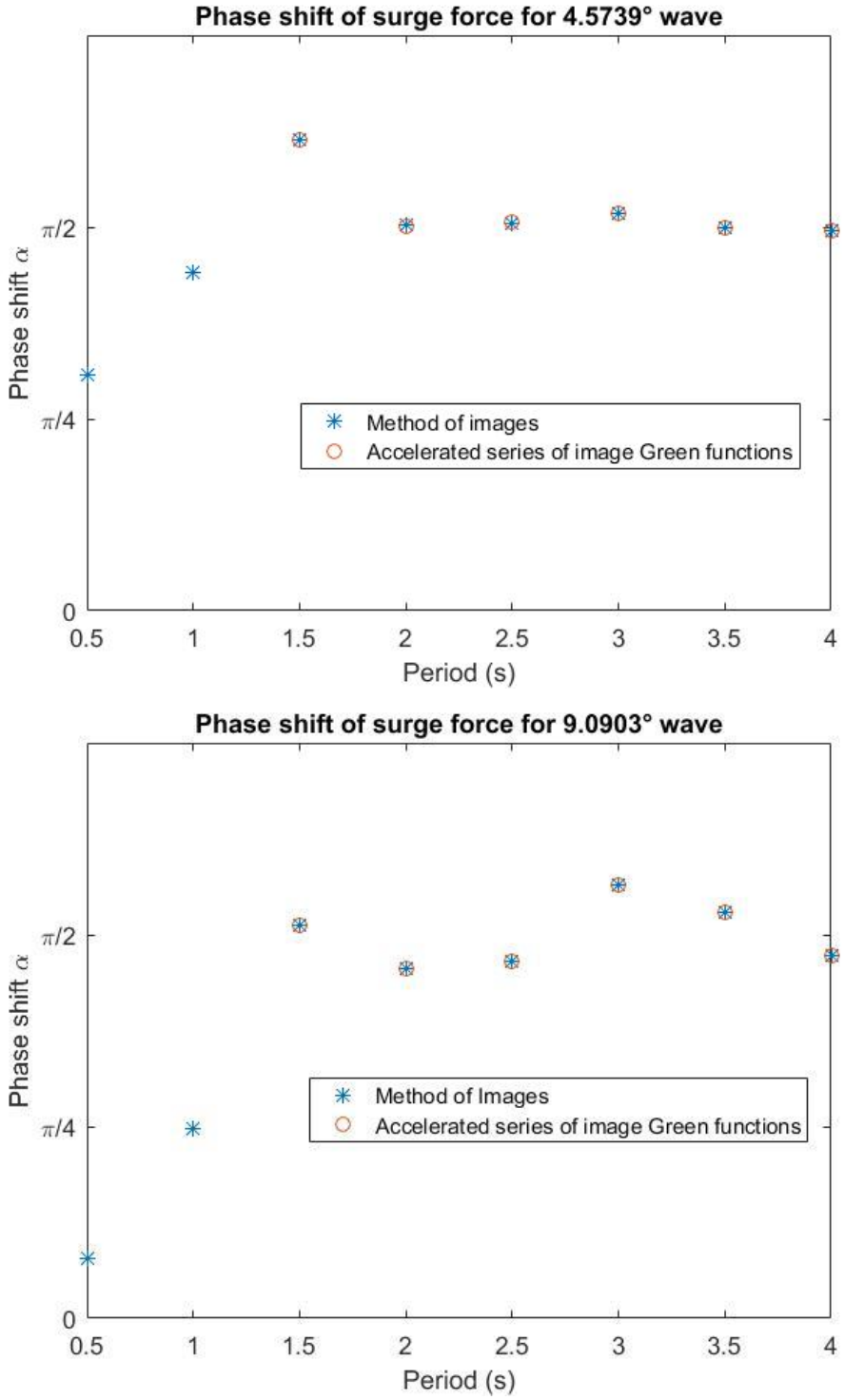

Figure 67 Comparison of phase shift of surge force transfer function for oblique wave

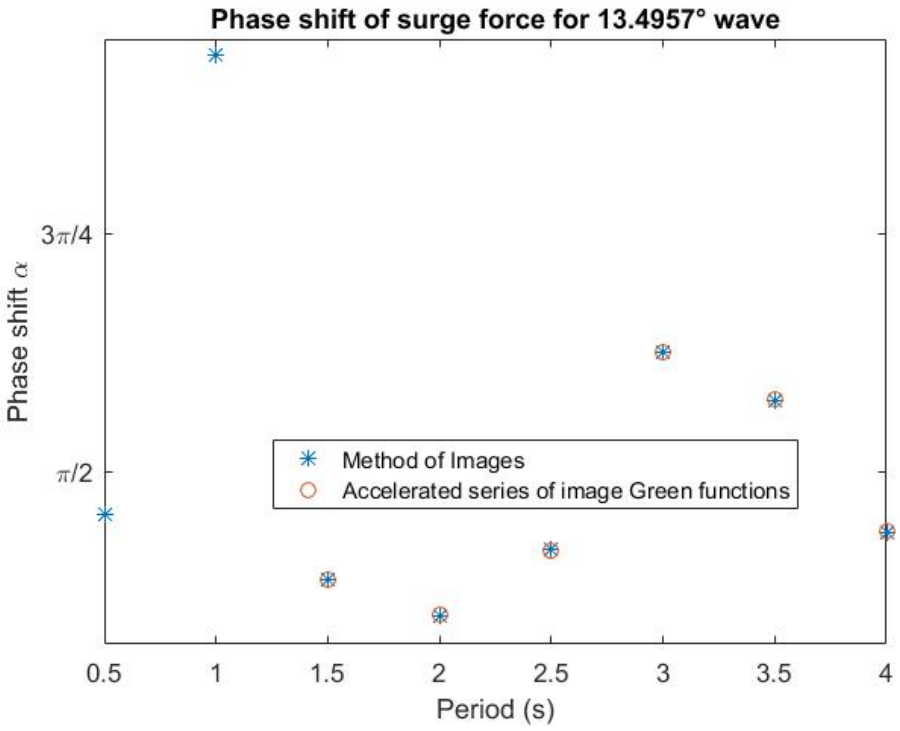

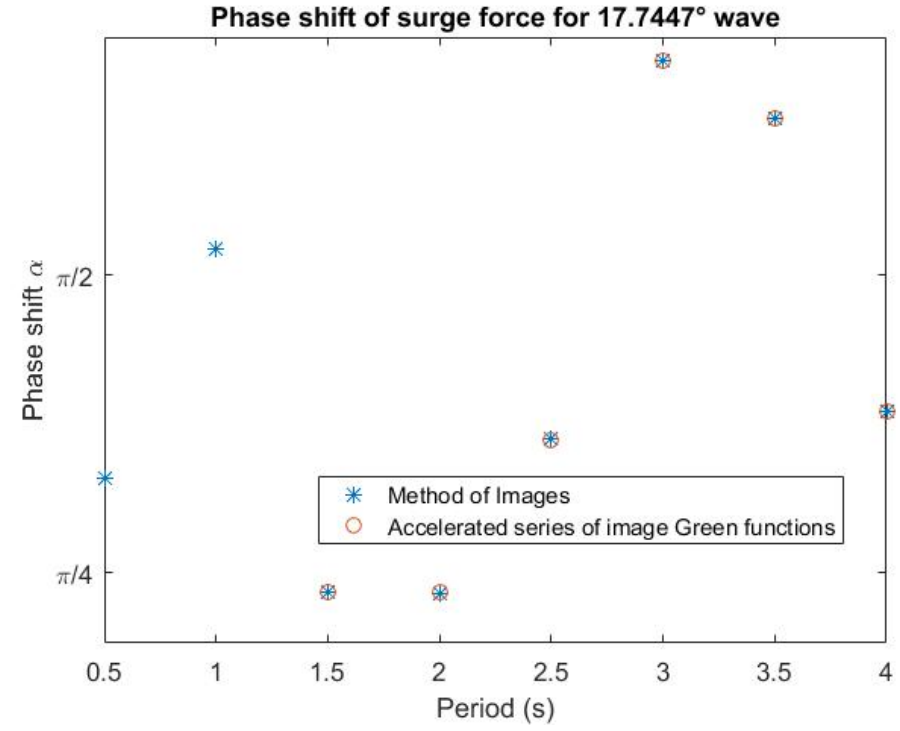

Figure 67 Continued

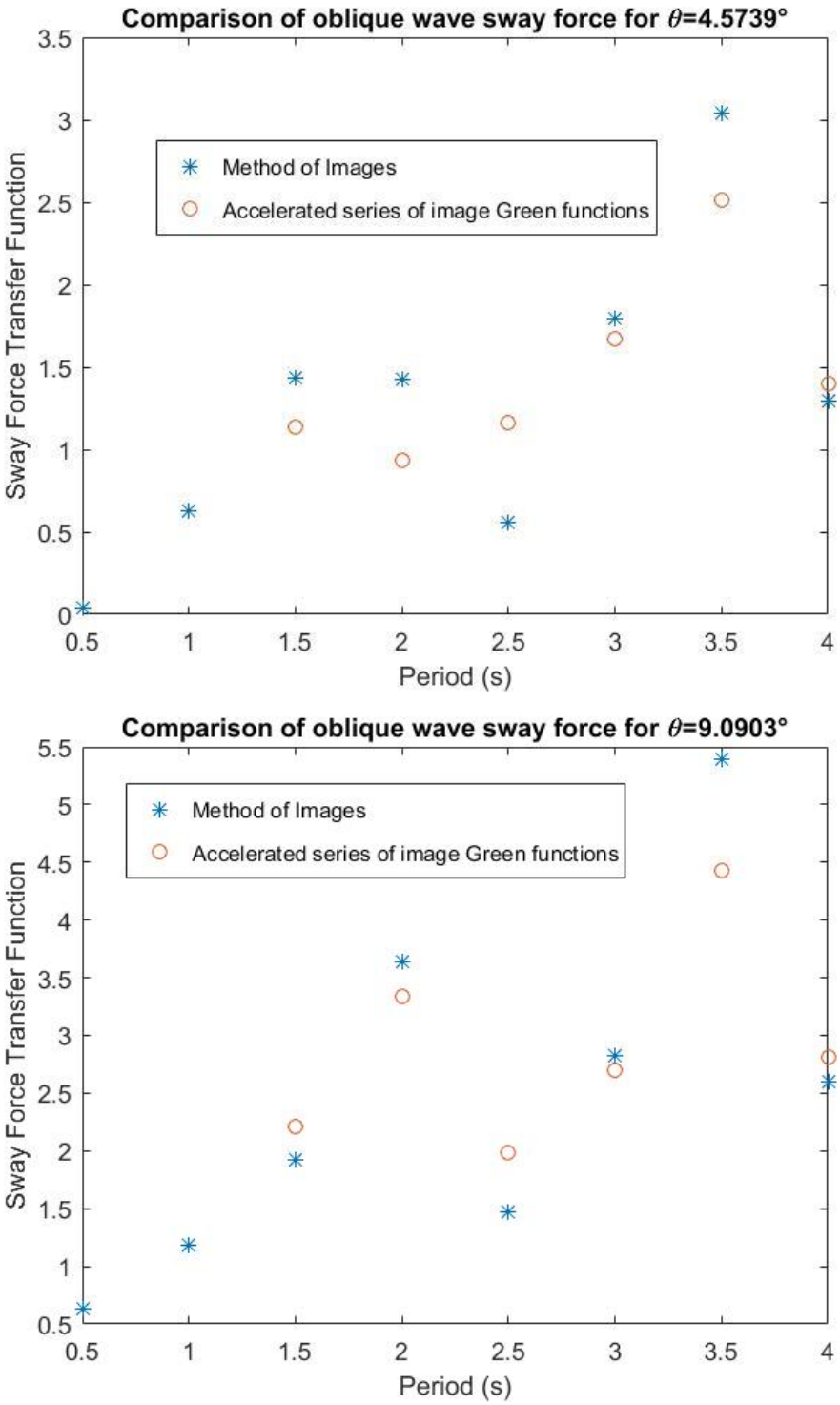

Figure 68 Comparison of sway force transfer function magnitude for oblique wave

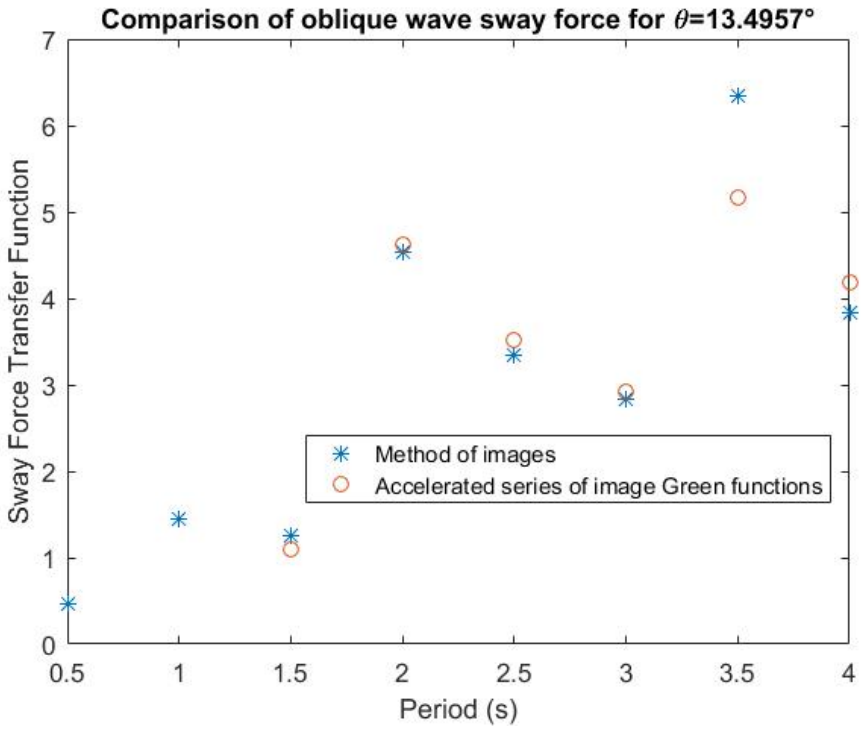

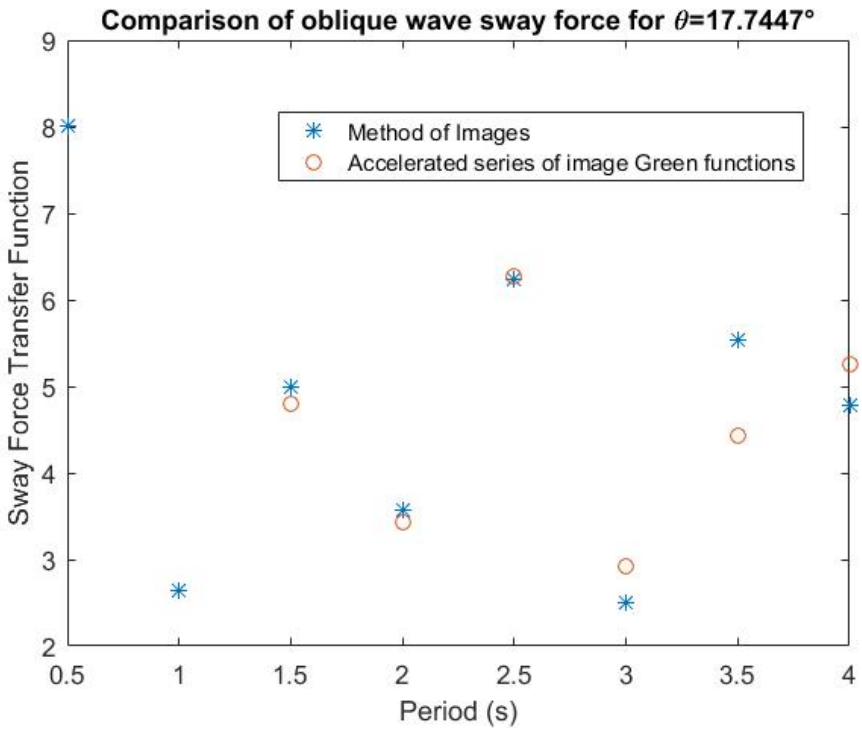

Figure 68 Continued

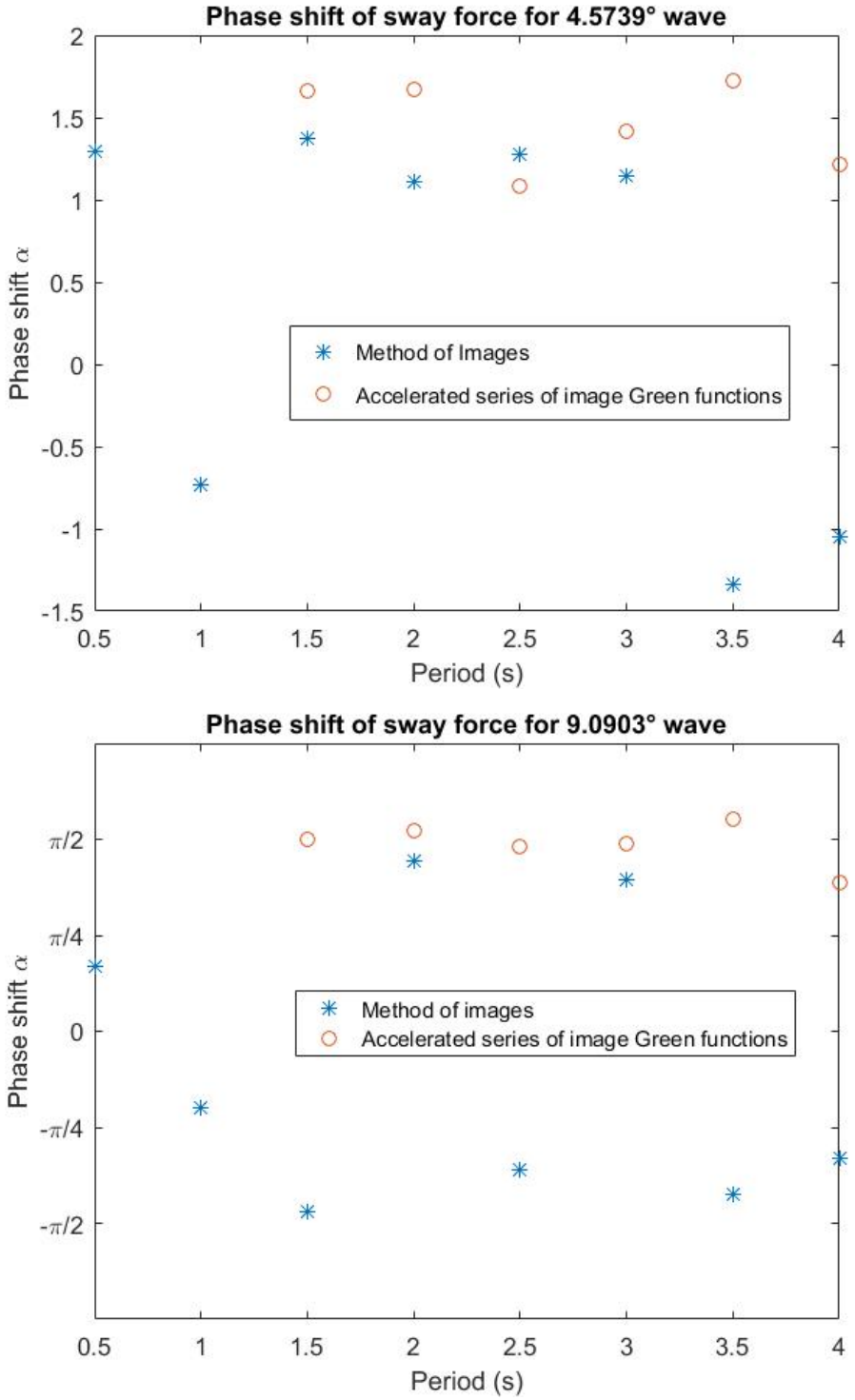

Figure 69 Comparison of phase shift of sway force transfer function for oblique wave

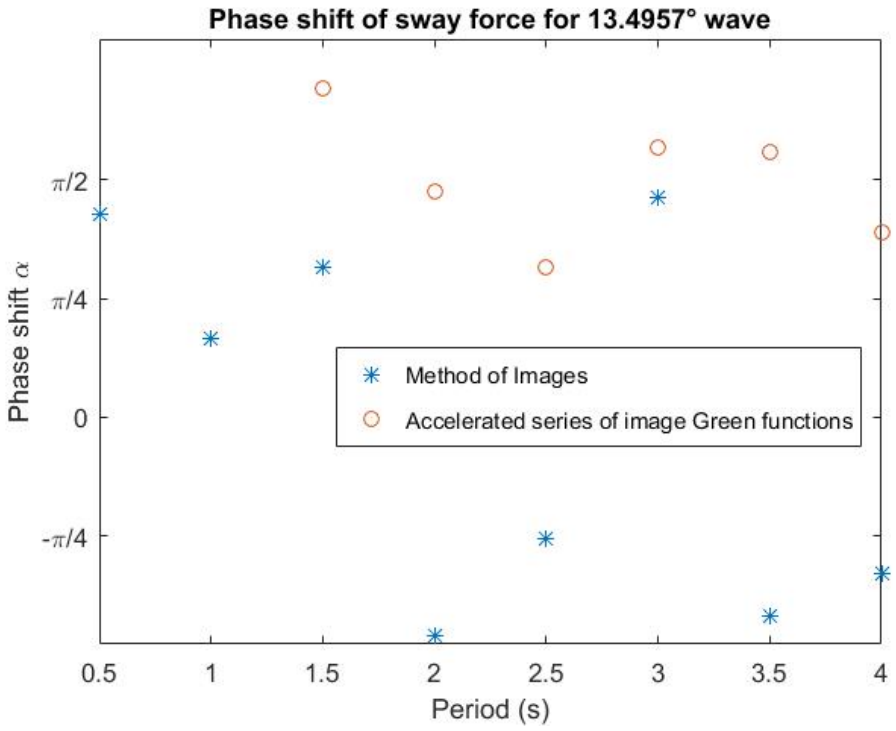

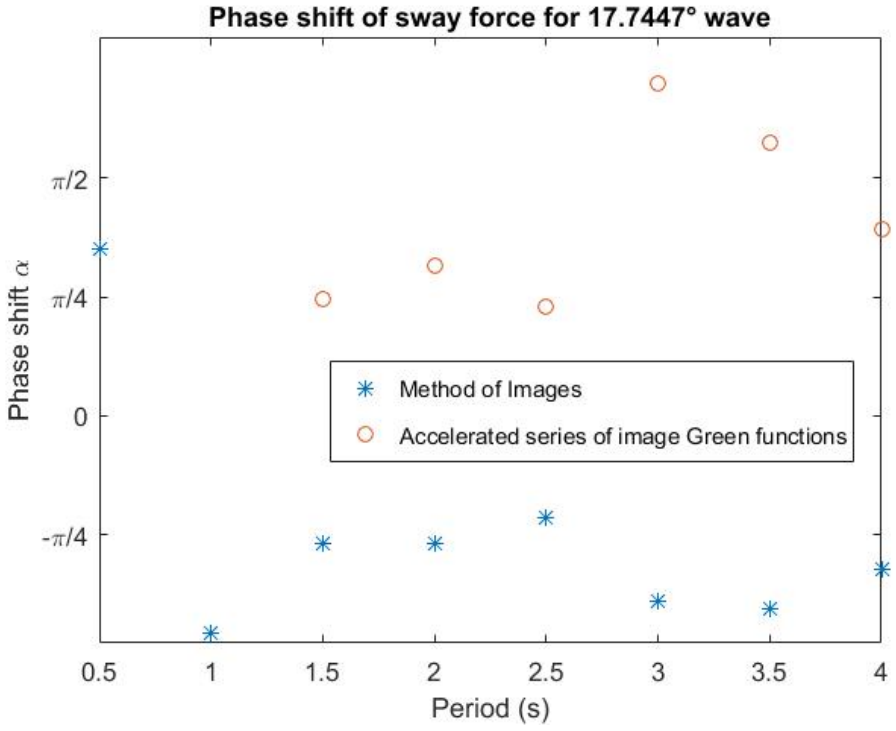

Figure 69 Continued

CHAPTER VI

SUMMARY AND CONCLUSION

This thesis aims to develop a 3D numerical model of the OTRC wave basin based on linear hydrodynamics. The method of direct side wall modeling and the method of images were studied in developing the numerical model using WAMIT. The numerical results in the study of free-surface wave elevation and the first order exciting force were compared with theoretical calculations. The method of direct side wall modeling was studied but was not selected for building the numerical model because of non-correctable numerical issues with the WAMIT solutions. The method of images was determined to provide adequate accuracy in modeling the wave basin to an extent governed by the number of images incorporated in the simulation, as validated by the simulations of wave generation and of exciting forces on a model in the test area.

The numerical model of the OTRC wave basin is assembled with images of wavemaker flaps and images of model bodies using the method of images. The side wall reflection effect is represented by a finite number of images to a certain accuracy. The following studies were performed in the conduct of this research.

First, a convergence test in the calculation of the wave field was performed using the method of images. The wave elevation from a considerable number of images (1600) shows good convergence to a reasonable accuracy (0.5%). The cross-tank wave elevation variation increases with wave period but is below 4% for periods less than 4s.

However, the time to evaluate the Green function in WAMIT for all the field points and to parse the database for post-processing is significant.

Second, the evanescent modes from the wavemaker for non-oblique wave generation were studied. The form of the evanescent modes identified from the simulations was consistent with theoretical expectations. The evanescent modes decay exponentially with the distance from the wavemaker and for periods less than 4s only affect the area within 25' of the wavemaker.

Third, the nonuniformity of the wave field associated with generation of oblique waves was investigated. Although in non-oblique wave generation the waves are long crested, in oblique wave generation the discrete finite width of wavemaker flaps and side wall reflection contribute to nonuniformity of the wave elevation in the basin. The nonuniformity in the test area is significant and, as expected, it increases with increasing wave angle. However, it is noted that the corner reflection technique developed by Funke and Miles (1987) to reduce the nonuniformity in the test area was not applied in this investigation, although it is routinely applied in the operation of the OTRC wave basin for oblique wave generation.

Fourth, the ability to calculate first order exciting forces on a bottom-founded circular cylinder in the test area using the method of images was demonstrated for both non-oblique and oblique waves. Theoretical calculations based on MacCamy and Fuchs' theory and numerical results from WAMIT for an open ocean case (no side walls or wavemaker) are used as benchmarks to assess the validity of the results obtained using the method of images, even though there should be small differences in the results for

the two cases. For non-oblique waves the amplitude and phase of the surge transfer function for the wave basin are in very good agreement with the open ocean results, confirming that the effect of the side walls is small. For oblique waves the difference between the (surge and sway) force transfer functions for the wave basin case compared to the open ocean case are noticeable. However, considering the nonuniformity of the wave amplitude, the side wall effects, and the loss of precision in applying the method of images using Matlab, the surge and sway force transfer functions appear reasonable as compared with the open ocean case results. The phase shift of the force transfer function can be greatly affected by the loss of precision and is not very consistent with the theoretical calculation. However, it is noted that a convergence test was not conducted for this case so the error in the results associated with using only 20 cylinder images in the simulation is unknown.

In conclusion, the use of WAMIT in combination with the method of images as an approach to model the linear hydrodynamics of the OTRC wave basin was successful. The model can be used to develop considerable insight on the extent to which "tank effects" can distort wave-body interactions in the wave basin as compared to the open ocean and to optimize the efficacy of different wavemaker control strategies. The tank effects investigated herein include evanescent modes from the wavemaker, sidewall wave reflections, and nonuniformity in oblique wave generation. Other tank effects that can and should be investigated in the future include effects of the pit, and reduction in nonuniformity associated with application of the Funke and Miles corner reflection method. Further, the performance of the wave basin in generation of irregular waves,

both long crested and directionally spread using single- and double-summation methods, should be studied. Methods to reduce the loss of precision and accelerate the convergence associated with application of the method of images should also be investigated, based on Newman (2016) and other references cited in his paper. In conjunction with this, the convergence analysis to determine the requisite number of image bodies to achieve a certain accuracy should be conducted. Finally, implementation of the basin model in the time domain using impulse response functions should be considered for efficient simulation of body responses in generated transient wave conditions.

REFERENCES

Boo, SY. "Linear and Nonlinear Irregular Waves and Forces in a Numerical Wave Tank." *Ocean Engineering* 29, no. 5 (2002): 475-93.

Boo, SY, CH Kim, and MH Kim. "A Numerical Wave Tank for Nonlinear Irregular Waves by 3-D Higher Order Boundary Element Method." *International Journal of Offshore and Polar Engineering* 4, no. 04 (1994): 265-272.

Chen, X. "On the Side Wall Effects Upon Bodies of Arbitrary Geometry in Wave Tanks." *Applied Ocean Research* 16, no. 6 (1994): 337-45.

Cointe, R. "Numerical Simulation of a Wave Channel." *Engineering Analysis with Boundary Elements* 7, no. 4 (12// 1990): 167-77.

Cooper, RIB and MS Longuet-Higgins. "An Experimental Study of the Pressure Variations in Standing Water Waves." *Proceedings of the Royal Society of London. Series A. Mathematical and Physical Sciences* 206, no. 1086 (1951): 424-435.

Dalrymple, RA. "Directional Wavemaker Theory with Sidewall Reflection." *Journal of Hydraulic Research* 27, no. 1 (1989): 23-34.

Funke, E and M Miles. "Multi-Directional Wave Generation with Corner Reflectors." *Institue for Mechanical Engineering Technical Report*, TR-HY-021, National Research Council, Canada (1987).

Grilli, ST, S Vogelmann, and P Watts. "Development of a 3d Numerical Wave Tank for Modeling Tsunami Generation by Underwater Landslides." *Engineering Analysis with Boundary Elements* 26, no. 4 (4// 2002): 301-13.

Haskind, MD and JN Newman. "The Exciting Forces and Wetting of Ships in Waves." DTIC Document, 1962: 65-79.

Havelock, TH. "Lix. Forced Surface-Waves on Water." *The London, Edinburgh, and Dublin Philosophical Magazine and Journal of Science* 8, no. 51 (1929): 569-76.

Kashiwagi, M. "Radiation and Diffraction Forces Acting on an Offshore-Structure Model in a Towing Tank." Paper presented at the The First ISOPE Pacific/Asia Offshore Mechanics Symposium, 1990: 95-102.

Kim, MH, JM Niedzwecki, JM Roesset, JC Park, SY Hong, and A Tavassoli. "Fully Nonlinear Multidirectional Waves by a 3-D Viscous Numerical Wave Tank." *Journal of Offshore Mechanics and Arctic Engineering* 123, no. 3 (2001): 124-33.

Koo, W. "Fully Nonlinear Wave-Body Interactions by a 2d Potential Numerical Wave Tank." Texas A&M University, 2004.

Lamb, H. *Hydrodynamics 6th Ed*. 1932.

Linton, CM. "A New Representation for the Free-Surface Channel Green's Function." *Applied Ocean Research* 21, no. 1 (2// 1999): 17-25.

Linton, CM. "The Green's Function for the Two-Dimensional Helmholtz Equation in Periodic Domains." *Journal of Engineering Mathematics* 33, no. 4 (1998): 377-401.

Longuet-Higgins, MS and ED Cokelet. "The Deformation of Steep Surface Waves on Water. I. A Numerical Method of Computation." *Proceedings of the Royal*

Society of London. A. Mathematical and Physical Sciences 350, no. 1660 (1976): 1-26.

Longuet-Higgins, MS and RW Stewart. "Radiation Stresses in Water Waves; a Physical Discussion, with Applications." Paper presented at the Deep Sea Research and Oceanographic Abstracts, 1964: 529-562.

MacCamy, RC and R Aam Fuchs. "Wave Forces on Piles: A Diffraction Theory." Corps of Engineers Washington DC Beach Erosion Board, No. TM-69 (1954).

Mansard, EPD, MD Miles, and RA Dalrymple. "Numerical Validation of Directional Wavemaker Theory with Sidewall Reflections." In *Coastal Engineering 1992*, 3468-81, 1993.

Naito, S. "Wave Generation and Absorption in Wave Basins: Theory and Application." *International Journal of Offshore and Polar Engineering* 16, no. 2 (2006/6/1/): 81-89.

Newman, JN. "Analysis of Wave Generators and Absorbers in Basins." *Applied Ocean Research* 32, no. 1 (Feb 2010): 71-82.

Newman, JN. "Channel Wall Effects in Radiation-Diffraction Analysis." Paper presented at the Proceedings of the 31st International Workshop on Water Waves and Floating Bodies. Available at: www. iwwwfb. org, 2016.

Newman, JN. "Wave Effects on Multiple Bodies." *Hydrodynamics in Ship and Ocean Engineering* 3 (2001): 3-26.

O'Dea, JF and JN Newman. "Numerical Studies of Directional Wavemaker Performance." Paper presented at the 28th American Towing Tank Conference, Ann Arbor, Michigan, 2007: 9-10.

Ottesen Hansen, NE. "Long Period Waves in Natural Wave Trains." *Progress Report No.46*, Institute of Hydrodynamics and Hydraulic Engineering, TU of Denmark (1978): 13-24.

Shen, J, and HD Qin. "Tank Green Function with Partial Reflections from Side Walls." *26th International Workshop on Water Waves and Floating Bodies* (2011): 177-180.

Stokes, GG. "On the Theory of Oscillatory Waves." *Trans Cambridge Philos Soc* 8 (1847): 441-73.

Svendsen, IA. "Physical Modelling of Water Waves." *Physical Modelling in Coastal Engineering.* AA Balkema, Rotterdam (1985): 13-48.

Tanizawa, K. "The State of the Art on Numerical Wave Tank." Paper presented at the Proc. 4th Osaka Colloquium on Seakeeping Performance of Ships, 2000: 95-114.

Tanizawa, K and M Minami. "Development of a 3d-NWT for Simulation of Running Ship Motions in Waves." *16th International Workshop on Water Waves and Floating Bodies*, 2001: 157-160.

Ursell, F, RG Dean, and YS Yu. "Forced Small-Amplitude Water Waves: A Comparison of Theory and Experiment." *Journal of Fluid Mechanics* 7, no. 01 (1960): 33-52.

Westhuis, J. *The Numerical Simulation of Nonlinear Waves in a Hydrodynamic Model Test Basin*. University of Twente, 2001.

Xia, J. "Some Insight into the Green Function of the Channel Problem." *17th International Workshop on Water Waves and Floating Bodies* (2002): 195-198.

Zhang, XT, BC Khoo and J Lou. "Wave Propagation in a Fully Nonlinear Numerical Wave Tank: A Desingularized Method." *Ocean Engineering* 33, no. 17-18 (Dec 2006): 2310-31.